# EFFECT OF ELECTRICAL STIMULATION ON BONE

# THE EFFECTS OF ELECTRICAL STIMULATION ON LOSS OF BONE MASS IN THE OVARIECTOMIZED RAT

By AKIV JHIRAD, B.ENG.

A Thesis Submitted to the School of Graduate Studies in Partial Fulfilment of the Requirements for the Degree Master of Applied Sciences

McMaster University MASTER OF APPLIED SCIENCE (2018) Hamilton, Ontario (Biomedical Engineering)

TITLE: The Effects of Electrical Stimulation on Loss of Bone Mass in the Ovariectomized Rat

AUTHOR: Akiv Jhirad, B.ENG. (McMaster University)

SUPERVISOR: Dr. Gregory Wohl

NUMBER OF PAGES: xviii, 141

# LAY ABSTRACT

In osteoporosis treatment, current interventions, including pharmaceutical treatments and exercise protocols, suffer from challenges of guaranteed efficacy for patients and poor patient compliance. Moreover, bone loss continues to be a complication factor for conditions such as spinal cord injury, prescribed bed-rest, and space flights. A low-cost treatment modality could improve patient compliance. Electrical stimulation has been shown to improve bone mass in animal models of disuse, but there have been no studies of the effects of electrical stimulation on bone in the context of bone loss under hormone deficiency such as in post-menopausal osteoporosis. To explore whether electrical stimulation could positively affect bone mass, we developed and tested a custom electrical stimulation device in the ovariectomized rat model of post-menopausal osteoporosis.

# ABSTRACT

In osteoporosis treatment, current interventions suffer from challenges of guaranteed efficacy for patients. Electrical stimulation has been shown to improve bone mass in animal models of disuse, but there have been no studies of the effects of electrical stimulation on bone loss in a hormone deficiency model. The purpose of this study was to explore the effects of electrical stimulation on bone mass in the ovariectomized (OVX) rat model.

We developed a custom electrical stimulation device capable of delivering a constant current, 15 Hz sinusoidal signal. We used 30 female Sprague Dawley rats (12-13 weeks old). Half were OVX, and half underwent sham OVX surgery (SHAM). These rats were divided into baseline, stimulation (stim), and no-stimulation (no-stim) groups. Stimulation groups received transdermal electrical stimulation to the right knee, while the left knee served as a non-stimulated contralateral control. The no-stimulation groups had electrodes placed on the right knee, but not connected. Rats underwent the procedure for one hour per day for six weeks. Rats were sacrificed ($CO_2$) after six weeks. Femurs and tibias were scanned by microCT. MicroCT data were analyzed for trabecular and cortical bone measures.

Femurs and tibias from OVX rats had significantly less trabecular bone than SHAM. In the distal femur of OVX-stim rats, bone volume fraction was significantly greater in the stimulated right than the non-stimulated contralateral

(left). There were no differences between stim and no-stim groups for tibial trabecular measures, or cortical bone measures in either the femur or the tibia.

This study presents novel findings that electrical stimulation can partially mitigate bone loss in the OVX rat femur, a model of human post-menopausal bone loss. Further work is needed to explore why there was a differential response of the tibial and femoral bone, and to better understand how bone cells respond to electrical stimulation.

# ACKNOWLEDGEMENTS

I would like to take this opportunity to express my sincere appreciation to those who supported me through the process of completing my degree. Thank you to Dr. Greg Wohl for allowing me to do this project and providing invaluable guidance towards achieving my goal. I would also like to thank Dr. DeBruin from contributing his expertise in electrical stimulation to this project. Finally, I would like to thank my parents for supporting me in this journey and being there when I needed them.

# TABLE OF CONTENTS

# LIST OF FIGURES

# LIST OF TABLES

# LIST OF ABBREVIATIONS & SYMBOLS

| | |
|---|---|
| ALP | Alkaline Phosphatase |
| BMD | Bone Mineral Density |
| BMP-2 | Bone Morphogenetic Protein 2 |
| BV | Bone Volume |
| BV/TV | Percent Bone Volume |
| CMD | Command Line |
| CMRR | Common Mode Rejection Ratio |
| DA | Degree of Anisotropy |
| EBGS | Electronic Bone Growth Stimulator |
| ECM | Extracellular Matrix |
| hMSC | Human Mesenchymal Stem Cells |
| HPF | High-pass Filter |
| IC | Integrated Circuit |
| IGF-1 | Insulin-like Growth Factor 1 |
| LPF | Low-pass Filter |
| MARC | McMaster Automotive Resource Centre |
| OVX | Ovariectomized |
| PEMF | Pulsed Electromagnetic Field |
| PTH | Parathyroid Hormone |
| PTM | Proximal Tibial Metaphysis |
| RMS | Root Mean Square |
| ROI | Region of Interest |
| SOP | Standard Operating Procedure |
| SPF | Special *Pasteurella*-free |
| Tb.N | Trabecular Number |

| | |
|---|---|
| Tb.Th | Trabecular Thickness |
| TV | Tissue Volume |
| VEGF | Vascular Endothelial Growth Factor |

# DECLARATION OF ACADEMIC ACHIEVEMENT

# CHAPTER 1: INTRODUCTION

The ability of animals to inherently generate electricity has been known since ancient times. In fact, ancient Romans used electric shocks produced by electric rays as therapeutic agents to treat illnesses (Parent 2004). The modern interest in biological electricity stems from the work of Giovanni Aldini, Luigi Galvani, and Allesandro Volta in the 1790's, with experiments dealing with frog leg twitching when exposed to various electricity-producing machines (Parent 2004). Building on this research, in 1952 Hodgkin et. al conducted experiments on the giant axon of a squid, depolarizing the axon membrane with a voltage clamp apparatus and assessing the influence of an external electric field on current flowing into the axon (Hodgkin et al. 1949). The group recorded a current flowing into the cell in the initial phase of the response, which was unexpected for the behaviour of pure charge under an applied electric field. Hodgkin et. al realized that the current was a result of ionic movement due to an energy gradient derived from cell metabolic activity, which was activated by the external electric field that induced change in membrane permeability (Piccolino 1997). These experiments led to the discovery of the movement of ions in the cell membrane, providing insight into the complex nature of the electric signalling mechanism in cells.

Since then, many researchers have focused on the electrical activation of the neuromuscular system, namely, applying electrical signals to nerves to elicit muscle contraction. We now know that nerves can be activated via polarized electrodes that

create a localized electric field which depolarizes the cell membranes of neurons. If the collective depolarization reaches a certain threshold, an action potential will propagate in both directions from the site of stimulation due to an influx of Na+ ions from the extracellular space into the intracellular space (Peckham & Knutson 2005). Additionally, the excitation of nerves and muscle fibers have different polarization thresholds (Mortimer 2011), allowing the selective activation of tissues in the body.

The phenomena of electricity in the body has also been applied to bone, and it is believed to be an important factor in the bone remodelling process. Bone is thought to be an inherently piezoelectric material, where mechanical stresses induce an electric polarization through the bone. The application of electricity to bone was initiated by Fukada et. al in 1957, who were the first to demonstrate the piezoelectric effect in dry bone (Fukada & Yasuda 1957). Their experiments also showed that the effects were not of biological origin, and they hypothesized that the effects were instead due to the crystalline micelle of collagen molecules along with the symmetry of collagen fibres in bone tissue. Additionally, they discovered that the relationship between the mechanical strain on bone and electrical polarization induced within bone was linear, and that there was also a linear relationship between the mechanical strain produced by subjecting bone to an electric field.

Mcelhaney et. al went further on and empirically determined the charge distribution on a dried human femur due to load, known as stress-generated potentials, and showed that when a section of bone is uniformly stressed areas of

positive and negative charge are produced on the bone surface (Mcelhaney 1967). Stress-generated potentials arising from longitudinal stresses on feline fibulae have been explored by Basset et. al (Bassett & Becker 1962), who found that the electrode positioned on the convex side of the bone undergoing flexion (while the fibulae bows under the stress) became negative with respect to the other electrode. The amplitude of the potentials on each electrode was influenced by the magnitude and rate of deformation, and the polarity was determined by the direction of bending. This is significant because research conducted on misaligned fractures in children showed that new bone is deposited on the concave side of deformity, while old bone is removed from the convex side, allowing the misalignment to straighten with time (Bassett & Becker 1962). The positively charged concave side of bone induces chemotaxis in osteoblasts and attracts the cells here, since they, like most cells, have a negative membrane potential (Isaacson & Bloebaum 2010). Thus, it has been said that this chemotaxis enables new bone to be deposited on the concave side of deformity, thereby allowing alignment of misaligned fractures.

The discoveries of piezoelectricity and stress-generated potentials paved the way for research in the effects of electrical signals in bone, since they have been shown to always be present when bone undergoes stresses. Therefore, researchers have postulated that an external electrical signal may be able to serve as an analog for these charge-based bone cell stimuli, which can be delivered using electrical stimulation. Research has been performed using electrical stimulation on fracture healing and animal models of bone loss, but there have been no studies of the effects

of capacitive coupling on a hormone-deficient animal model of post-menopausal osteoporosis. Such a modality could have positive implications for the treatment of osteoporosis.

# CHAPTER 2: OBJECTIVES & HYPOTHESES

The main objective of this research was to examine the effects of electrical stimulation on bone loss using low frequency, constant current, capacitive coupling stimulation. Specifically, this research looked at the capability of electrical stimulation to mitigate bone loss in the OVX rat, a hormone-deficient animal model of human post-menopausal osteoporosis. To achieve the stimulation, a custom electrical stimulation circuit was developed and tested on OVX rats. Following experimentation, micro CT analysis and fluorescence microscopy were used to determine characteristics of the tibia. Finally, the stimulated group was compared to the non-stimulated controls. The OVX rat has been shown to closely mimic the bone loss experienced by postmenopausal humans, so the overall motivation behind this study was to determine whether low frequency, constant current, capacitive coupling stimulation could retard or reverse the bone loss that occurs due to osteoporosis.

## 2.1 OBJECTIVES

1. To develop a circuit that can deliver a 15 Hz, sinusoidal, 250 $\mu$A constant current signal for the electrical stimulation;

2. To develop a novel Standard Operating Procedure (SOP) with a custom anesthetic device to enable experimentation on multiple rats at once; and
3. To evaluate the effectiveness of the electrical stimulation treatment using experimental methods;

## 2.2 HYPOTHESES

Electrical stimulation will mitigate bone loss in the leg of the ovariectomized rat.

# CHAPTER 3: BACKGROUND

Due to the potential of electrical signals in influencing bone cell behaviour, electrical stimulation in-vivo became a popular research endeavour for applications in bone repair (Nabil et al. 2014; Kane 1987; Saltzman et al. 2004; Otter et al. 1998; Fredericks 1999; Inoue et al. 2002; Brighton, Hozack, et al. 1985; Hassler et al. 1976). Similar research was performed to assess the effects of electrical stimulation for preventing bone loss (Lirani-Galvão et al. 2006; Sert et al. 2002; Eser et al. 2003; Eyres et al. 1996; Chang & Chang 2003; Brighton, Katz, et al. 1985; Mcleod & Rubin 1992; Rubin et al. 1989). To try and understand the underlying mechanisms of how electrical stimulation affects bone, many in-vitro studies have been performed, with a focus on the expression of biomolecules that play a role in bone growth and healing cascades (Stein & Lian 1993; Griffin et al. 2013; Hartig et al. 2000; Stromal et al. 2009; Hwang et al. 2012; Bodamyali et al. 1998).

The three types of electrical stimulation techniques used are: direct current stimulation, capacitive coupling stimulation, and inductive coupling stimulation. Direct current stimulation involves the surgical implantation of metal electrodes the area of bone requiring repair and consists of two or more electrodes supplying a constant current to the tissue. Capacitive coupling stimulation involves placing two electrodes or pair of parallel plate capacitors on the surface of the skin surrounding the site of the bone area of interest, while ensuring the site is within the induced electric field. This stimulation technique generally employs the use of an alternating current electric field, which is supplied by circuitry generating a signal of certain frequency and waveform. Inductive coupling stimulation involves the placement of a metal coil over the bone region of interest. When current passes through the coil, a magnetic field proportional to the current is generated, which in turn causes an electric field to form within the tissue. Since the magnitude of the electric field is dependent on that of the magnetic field, a time-varying electric field can be induced along the fracture site by varying the amplitude of the current flowing through the metal coil (Kuzyk & Schemitsch 2009). This time-dependent electric field is known as a Pulsed Electromagnetic Field (PEMF).

## 3.1 ELECTRICAL STIMULATION IN VITRO

In vitro studies of electrical stimulation have provided insights into the biochemical effects of electrical stimulation in bone, utilizing direct current, capacitive coupling, and PEMF stimulation methods. These studies provide an avenue in determining the various growth factors, hormones, and biomolecules that

are affected by the stimulus, and allow inference of the possible effects of electrical stimulation in vivo.

### 3.1.1 Gene Expression

The administration of electrical stimulation in osteoblast-like cells has resulted in upregulation in the genes of proteins that have positive effects in bone. An increased expression of genes that produce proteins responsible for bone mineralization such as collagen I, bone sialoprotein, osteonectin, osteopontin, and osteocalcin (Stein & Lian 1993) has been observed using both direct current (Griffin et al. 2013) and capacitive coupling (Hartig et al. 2000) stimulation. Additionally, osteonectin has a more specific role in inducing cellular adhesion and growth (Lane & Sage 1994), and bone sialoprotein and collagen I contribute to the formation of the extracellular matrix (ECM) (Owen et al. 1990). Overall, since the expression of these mineralization-related genes reflects the maturation of osteoblasts in vivo (Owen et al. 1990), the significant increase in expression implies that electrical stimulation can play a role in accelerating both the maturation and biomineralization of osteoblasts.

### 3.1.2 Alkaline Phosphatase

Another finding common to in-vitro electrical stimulation research on osteoblasts is the upregulation of the enzyme alkaline phosphatase (ALP). A significant increase in ALP gene activity has been found using direct current electrical stimulation (Griffin et al. 2013), and capacitive coupling electrical

stimulation (Hartig et al. 2000). Additionally, an increase in the relative gene expression of ALP has been found using direct current electrical stimulation (Griffin et al. 2013). ALP is a thoroughly-studied enzyme that is known to induce calcification in bone cells, thereby initiating the bone mineralization process (Golub & Boesze-Battaglia 2007). Thus, the increase in ALP gene expression and activity by electrical stimulation could be another pathway by which the biomineralization of osteoblasts could be enhanced.

### 3.1.3 Growth Factors

The effects of electrical stimulation on upregulation of growth factors in cells has also been explored in-vitro. Specifically, direct current electrical stimulation in human mesenchymal stem cells (hMSCs) has been shown to enhance the gene expression of insulin-like growth factor 1 (IGF-1), bone morphogenetic protein 2 (BMP-2), and vascular endothelial growth factor (VEGF) (Hwang et al. 2012; Kim et al. 2006). Similar effects on BMP-2 and BMP-4 have also been found using PEMF in osteoblasts, with gene expression levels being shown to correlate positively with exposure time of the electrical stimulation (Bodamyali et al. 1998). BMP-2 and BMP-4 have been shown to be crucial factors in skeletal repair and regeneration (Bragdon et al. 2011), and their roles are complemented by VEGF without which there would be impaired trabecular bone formation, and suppressed blood vessel development in bone (Gerber et al. 1999). Additionally, IGF-1 is an important signalling molecule in cells of osteoblast lineage, and has been shown to influence bone formation rate, mineral apposition rate, osteoblast cell population,

and osteoclast cell population (Zhang et al. 2002). Collectively, the increased expression of these biomolecules through the administration of electrical stimulation could lead to an enhancement of bone formation and healing (Peng et al. 2002), along with reduced bone mineral density (BMD) loss (Yakar et al. 2002) in vivo.

## 3.2 ELECTRICAL STIMULATION FOR BONE HEALING

Since the discoveries of the piezoelectric effect and stress-generated potentials in bone by Fukada et. al (Fukada & Yasuda 1957) and Mcelhaney et. al (Mcelhaney 1967), research in electrical stimulation emerged as a method of increasing the rate of bone growth in individuals, as those who experienced delayed healing or non-union after injury had minimal therapeutic alternatives, the only one available being surgical intervention (Isaacson & Bloebaum 2010). In contrast to applications of electrical stimulation for preventing bone loss, electrical stimulation for bone healing has been found to be beneficial using all three of the methods stated above.

### 3.2.1 Direct Current

Hassler et. al (Hassler et al. 1976) studied the effects of direct current electrical stimulation in the osteotomized calvarium of adult, male, New Zealand white rabbits, with the goal of examining the percent bone growth at the cathodic electrode. The group developed a 5-bristle platinum anode and cathode device using brush electrodes, and applied waveforms varying in shape, current, frequency, and

repetition rate directly at the osteotomy sites. Their experiments showed that with a certain range of electrical stimulation power, shown in Figure 1, there was significant bone growth and healing at the osteotomy site where the cathode was situated. On the contrary, the anode always showed a lack of healing compared to control Figure 2, with bone corrosion occurring at currents of 1000 $\mu$A due to a higher current density being applied by the electrodes (Hassler et al. 1976).

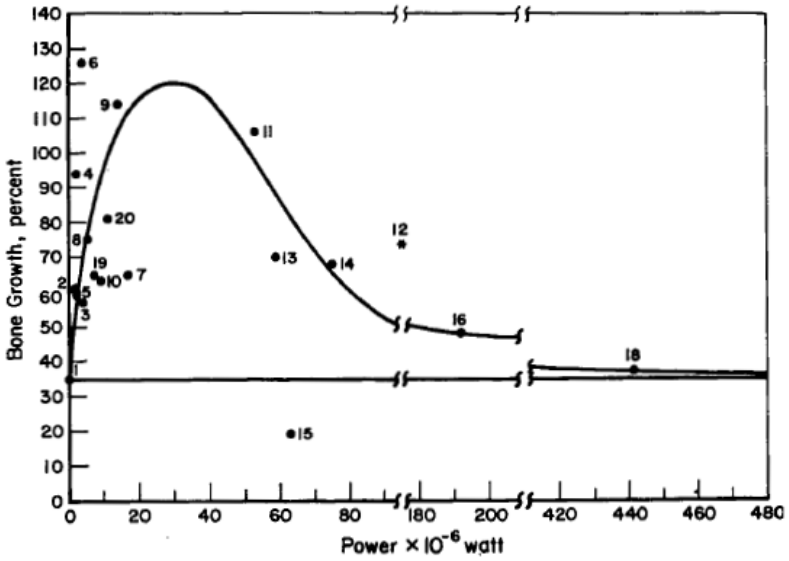


Figure 1: Percent Bone growth at the cathode as determined by radiographic densitometry vs. power dissipation (Hassler et al. 1976)

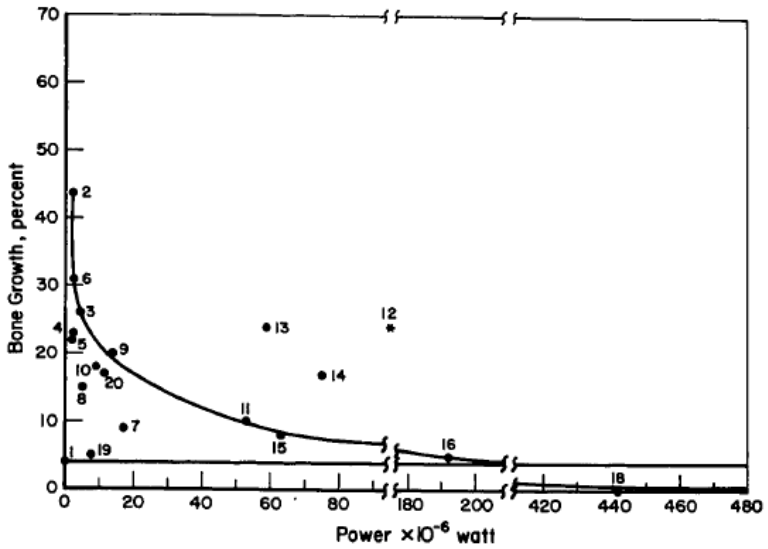


Figure 2: Percent Bone growth at the anode as determined by radiographic densitometry vs. power dissipation (Hassler et al. 1976)

DC stimulation has also been used to try and accelerate the rate of spinal fusion (Kane 1987) using a commercial electronic bone growth stimulator (EBGS). The group performed a large randomized prospective controlled trial to assess whether radiographically successful spinal fusion occurred at a higher rate when the EBGS was used to supplement the conventional spinal fusion procedure, with a comparison to the procedure alone. The results of the trial showed an 81% success rate of spinal fusion using the EBGS, compared to only 54% of the non-stimulated control group, this difference being statistically significant. Additionally, the group performed statistical analysis on different characteristics of the patients such as: number of spinal levels requiring fusion, and previous failed spinal fusion attempts (failed fusion, spondylolisthesis, grafting, and other high-risk factors). This analysis

also showed a higher number of successful spinal fusion cases using the EBGS compared to the control group, in all the stated characteristics (Kane 1987).

### 3.2.2 Pulsed Electromagnetic Fields

Electrical stimulation using PEMF has been the primary method for bone healing more recently due to its non-invasive and non-contact nature. Fredericks et. al (Fredericks 1999) utilized low-frequency PEMF and examined whether 60 minutes or less daily PEMF exposure would be able to accelerate bone repair in healing tibial osteotomies induced in special *Pasteurella*-free (SPF) New Zealand White Rabbits. The rabbits were randomly assigned into groups that underwent the PEMF treatment for different time periods per day (0 hours, 0.5 hours, 1 hour), and that underwent treatment for various number of days (14 days, 21 days, 28 days) before sacrificing. The PEMF stimulation itself consisted of pulse bursts of 30 ms with a repetition rate of 1.5 Hz, and a magnetic strength of 0 to 1 Gauss in 230 $\mu$s (Figure 3). The group chose the healing outcome to be the point at which the osteotomized tibiae had acquired biomechanical properties not significantly different from the intact tibiae, using tests for torsional strength and stiffness. Their results showed that PEMF treatment for 1 hour per day was the most effective and was able to reduce healing time by 2 weeks relative to the control (0 hours per day). Additionally, the most efficient stimulation of bone formation was seen in the 1 hour per day treatment in the form of tibial calluses (Figure 4).

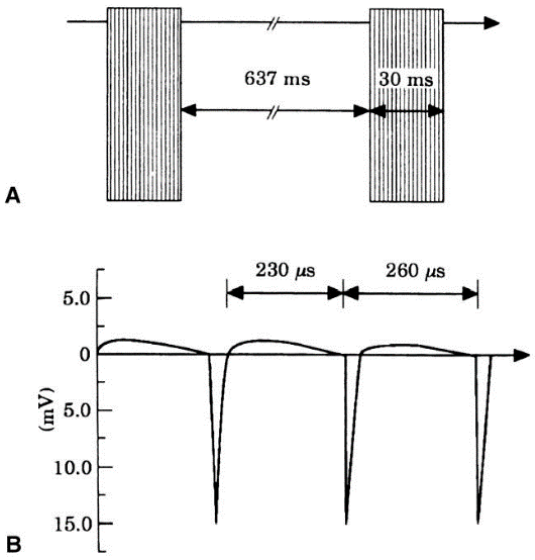


Figure 3: Schematic representation of the PEMF. **A**: The PEMF signal of 30 ms pulses at 1.5 Hz. **B**: The voltage change as the magnetic field rose from 0 to 1 Gauss in 230 $\mu$s. (Fredericks 1999)

| | Sham | | Group I | | Group II | |
|---|---|---|---|---|---|---|
| Days | Bone (%) | Cartilage (%) | Bone (%) | Cartilage (%) | Bone (%) | Cartilage (%) |
| 14 | 20 | 80 | 35 | 65 | 68 | 32 |
| 21 | 55 | 45 | 80 | 20 | 81 | 19 |
| 28 | 62 | 38 | 85 | 15 | 86 | 14 |

Group I was exposed to a low-frequency, low-amplitude pulsed electromagnetic field (PEMF) for 0.5 hour per day; Group II was exposed for 1.0 hour per day; the sham control group received no exposure.

Figure 4: Bone and Cartilage composition of callus developed during healing (Fredericks 1999)

Inoue et. al (Inoue et al. 2002) developed a standardized delayed union model that induces a reduction in bone strength and limb load-bearing function compared to the osteotomized bone model used by electrical stimulation applications traditionally. Using this model, the group studied the effects of the same PEMF stimulation utilized by Fredericks et. al (Fredericks 1999) (described

above) on bone osteotomy in the canine mid-tibia. The statistical analysis performed was using comparisons between stimulated and non-stimulated group, as well as using within-specimen comparisons between the osteotomized tibia with the intact, contralateral tibia. The results showed that the PEMF treatment was able to accelerate healing in the canine tibia by achieving faster rate of increase in load-bearing over time by the osteotomized tibia and inducing a greater periosteal callus area around the osteotomy site. Additionally, the group found a statistically significant increase in the mean ratio of maximum torque and torsional stiffness withstood by the left and right tibia of each specimen in the PEMF group ($74.7 \pm 10.7$ % and $86.1 \pm 10.6$ % respectively) compared to the control group ($56.0 \pm 16.1$ % and $63.2 \pm 12.6$ respectively), indicating that the PEMF treatment led to much better healing than the control as the performance of the osteotomized bone more comparable to the intact tibia.

Although PEMF has shown success is animal models, Saltzmann et. al (Saltzman et al. 2004) found a low success rate in its abilities in treatment of delayed healing in foot and ankle arthrodesis, an important procedure for arthritis patients in which a joint is surgically immobilized by fusion of adjacent bones. An important note is that the patients that underwent the PEMF treatment showed failure to heal at 4 months or longer post-operatively. In the 19 patients that underwent a protocol of PEMF, restricted weight-bearing, and immobilization in a short-leg cast, 5 (26%) showed successful fusion sites in the ankle joint. The researchers noted that they were unable to obtain a control group for the PEMF

treatment and surgical intervention alone and were unable to make definitive conclusions on patient-related factors such as age or tobacco use due to the limited sample size.

### 3.2.3 Capacitive Coupling

To try and pinpoint the ideal electrical stimulation characteristics for bone healing, Brighton et. al (Brighton, Hozack, et al. 1985) performed experiments with various electrical parameters such as peak-to-peak voltage, root mean square (RMS) of the applied current, and signal frequency. The group performed midshaft transverse osteotomies on the right fibulae of New Zealand white rabbits and developed a custom capacitive coupling stimulation device using 2 flexible stainless-steel circular plates, applied directly to the skin with the fracture site being in between. Since high frequency signals have been known to penetrate skin more effectively than low frequency, a focus was on using higher frequency signals so that lower applied voltages can be utilized (Brighton, Hozack, et al. 1985). To assess the effectiveness of the electrical stimulation, roentgenograms of the fibulae were taken, with scores being determined through visual inspection of the degree of fracture healing present. Additionally, mechanical tests were conducted using 3-point bending (Figure 5) to determine the difference in stiffness between the stimulated (right) fibulae compared to the non-stimulated. Brighton et. al found that capacitively coupled electrical stimulation can stimulate fracture healing, with dose-response characteristics and optimal healing occurring using a signal with a 60 kHz frequency (Figure 6).

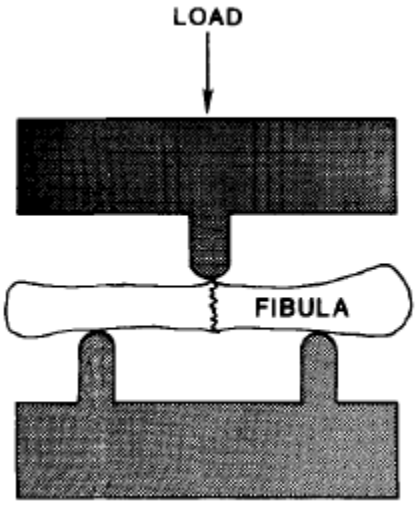


Figure 5: 3-Point bending jig used by Brighton et. al to mechanically test the healing fracture fibulae (Brighton, Hozack, et al. 1985)

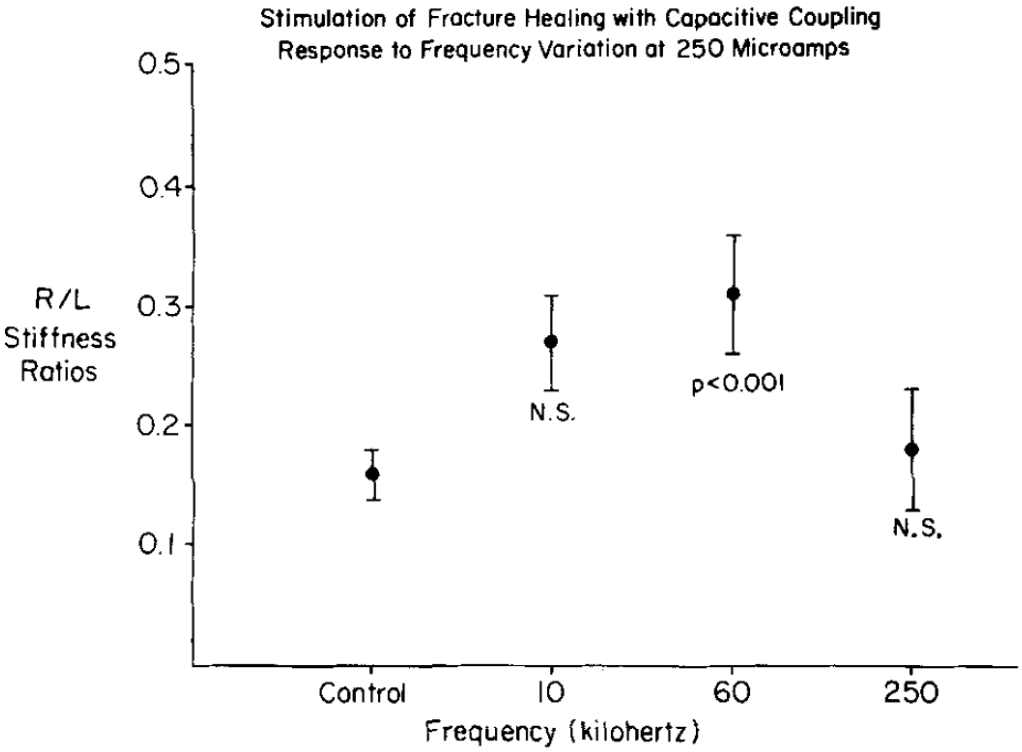


Figure 6: Right/left stiffness ratios where the current was held constant at 250 μA and the frequency was varied (Brighton, Hozack, et al. 1985)

Although most bone healing applications of electrical stimulation have been for fractures in long bones and spinal fusion, Nabil et. al (Nabil et al. 2014) studied the effects of capacitive coupling stimulation on segment transfer distraction osteogenesis for the purposes of mandibular reconstruction. Distraction osteogenesis involves gradually pulling apart bone surfaces and allowing new bone to form in between, eliminating the need for bone grafting. The goal of this research was to examine whether the use of electrical stimulation during the distracting process would result in distracted bone with greater bone density. The group developed a custom electrical stimulation device (Figure 7) that delivered a current of 10 $\mu$A to the distracted zone. With a distraction target of 2 mm/day, they reported that the electrical stimulation group was able to achieve this rate, while the control group encountered many complications, preventing the maintenance of a 2 mm/day rate. At the end of the experimental period, the electrical stimulation group achieved a bone density of $779 \pm 201$ at the distraction process, while the control group achieve a bone density of $720 \pm 150$, the results being statistically significant.

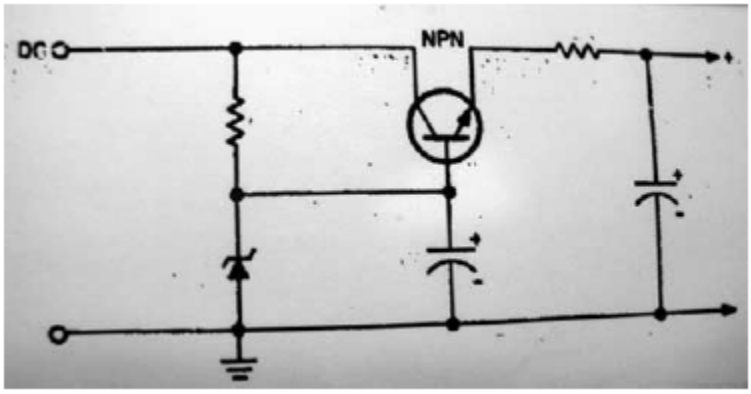


Figure 7: Diagram of the electric current circuit of the electrical stimulator developed by Nabil et. al (2014)

## 3.3 ELECTRICAL STIMULATION FOR BONE LOSS

The success of electrical stimulation in in-vivo bone healing and in-vitro cell stimulation has also led researchers to examine whether or not it may have effects in reducing bone loss in vivo. As mentioned earlier, compressive stresses on bone result in electronegative potentials being generated, while electropositive potentials are generated with tensile stresses (Kuzyk & Schemitsch 2009). These changes in potentials experienced by bone result in the movement of charge-carrying particles, which can be mimicked using electrical stimulation. There have been a wide variety of stimulation parameters used with PEMF and capacitive coupling electrical stimulation, with different techniques leading to different effects on cortical bone area, BMD and bone formation rate.

### 3.3.1 Pulsed Electromagnetic Fields

The most common method of studying the effects of electrical stimulation on bone loss has been through the use of PEMF. PEMF employs the usage of two coils in a Helmholtz configuration, which induces an electromagnetic field in between them when an electric current is applied. The effects of using simple sinusoidal versus complex PEMF waveforms have been examined in the isolated turkey ulnae model, making comparisons to an electrical stimulation control group as well as a within-subject comparison of the isolated and intact ulnae. The results (Figure 8) showed that the simplest, lowest frequency sinusoidal waveform (15 Hz frequency, 0.08 mV amplitude) resulted in the greatest increase in cortical area relative to both the electrical stimulation control group and the contralateral ulnae within-group (Mcleod & Rubin 1992). A similar study was conducted to examine the effect of pulse power on cortical bone area, and found that there was a maximum osteogenic effect between 0.01 and 0.04 $T^2/s$ (Rubin et al. 1989). Additionally, the within-group comparison of the contralateral ulnae of the study showed a -13% difference in cortical area in the control group, and a 12.3% difference in the group that underwent the 0.01 $T^2/s$ stimulation protocol.

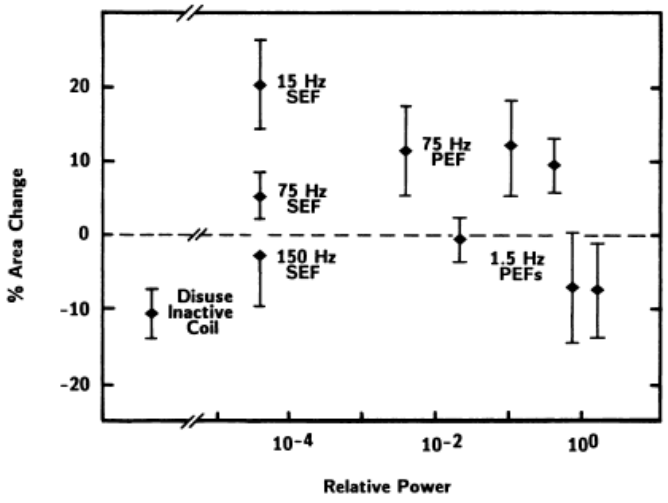


Figure 8: Summary of the changes in cross-sectional area (mean and standard error of the mean) of the functionally isolated ulnae after exposure to various electric-field signals (Mcleod & Rubin 1992)

Another popular animal model for PEMF experiments has been the female ovariectomized (OVX) rat model, due to an induced osteoporosis effect that is remarkably similar to that experienced by humans (Jee & Yao 2001). Using a 50 Hz frequency, 1 mT magnetic field strength PEMF signal resulted in a significant increase in the cortical thickness of the tibial bone in OVX rats (Sert et al. 2002). Additionally, the effects of a 7.5 Hz frequency, 1~2 mV/cm electrical field was examined in the trabecular bone of the proximal tibial metaphysis of OVX rats (Chang & Chang 2003). This treatment resulted in a significant increase in trabecular bone volume percentage, trabecular thickness, and trabecular bone formation rate.

### 3.3.3 Capacitive Coupling

Capacitive coupling involves the usage of conducting electrodes on the surface of the skin on opposite sides around the bone area of interest. An electrical signal applied to the electrodes creates an electric field that induces the movement of charge within the tissue. The effects of a 60 kHz sinusoid at varying amplitudes were examined in the sciatic denervation disuse bone loss rat model, to see if electrical stimulation was able to both prevent and treat induced disuse-induced bone loss (Brighton, Katz, et al. 1985). The sciatic denervation was administered in the right leg, while the left leg was intact and used as an internal control, with varying amplitudes of electrical stimulation being applied to the right leg in different groups. For prevention of bone loss, electrical stimulation was able to maintain the percent porosity, cortical thickness, and cortical area of the denervated bone to a level that was not statistically different from the internal control. Similarly, for treatment of osteoporosis electrical stimulation was able to greatly reduce the percent porosity when performing an internal paired control with the contralateral tibia (Figure 9), increase cortical area, and increase cortical thickness of the denervated bone when compared to the non-stimulated, denervated control (Brighton, Katz, et al. 1985).

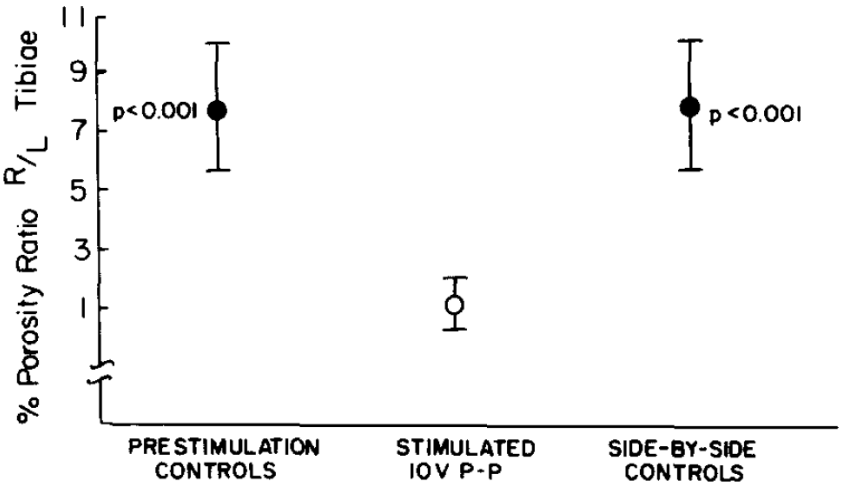


Figure 9: Graph showing the percent porosity of sciatic-denervated tibiae treated with 10 V peak-to-peak, 60 kHz electrical stimulation (Brighton, Katz, et al. 1985)

Capacitive coupling electrical stimulation has also been used to examine global effects in OVX rats that have had their whole body within a 1.5 MHz, 30 mW/cm2 electric field (Lirani-Galvão et al. 2006). These experiments found an increase in the global BMD (Figure 10), spinal BMD, and lower limb BMD in the treatment group (OVX with electrical stimulation) compared to the diseased (OVX with no electrical stimulation) group.

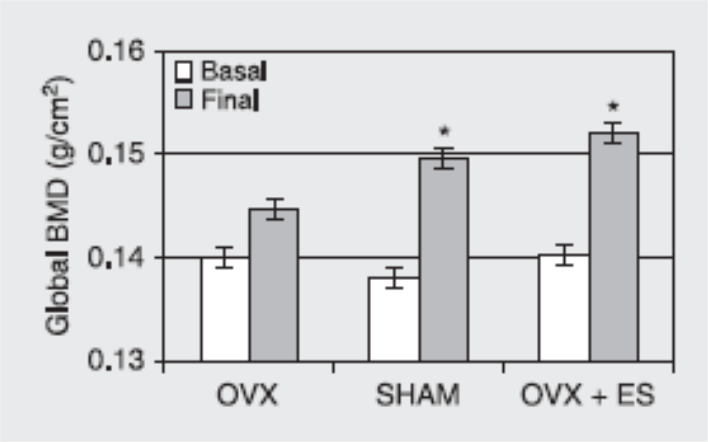


Figure 10: Global BMD 7 days after surgery (Basal), and at the end of the 84-day protocol (Final). The OVX and SHAM groups received no electrical stimulation (ES) (Lirani-Galvão et al. 2006)

# CHAPTER 4: THEORY

## 4.1 ELECTRICAL STIMULATION CIRCUIT

### 4.1.1 Constant Current Circuit

For the applications of this experiment, a constant current electrical stimulation protocol was selected. Traditionally, constant current stimulation has been preferred over alternatives such as constant voltage because electrical current is the factor that stimulates tissue. Additionally, tissue and electrode resistance can alter as stimulation proceeds, so a constant current circuit can adapt to this change in resistance and alter the voltage to ensure the same stimulation is being delivered (WPI 2013). For our specific application a constant current stimulation protocol is advantageous because each OVX rat had different resistance in the leg (due to variability in skin thickness, muscle mass, and subcutaneous fat), so the constant

current helped to reduce variability in the magnitude of stimulation delivered to each rat.

The constant current circuit (Figure 11) consisted of a difference amplifier (outlined in red) and a comparator circuit (outlined in green). The comparator adjusted its output voltage until it reached its stability criterion, i.e. when both input voltages were the same, corresponding to $V_{source}$. This in turn forced the output of the difference amplifier op-amp to be equal to $V_{source}$. The difference amplifier multiplied the difference between the voltages at its inputs by a gain factor set by the ratio of a pair of resistors ($R_3$ and $R_4$ or $R_1$ and $R_2$). Since the output of the difference amplifier was fixed, the difference between its inputs was fixed as well. Hence, the voltage-drop across $R_{sense}$ was also fixed as it was the input voltage multiplied by the factor chosen through the ratio of pair resistors in the circuit. Finally, since the voltage across $R_{sense}$ was fixed, the current through it was fixed as well. Since $R_1$ and $R_2$ were chosen to be much larger than $R_{load}$, the majority of this fixed current flowed through $R_{load}$. Hence, the current through $R_{load}$ was dependent only on $V_{source}$, the gain factor and $R_{sense}$, and followed the equation shown in Equation 1.

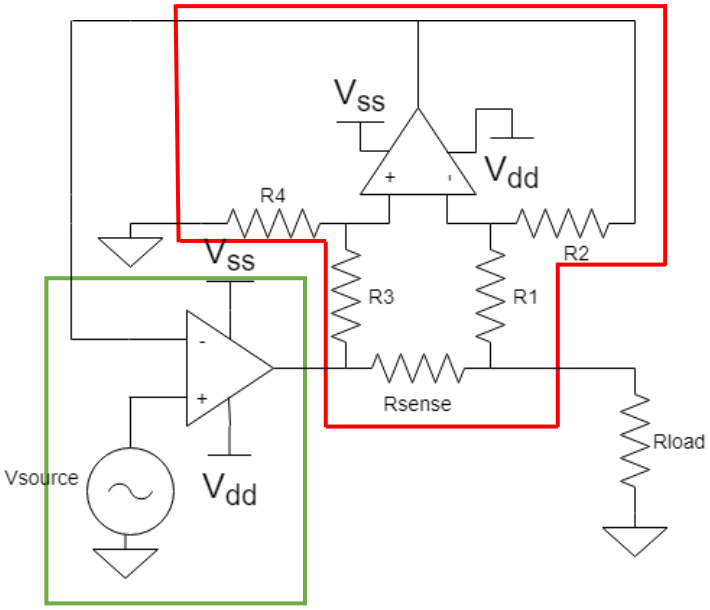


Figure 11: Constant current circuit schematic

$$I_{load} = \frac{V_{source}}{gain * R_{sense}}$$

Equation 1: Output current of the constant current circuit

An important aspect of the difference amplifier was its ability to reject signals that are common to both inputs, thereby reliably amplifying only the difference between the inputs. The extent to which the common signals are rejected depended on the gain of the op-amp, and the tolerance of the resistors selected, since a lower tolerance resulted in better matching between resistors (i.e. the goal is to match $R_1$ to $R_3$ and $R_2$ to $R_4$). Since high frequency noise can be picked up by circuit components, the main function of this rejection was to ensure the noise is not amplified and present in the output current. The ability of the circuit in rejecting this common signal was expressed as a ratio known as the Common Mode

Rejection Ratio (CMRR), and followed Equation 2, where $A_d$ is the gain of the difference amplifier and $t$ is tolerance of the resistors (Holt 2014).

$$CMRR \cong \frac{A_d + 1}{4t}$$

Equation 2: CMRR calculation for a difference amplifier

### 4.1.2 Microcontroller-Based Signal Generator

The first circuit developed for generating the input signal to the constant current circuit was utilizing the output of a small microcontroller to generate the electrical signal. Since a microcontroller can generally output only digital signals (i.e. Square pulses), filtering techniques were employed to achieve a signal that was sinusoidal in nature.

The microcontroller of choice was a Teensy-LC (Figure 12) due to its low cost, low power consumption, ease of programming, and battery operable capabilities. The microcontroller was programmed to output a digital signal of 1 for 1/30 seconds using the *digitalwrite()* function, and then output a 0 for 1/30 seconds using the *delay()* function, thus output a 15 Hz square wave signal. Appendix A shows the code use to program the microcontroller.


Figure 12: Teensy LC Microcontroller

Since the Teensy LC was only able to output digital (square) pulses, and a sine wave was the signal of choice for this research, analog filtering was implemented. A 50% duty-cycle (such as what was implemented using the code in Appendix A ) square wave consists of odd order harmonic sine waves with the same fundamental frequency as the square wave. Therefore, a sine wave with the same frequency as the square wave can be generated by filtering out the harmonics above this fundamental frequency (Stitt 1993). The square wave output by the microcontroller was sent to a 3-stage passive low-pass filter (LPF) circuit to convert the square wave into a triangular wave, followed by a sinusoidal wave with some sharp edges, and then finally a close-to-pure sinusoidal wave. Each stage of the 3-stage passive LPF had a cut-off frequency equal to the fundamental frequency of the square wave produced (15 Hz), and followed the equation shown in Equation 3 which is based on the time constant determined by the resistor and capacitor of choice. For this particular circuit, the capacitor value was chosen to be 100 nF, with the resistance required calculated to be 106,490 Ω using Equation 3.

$$f_c = \frac{1}{2 * \pi * R * C}$$

Equation 3: Cut-off frequency of a passive low-pass filter

Following the 3-stage LPF, the signal was sent through a high-pass filter (HPF) to remove DC offset. This DC offset is present because the Teensy LC is not able to output signals with negative voltages so the square wave produced has a minimum voltage of 0 V and a maximum voltage of 3.3 V, resulting in a DC offset of 1.65 V. The DC offset needed to be removed so the signal required for experimentation consisted of negative voltages, since both positive and negative charge potentials are present during normal biological function of bone (Isaacson & Bloebaum 2010). The HPF was designed in a similar manner to the LPF for a cut-off frequency of 0.9 Hz. Since the frequency of DC offset is 0 Hz, this HPF removed all signal components below the frequency of 0.9 Hz, thereby removing the offset as shown in Figure 13 (Greenfield 2015).

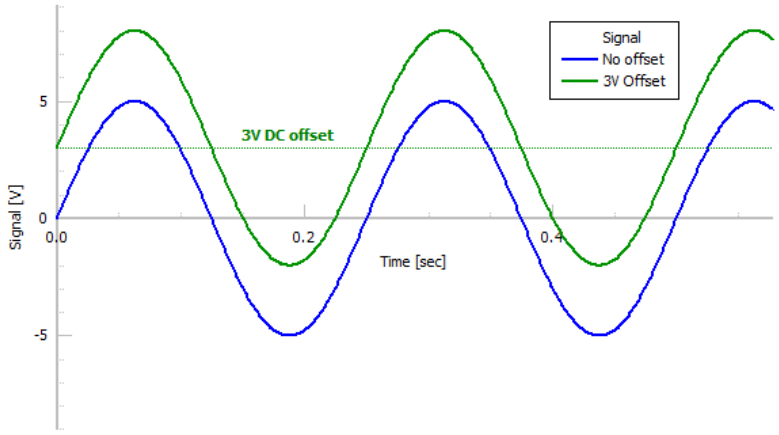


Figure 13: Effects of removing the DC offset of a signal (Greenfield 2015)

Finally, the signal was sent through a voltage divider to reduce the amplitude down to the level required to achieve our selected output current determined by Equation 1. A schematic of the full signal generator circuit is shown in Figure 14.

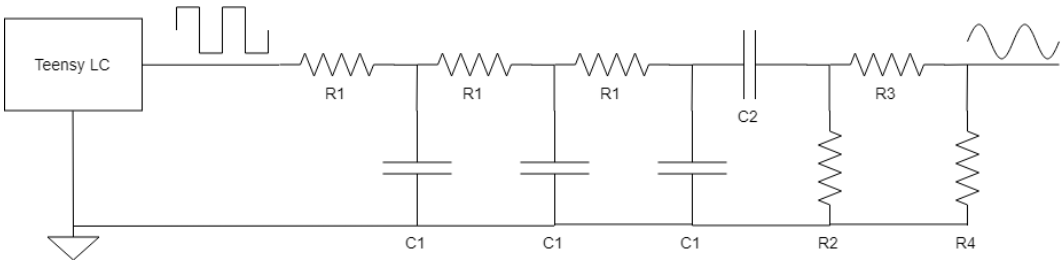


Figure 14: Signal generator circuit

## 4.2 ANIMAL MODEL FOR BONE LOSS

All tests performed on animals were approved by the Animal Research Ethics Board at McMaster University. The animal model chosen for these experiments was the OVX rat model. The OVX rat is currently the gold standard for studying treatments that act on osteoporosis-induced bone loss, and have been validated for this in multiple publications (Jee & Yao 2001). After the OVX procedure is performed, there is a fast decrease in cancellous bone mass and strength, which continues less quickly at certain sites until reaching an equilibrium of bone mass. This change in bone mass mimics that experienced by humans following menopause. The region of interest to observe changes in bone mass selected for these experiments is the Proximal Tibial Metaphysis (PTM), which has been shown to undergo statistically significant bone loss as early as 14 days post-OVX (Jee & Yao 2001). The PTM has also been shown to undergo 50% bone loss

between 30 and 60 days and has been shown to achieve steady state as early as 90 days. Hence, experimentation was ensured to start less than 14 days post-OVX to try and mitigate the amount of bone loss experienced before treatment. Additionally, the experimentation period was selected to ensure the bone loss in the PTM had not reached steady state by the end of the period.

## 4.3 ANIMAL LEG IMPEDANCE MODEL

### 4.3.1 Simple Impedance Calculation

To ensure the circuit would be functional at the impedance required at the output, an impedance model of the rat leg was developed using thickness and conductivity values found in literature (Belill et al. 2014; Bronaugh et al. 1983; Takeuchi et al. 2012; Andreuccetti et al. 1997). The model was developed under the assumption that the electric current would follow a path in the following order: skin, muscle, bone, muscle, skin. A consistent value for the thickness of muscle was not found in literature, so an inference of the thickness of the muscle was determined through measurement a rat cadaver and subtracting this total value from values for skin and bone thicknesses found in literature. The chosen tissue area was 1 cm x 1 cm, as this was the chosen electrode size to achieve the required current density for stimulation. Each tissue was modeled in 3 dimensions by using this 1 $cm^2$ area and multiplying it by the thicknesses found in literature. Finally, this value was use in conjunction with the tissue conductivity at 15 Hz found in literature to determine the tissue impedance at 15 Hz. The impedance was determined using the

formula shown in Equation 4, where $\rho$ is the resistivity (inverse of the conductivity), $L$ is the thickness of the tissue, and $A$ is the area determined by the size of the electrode. Table 1 shows a summary of the literature values and resultant tissue impedance.

$$R = \frac{\rho L}{A}$$

Equation 4: Calculation for tissue impedance at 15 Hz

| **Tissue** | **Conductance (S/m)** (Andreuccetti et al. 1997) | **Resistivity (Ω ∗m)** | **Thickness (mm)** | **Impedance (Ω)** |
|---|---|---|---|---|
| Bone | 0.0777 | 12.87 | 4 (Belill et al. 2014) | 635.5 |
| Skin | 0.0002 | 5000 | 0.033 (Bronaugh et al. 1983) | 1650 |
| Muscle | 0.2043 | 4.89 | 8 | 466 |

Table 1: Tissue impedance values of the rat leg

In addition to the impedance of various tissue, the impedance of the electrodes had to be considered. This information was obtained through email from speaking with a representative from Covidien (Dublin, Ireland). The impedance of a single electrode was taken to be 2724 Ω for a 1 $cm^2$ electrode. Hence, the total impedance of the load that the circuit would be required to deliver a constant current to is 10315.5 Ω.

The theoretical "constant current" capability of the circuit was found to not be exactly constant (CHAPTER 5: CIRCUIT DESIGN & PERFORMANCE). To

ensure that the required current was being output into the rat leg, the amplitude of the input signal was modulated such that the output current would meet specifications when a resistor close to the value calculated above was at the load of the circuit. Although this calculated impedance was purely theoretical, it gave a good starting point for more accurate calibration which was achieved through testing on discard rats (Section 5.3.2s).

### 4.3.2 Tissue & Impedance Model

To obtain an approximation of the magnitude of the current that would be able to reach the bone for stimulation, an equivalent circuit model of the rat leg was developed. The first step to achieving the circuit model was to develop a tissue model combining the measured and published parameters mentioned above (Figure 15). The assumption in this model is that the bone is surrounded by all sides by muscle, and is in the center of pair of electrodes in the X direction. Additionally, the bone and muscle are assumed to be continuous along the Y direction for the length of the electrode (1 cm). Following these assumptions, Table 2 shows a summary of the dimensions of each tissue, and their resultant impedances. Using these impedances, an impedance model was developed representing the rat leg (Figure 16).

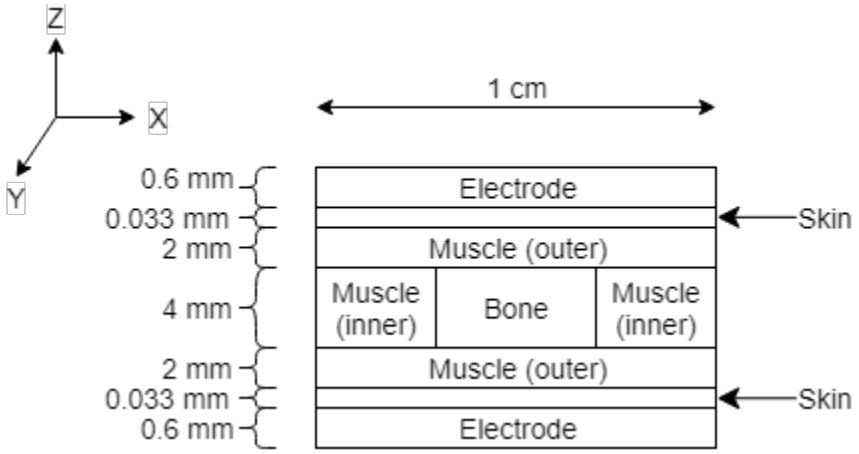


Figure 15: Model of the load attached to the circuit (not to scale)

| Tissue | Resistivity (Ω ∗m) | Dimensions (X x Y x Z mm) | Thickness (mm) | Area ($mm^2$) | Impedance (Ω) |
|---|---|---|---|---|---|
| Skin | 5000 | 10 x 10 x 0.033 | 0.033 | 100 | 1650 |
| Muscle (outer) | 4.89 | 10 x 10 x 2 | 2 | 100 | 97.8 |
| Muscle (inner) | 4.89 | 3 x 10 x 4 | 4 | 30 | 652 |
| Bone | 12.87 | 4 x 4 x 10 | 4 | 40 | 1287 |

Table 2: Tissue impedance values of the rat leg based on the model in Figure 15

### 4.3.3 Equivalent Circuit Model

Using the impedances calculated in Table 2 an equivalent circuit model was developed representing the leg of the rat between the electrodes (Figure 16). Here, $V_{SS}$ represents the voltage of the signal output through the electrodes, and $I_{Load}$ represents the current flowing through the rat leg. Using this circuit, the theoretical current that reaches the bone itself was calculated, to ensure the bone does not

undergo any detrimental effects due to having too high of a current as mentioned in literature, where a current density of 97 $\mu$A/cm$^2$ has been said to result in bone degradation (Isaacson & Bloebaum 2010). It is important to note that the total impedance of the circuit is 3755.7 Ω when following the model in Figure 16, while the total impedance of the circuit as calculated in Section 4.3.1 (which would be final load impedance minus the electrode impedance) is 4861.5 Ω. This discrepancy stems from the alternate dimensions of bone and muscle chosen in the more accurate model developed in this section, wherein the muscle surrounding the bone along the X axis has created a parallel pathway for current to flow with reduced impedance. Using this model, and selecting an $I_{Load}$ of 250 $\mu$A to be delivered to the rat leg, the total current that will reach the bone is approximately 63 $\mu$A. A full derivation of this calculation can be found in Appendix B**.**

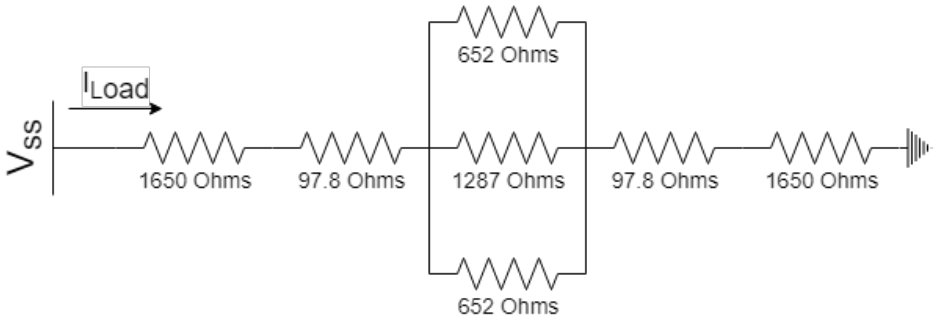


Figure 16: Equivalent circuit impedance model of the rat leg

# CHAPTER 5: CIRCUIT DESIGN & PERFORMANCE

## 5.1 CONSTANT CURRENT CIRCUIT

As mentioned in Section 4.1.1, the constant current circuit consists of an integrator circuit and a difference amplifier circuit. To create the integrator circuit, 1 of the 4 op-amps of the LT1014CN Quad Precision Operational Amplifiers by Texas Instruments (Dallas, United States) was used. The LT1014CN (Figure 17) was selected due to its low supply current (2.2 mA max), which would reduce its load on the power supply. This reduction in load is important as a single power supply was used to power 12 of such circuits concurrently, putting a high load on the power supply. The voltage rails of the op-amp were set to be $\pm$ 15 V and were generated using the Anatek (Santa Clara, United Stated) Model 25-2D power supply (Figure 18).

Figure 17: LT1014CN integrated circuit


Figure 18: Anatek Model 24-2D Power Supply

To create the difference amplifier circuit, the INA106KP (Figure 19) by Texas Instruments was used. This integrated circuit (IC) has a gain factor of 10 and is pre-packaged with resistors $R_1$ to $R_4$ from the circuit in Figure 11. Additionally, the resistors in the IC are laser trimmed for accurate gain and high common-mode rejection, which is crucial for ensuring that noise is not amplified and present in the output signal. The voltage rails for the INA106KP were set to $\pm$ 15 V, with the reference voltage being ground. A schematic and pinout diagram of this IC can be seen in Figure 20.


Figure 19: INA106KP integrated circuit

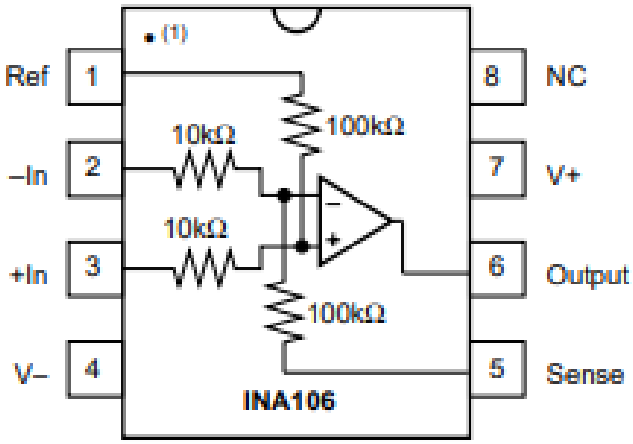


Figure 20: Pin configuration of the INA106KP

The amplitude of the current from the constant current circuit was chosen to be 250 $\mu$A, as testing amplitudes from 500 $\mu$A up to 2 mA showed the occurrence of muscle contraction in the rat leg, as well as tissue damage to the skin due to a high current density. Using Equation 1 and selecting an $R_{sense}$ of 1000 Ω, the ideal amplitude required by the signal generator was 2.5 V. Although this was the required amplitude, the true amplitude was selected by the calibration method, where the input voltage was modulated until the output current reached 250 $\mu$A at

the resistances predicted by the theoretical model in Section 4.3.3 and the resistances determined experimentally through testing on rats. To examine the output voltage, the Hewlett Packard (Palo Alto, United States) 54603B 60 MHz Oscilloscope (Figure 21) was used. For some tests, the Agilent (Santa Clara, United States) 54621A 60 MHz Oscilloscope was used (Figure 22).

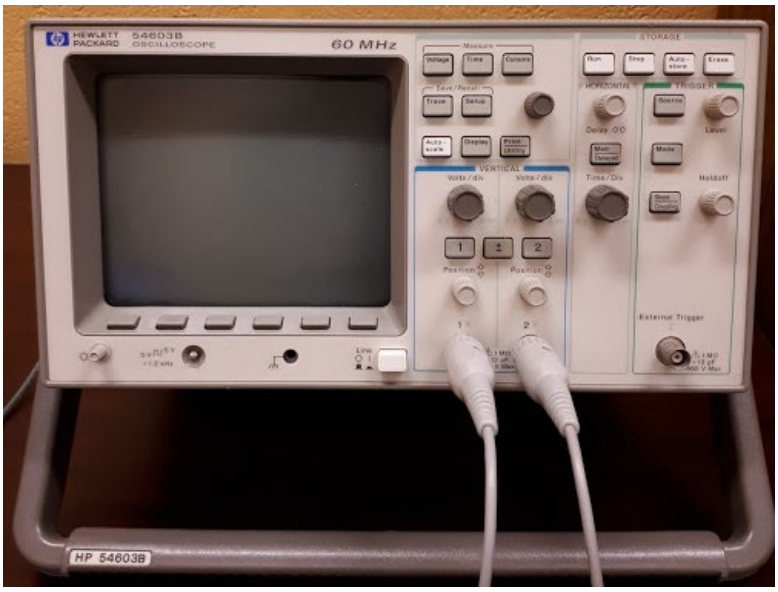


Figure 21: HP 54603B 60 MHz Oscilloscope

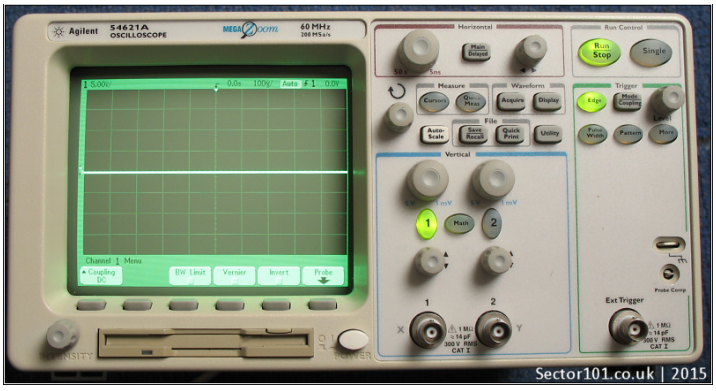


Figure 22: Agilent 54621A 60 MHz Oscilloscope

## 5.2 MICROCONTROLLER-BASED SIGNAL GENERATOR

### 5.2.1 Design

As mentioned in Section 4.1.2**,** the microcontroller-based signal generator used analog filtering to convert a square pulse of 15 Hz into a sinusoidal wave. The 3-stage LPF was chosen to have a frequency of 15 Hz, which was achieved by selecting capacitor $C_1$ to be 100 nF (due to this value being readily available), and hence resistor $R_1$ was selected to be 106490 Ω using Equation 3**.** Following the same logic, the capacitor $C_2$ of the HPF was chosen to be 1.1 $\mu$F, and resistor $R_2$ chosen to be 156 kΩ. The value of $R_3$ and $R_4$ varied with different tests as the voltage divider needed to be varied to achieve different amplitudes of the output signal.

The circuit was first tested at a frequency of 20 Hz, to examine the viability of the output signal in being a sine wave good enough to be used for experimentation. The goal of the signal generator was to be a pure sine wave so that we can infer that any effects from the electrical stimulation were due to that specific frequency of stimulation. Using a sine wave containing higher frequency harmonics would be detrimental to this goal as we would not be able to make conclusions related to any particular frequency. Figure 23 shows the input and output signals of the signal generator after and before the voltage divider. The top signal of each figure shows the output of the microcontroller, a square pulse of 20 Hz. The bottom signal of each figure shows the resultant sinusoidal signal after filtering the square wave. The amplitude of the output in the left figure can be seen to be 306 mV

($\Delta Y(2)$), while that on the right figure can be seen to be 3.5 V ($\Delta Y(1)$), showing the effects of the voltage divider having a divisor factor of approximately 10. It can be seen that the output sinusoid is not a perfect sine wave as compared to that of Figure 13 and seems to contain higher frequency content with characteristics of a triangular waveform.

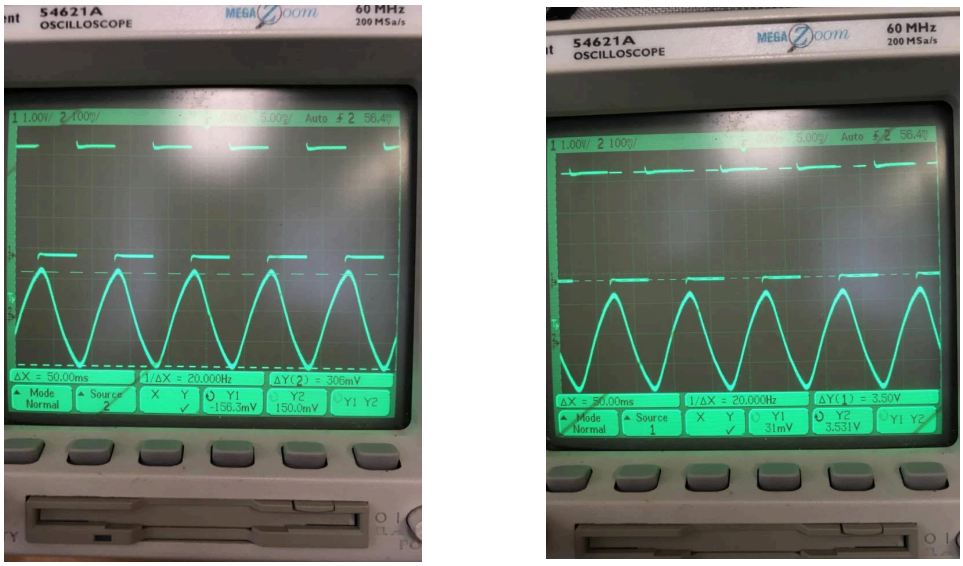


Figure 23: **A (left)** – Input (top) and output (bottom) signals after the voltage divider. **B (right)** – Input (top) and output (bottom) signals before the voltage divider

### 5.2.2 Performance

The performance of this signal generator in being able to provide the required current to output the specified constant current through the circuit in Section 4.1.1 was evaluated after design. To assess the performance, resistors of values ranging from 1,000 Ω to 20,000 Ω were placed at $R_{Load}$ in the circuit in Figure 11. The signal generator described here replaced the $V_{source}$ shown in the figure. For these tests a 275 mV input voltage amplitude (550 mV peak-to-peak)

was selected, along with a $R_{sense}$ of 100 Ω, and a gain factor of 10. Following these parameters and using Equation 1, the theoretical output current was calculated to be 275 $\mu A$. The actual output current was determined by looking at the peak-to-peak voltage across $R_{Load}$ and dividing that value by $R_{Load}$. Both the input and output voltages were monitored using 2 channels of the oscilloscope, to examine the variability in the voltage of the signal delivered by the signal generator as the load changes. Hence, Equation 5 shows the equation used to calculate the amplitude of the actual output current.

$$I_{out,actual} = \frac{V_{PP_{out}}}{2 * R_{Load}}$$

Equation 5: Calculation for the output current amplitude

A summary of this experiment can be seen in Table 3. As seen in the table, the output current remains relatively stable for low load resistances and is close to the theoretical calculated value of 275 $\mu A$. The circuit shows great behaviour when considering the rat leg resistance model shown in Section 4.3.1, as the current behaves as theoretically calculated around resistances of 10,000 Ω. At resistances of 20,000 Ω there was a decrease in the output current, which could indicate an inability of the microcontroller to provide the current required at this load. A sample oscilloscope output at an $R_{Load}$ of 10,000 Ω can be seen in Figure 24 where the voltage across $R_{Load}$ is approximately 5.53 $V_{pp}$, resulting in an output current with an amplitude of 276.5 $\mu A$. Figure 25 shows a graphical representation of the results

with an exponential curve being selected to fit the results due a greater $R^2$ value than other fitting models.

| $V_{PP_{in}}$ $(V)$ | $R_{Load}$ $(\Omega)$ | $V_{PP_{out}}$ $(V)$ | $I_{out,actual}$ $(\mu A)$ |
|---|---|---|---|
| 0.556 | 1,000 | 0.55 | 275 |
| 0.556 | 3,000 | 1.67 | 278 |
| 0.550 | 5,000 | 2.78 | 278 |
| 0.556 | 7,000 | 3.87 | 277 |
| 0.562 | 10,000 | 5.5 | 275 |
| 0.556 | 20,000 | 10.6 | 265 |

Table 3: Change in output current with load resistance

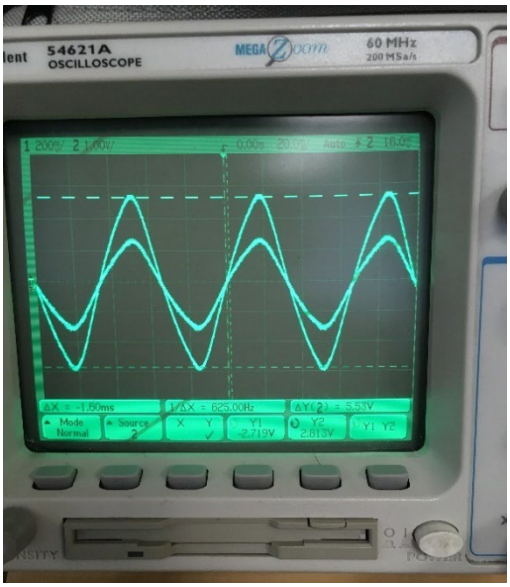


Figure 24: Signals showing the output of the signal generator and output of the constant current circuit

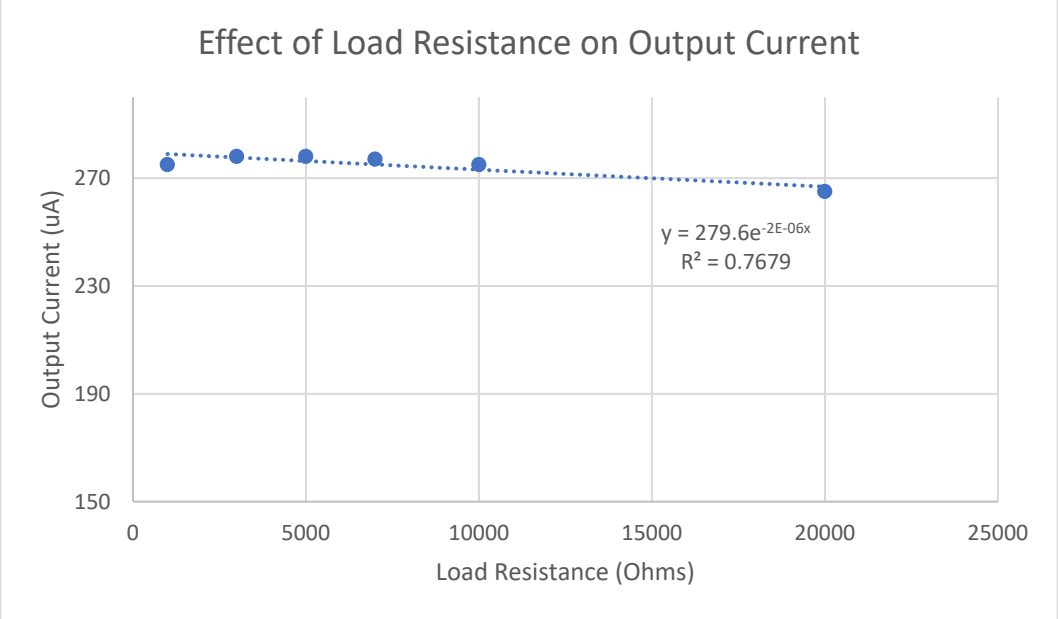


Figure 25: Effect of load resistance on output current

## 5.3 OFF-THE-SHELF SIGNAL GENERATOR

Due to the limitations of the microcontroller-based signal generator, namely the inability to produce a perfect sine wave, an off-the-shelf signal generator was used to produce the $V_{source}$ of the constant current circuit. The signal generator used was the BK Precision (Yorba Linda, United States) Model 3011B (Figure 26) due to its ability to produce a perfect sine wave at the frequency of interest, and variable amplitude for modulation of the output current. An example sin wave output directly from the signal generator can be seen in Figure 27, which shows a much closer resemblance to a perfect sine wave than the output of the microcontroller-based signal generator.


Figure 26: BK Precision Model 3011B signal generator

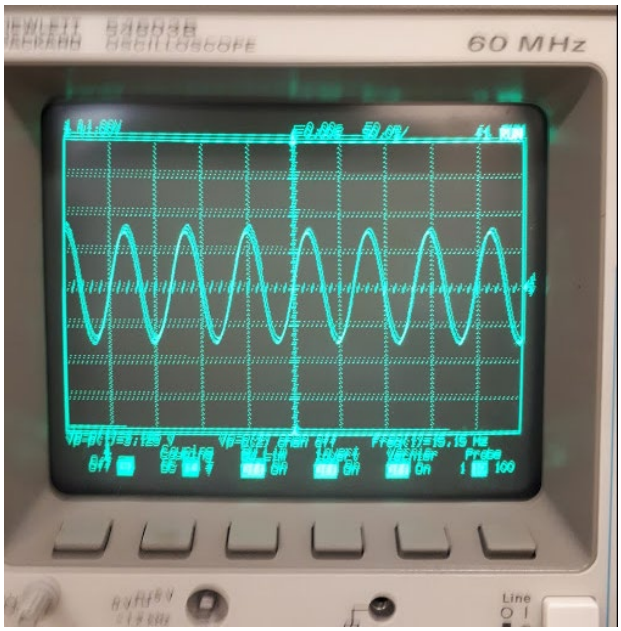


Figure 27: Signal showing the output of the off-the-shelf signal generator

### 5.3.1 Performance

The tests performed for the microcontroller-based signal generator in Section 4.1.2 Microcontroller-Based Signal Generator were also performed for the off-the-shelf signal generator. For these tests, the output current was calibrated such that at an $R_{Load}$ of 10,000 Ω the amplitude was 250 $\mu A$ as specified. At the oscilloscope, this corresponded to a peak-to-peak voltage of around 5 V across $R_{Load}$ for a peak-to-peak input voltage of 2.68 V. The output current was calculated in the same way as above using Equation 5**.** The results of these tests for an $R_{Load}$ ranging from 500 Ω to 50,000 Ω can be seen in Table 4. Figure 28 shows a graphical representation of the effects of load resistance on output current. When compared to the graph in Figure 25, we can see that the off-the-shelf signal generator experiences an 8.8% decrease in output current from a $R_{Load}$ of 10,000 Ω to 20,000 Ω, compared to only a 3.6% decrease experienced by the microcontroller-based signal generator. Although this performance is poorer, the decrease is still less than 10% over a large resistance range, making it still viable as the signal generator for experimentation. Additionally, this signal generator has the benefits of being able to output a pure sine wave compared to the microcontroller-based one.

| $\boldsymbol{R_{Load}}$ $\boldsymbol{(\Omega)}$ | $\boldsymbol{V_{PP_{out}}}$ $\boldsymbol{(V)}$ | $\boldsymbol{I_{out,actual}}$ $\boldsymbol{(\mu A)}$ |
|---|---|---|
| 500 | 0.266 | 266 |
| 1000 | 0.516 | 258 |
| 3000 | 1.609 | 268 |
| 5000 | 2.609 | 261 |
| 7000 | 3.547 | 253 |

| | | |
|---|---|---|
| 10000 | 5.016 | 251 |
| 15000 | 7.172 | 239 |
| 20000 | 9.175 | 229 |
| 30000 | 12.86 | 214 |
| 40000 | 15.98 | 200 |
| 50000 | 18.81 | 188 |

Table 4: Change in output current with load resistance calibrated at a load resistance of 30,000 Ohms

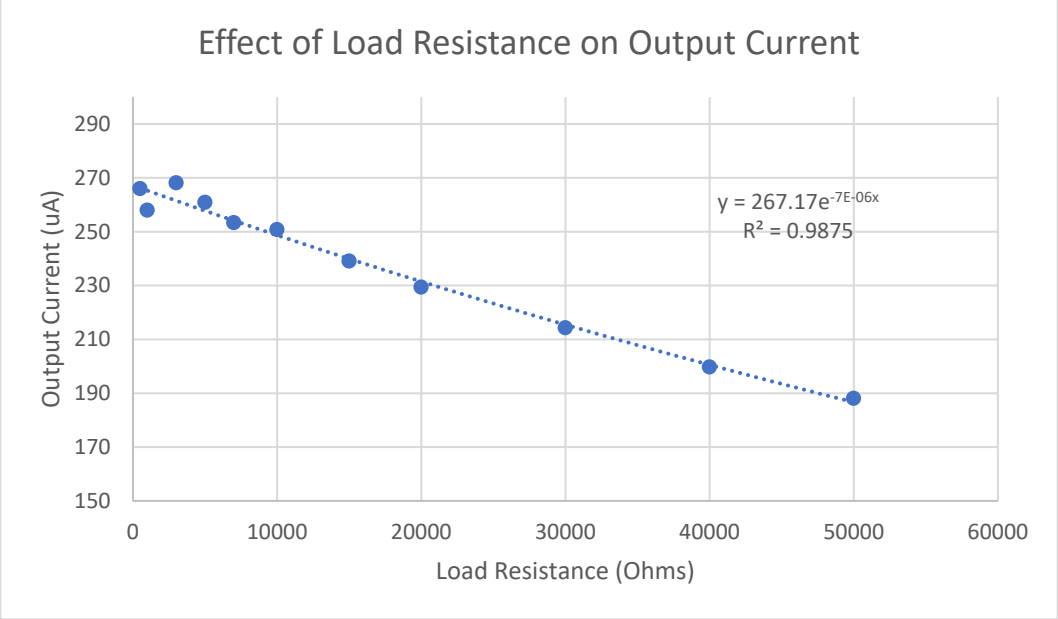


Figure 28: Effect of load resistance on output current

### 5.3.2 Animal Testing

All tests performed on animals were approved by the Animal Research Ethics Board at McMaster University. Once the performance of the two circuits was explored and the off-the-shelf signal generator was selected for use in the stimulation circuit, testing on test rats provided by the Central Animal Facility

(CAF) were performed. These tests were used to determine the capabilities of the circuit in providing enough voltage for the varying resistances of rat legs, determining the true approximate rat leg resistance, and determining the ability of the electrical stimulation circuit in providing the stimulation for an hour-long period.

Testing was performed on two female Sprague-Dawley rats and one female Wistar rat of ages ranging from 3 – 4 months. The rats were simultaneously anesthetized using gaseous anesthesia in an induction chamber, and then the anesthetized state was maintained using a custom anesthetic tube (details of the anesthetic device setup can be found in CHAPTER 6). The right leg of each rat was shaved as cleanly as possible with electric clippers and a razer. Electrodes were put on the leg surrounding the PTM with Spectra 360 electrode gel by Parker Laboratories (Fairfield, United States) (Figure 29). The electrodes were connected to the electrical stimulation circuit by insulated alligator clips from Kego Corporation (London, Canada) (Figure 30). One electrode was connected to the output of the circuit, and the other was connected to ground, which essentially replaced the $R_{Load}$ in Figure 11 by the rat leg. Figure 31 shows the electrical circuit connected to the rat leg.


Figure 29: Spectra 360 electrode gel

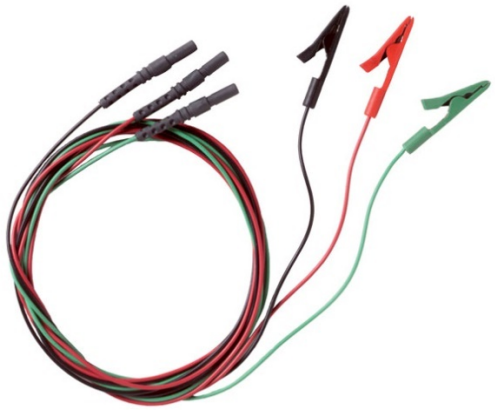

Figure 30: Insulated alligator clips from Kego Corp.

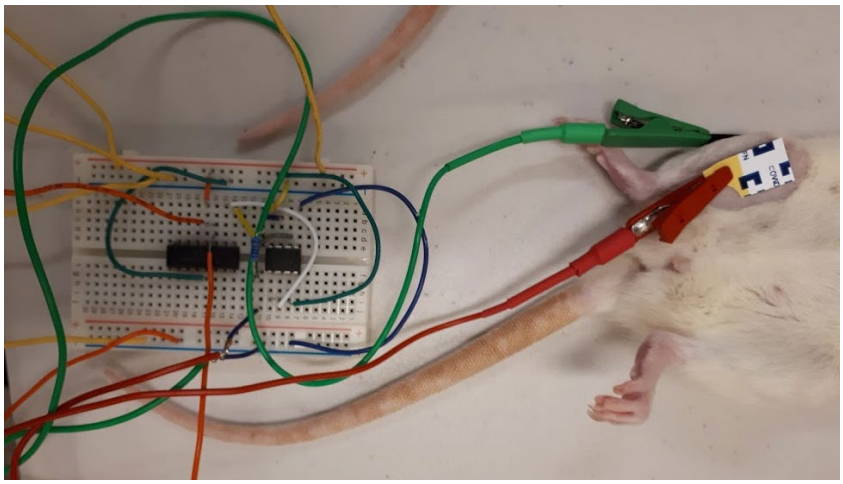

Figure 31: Electrical stimulation circuit connected to a shaved rat leg via electrodes

Figure 32 shows the setup of the test rats when performing the tests. The oscilloscope was used to track the voltage of the left-most and right-most rats. These two rats were tracked as they were of different species and size, which gave an indication on whether the leg impedance between rats of different species and sizes varied drastically. The voltage across the rat leg at the beginning of the tests can be seen in Figure 34, where channel 1 on the oscilloscope corresponds to the circuit attached to the right-most (black and white) rat, and channel 2 corresponds to the left-most (white). The peak-to-peak voltage of channel 1 can be seen to be 12.31 V, while that of channel 2 was 11.88 V. Since the output current was chosen to be approximately 250 $\mu A$, the resistances of the rat legs can be calculated to be 24,620 Ω and 23,760 Ω respectively. The main test to determine proper functionality of the circuit was to examine whether or not the output signal was saturated as shown in Figure 33. Since the voltage across $R_{Load}$ is limited by the voltage rails of the power supply (the circuit cannot output more voltage than it is

provided), saturation of the output signal would result in an output current much lower than the selected 250 $\mu A$, which would reduce the effectiveness of the stimulation. This could occur in cases where the rat leg resistance was much larger than expected, an electrode has fallen off, or there is improper adhesion between the leg and electrode due to an inadequate amount of electrode gel used. If the output signal resembles a pure sinusoid as expected from the output of the function generator, then the current delivered to the rat leg is as expected.

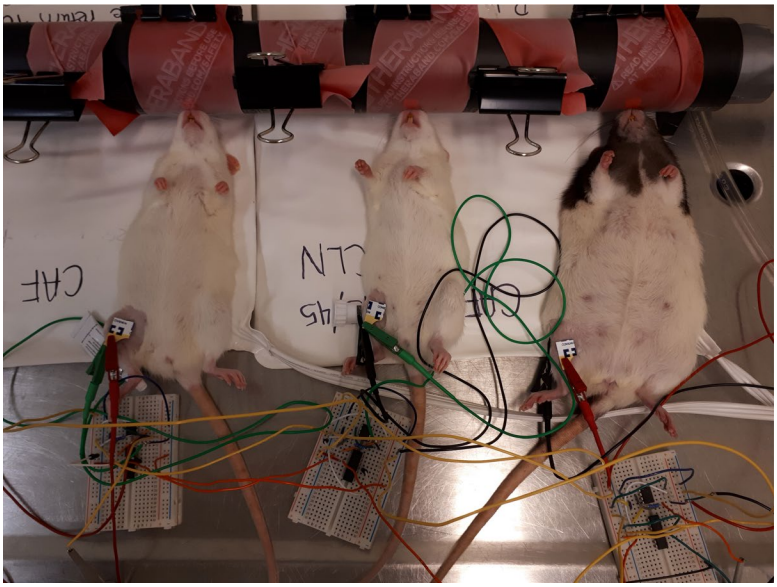

Figure 32: 3 discard rats attached to electrical stimulation circuits

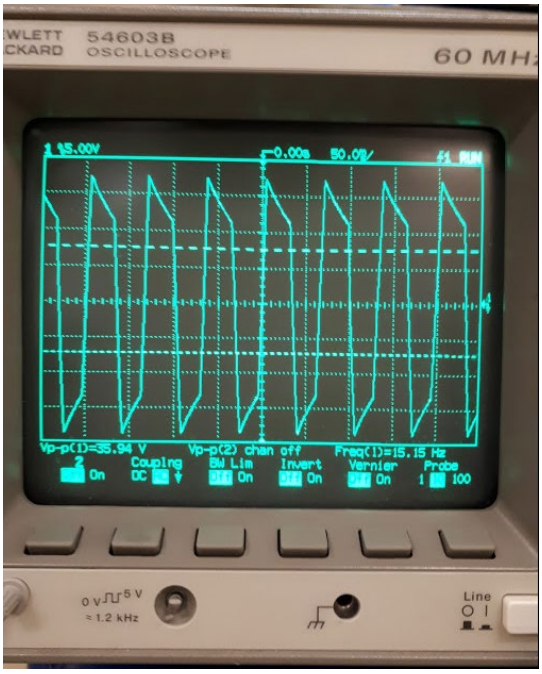


Figure 33: Oscilloscope output showing a saturate output signal due to an electrode falling off

Figure 34 also shows the output of the oscilloscope near the end of the test, at minute 50 of stimulation. As seen in the image, the voltage across the leg of the left-most rat remained fairly constant (peak-to-peak voltage of 11.25 V). The voltage across the leg of the right-most rat experienced a more drastic change, decreasing from a peak-to-peak voltage of 12.81 V down to 7.344 V. This change could have been due to the fact that this rat was pulled out of the anesthetic tube a few minutes prior to taking the picture because its heart rate was much lower compared to the other two, indicating an over-administration of the anesthetic. Removing the rat may have caused physiological changes in the leg as the rat experienced increased heart rate and waking from its deep sleep state. Additionally,

the electrodes may have experienced movement, and the output voltage has a strong relationship with the position of the electrodes.

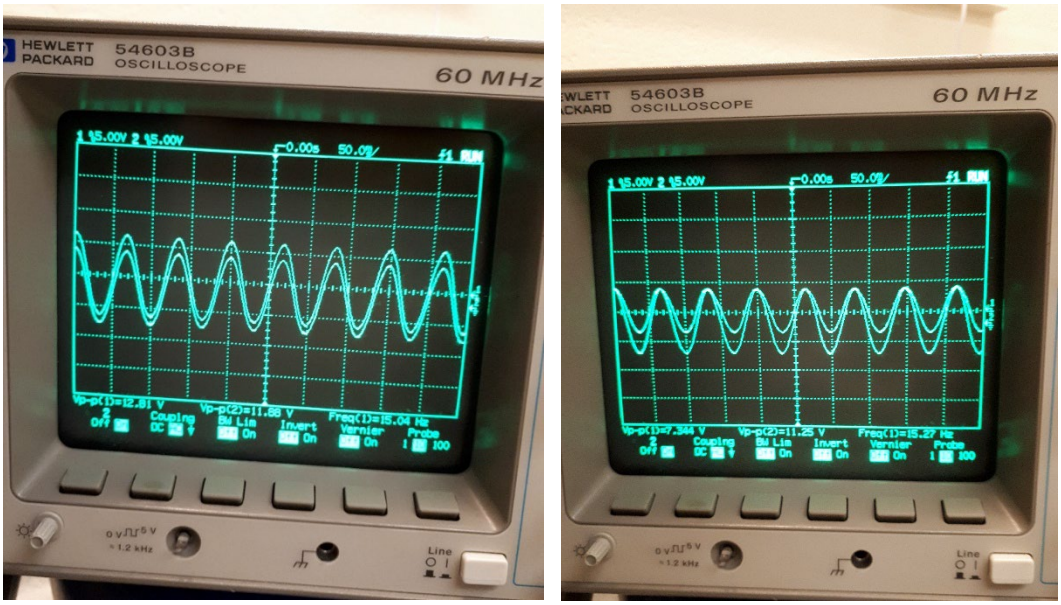


Figure 34: Oscilloscope output at time = 0 (**left**) and time = 50 minutes (**right**). Channel 1 corresponds to the right-most rat, channel 2 corresponds to the left-most rat.

Following these experiments and realizing that the rat leg resistance predicted by the model in Section 4.3.1 was incorrect, the circuit was calibrated at a load resistance of 30,000 Ω and its performance was compared to the calibration at 10,000 Ω. At the oscilloscope, this corresponded to a peak-to-peak voltage of around 15 V across $R_{Load}$ for a peak-to-peak input voltage of 3.1 V. The output current was calculated in the same way as above using Equation 5**.** The results of these tests for an $R_{Load}$ ranging from 500 Ω to 50,000 Ω can be seen in Table 5. Figure 35 shows a graphical representation of the circuit's behaviour. As seen in the graph, calibrating the circuit for an $R_{Load}$ of 30,000 Ω simply shifts the curve by a certain current. Looking at the exponential curve fit we can see that the decay

in output current with increasing $R_{Load}$ remains constant, indicating that the circuit will behave appropriately as it did with the previous calibration.

| $\boldsymbol{R_{Load}}$ $(\boldsymbol{\Omega})$ | $\boldsymbol{V_{PP_{out}}}$ $(\boldsymbol{V})$ | $\boldsymbol{I_{out,actual}}$ $(\boldsymbol{\mu A})$ |
|---|---|---|
| 500 | 0.316 | 316 |
| 1000 | 0.6 | 300 |
| 3000 | 1.831 | 305 |
| 5000 | 3 | 300 |
| 7000 | 4.191 | 299 |
| 10000 | 5.847 | 292 |
| 15000 | 8.319 | 277 |
| 20000 | 10.76 | 269 |
| 30000 | 14.94 | 249 |
| 40000 | 19 | 238 |
| 50000 | 22.28 | 223 |

Table 5: Change in output current with load resistance, calibrated at a load resistance of 30,000 Ohms

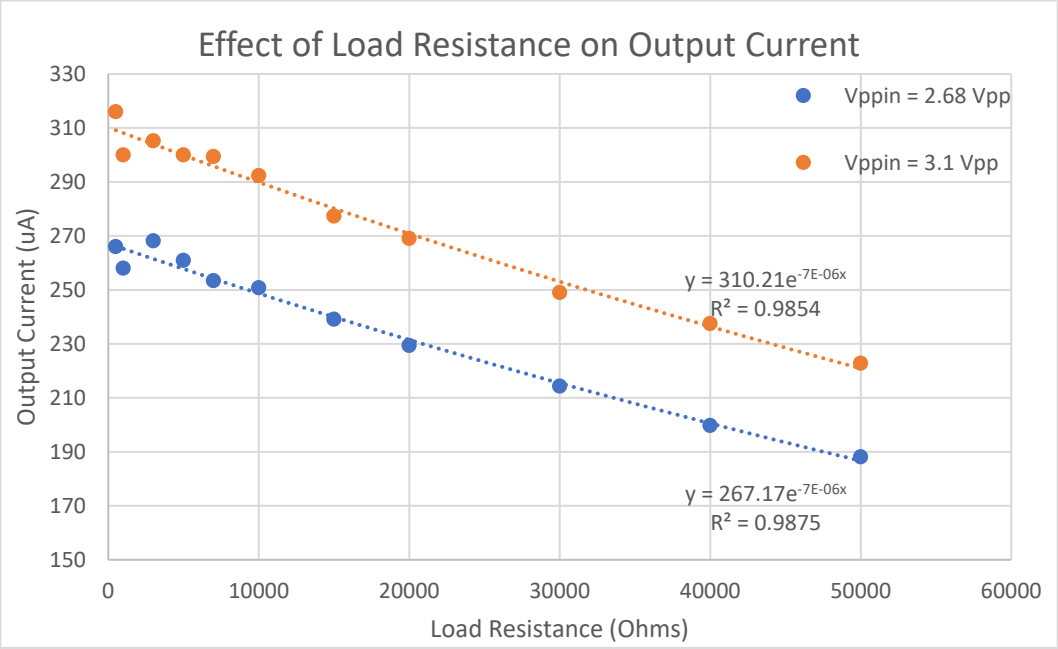


Figure 35: Effect of load resistance on output current

Once the circuits were calibrated for a 30,000 Ω load resistance, additional testing on test rats was performed. In these tests, the oscilloscope monitored the circuits attached to the same rats as previously to ensure consistency. This time, the voltage across the leg of the white (left-most) rat in Figure 32 was shown in channel 1 of the oscilloscope, while that of the black and white (right-most) rat was shown in channel 2. The peak-to-peak voltage of channel 1 can be seen to be 16.25 V, while that of channel 2 was 15 V. Since the output current was again chosen to be approximately 250 $\mu A$, the resistances of the rat legs can be calculated to be 32,500 Ω and 30,000 Ω respectively. Figure 36 shows the output of the oscilloscope near the end of the test, at minute 50 of stimulation. As seen in the image, the voltage across the legs of both rats remained fairly constant (peak-to-peak voltages of 14.69 V and 16.09 V respectively). Importantly, the black and white rat was once again

removed from the anesthetic tube a few minutes prior to taking the second oscilloscope picture, but the voltage across the leg was not affected significantly as it was previously. This could discredit the previous statement on physiological changes occurring in the leg due to the rat entering an increasingly-waking state and support the statement that there was movement of electrodes.

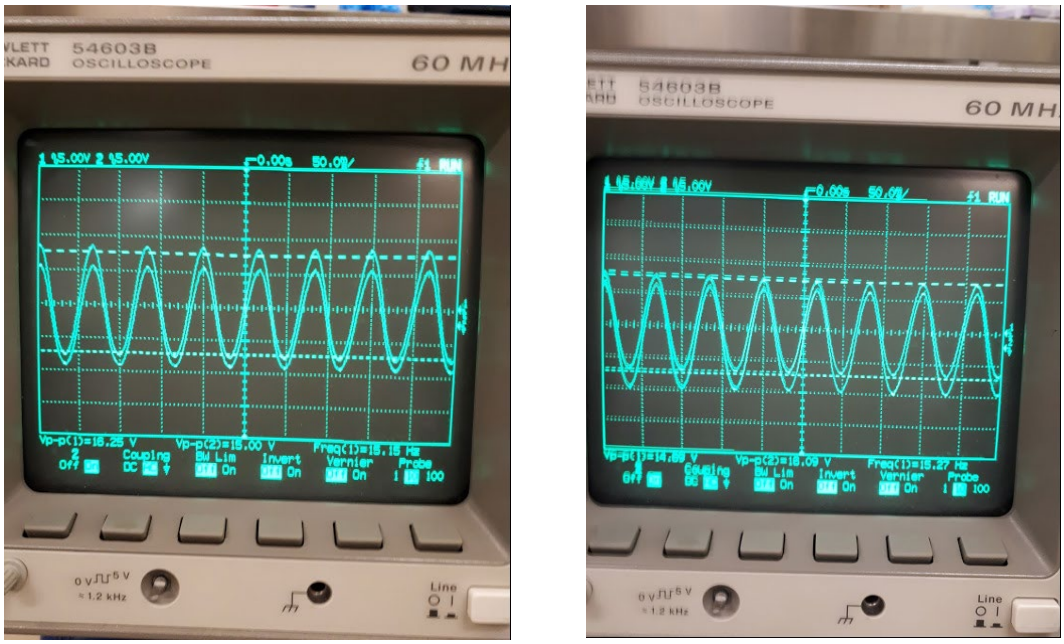


Figure 36: Oscilloscope output at time = 0 (**left**), and time = 50 minutes (**right**). Channel 1 corresponds to the left-most rat, channel 2 corresponds to the right-most rat

Table 6 shows a summary of the voltages, resistances, and currents from the two calibrated circuits and corresponding animal tests. During the calculation of the resistances of the rat leg when the circuit was calibrated for 10,000 Ω, the flaw was that the output current was assumed to be 250 $\mu A$. Looking at the decay in current with increase load resistance as shown in Figure 28, the output current would be lower. Hence, to calculate what the true resistance of the rat leg would be during

these tests, the resistance of the rat leg calculated using the tests calibrated for a 30,000 Ω load resistance was used for each rat. The true output current according to this resistance was determined using the fitted curve in Figure 35, and then the true rat leg resistance was once again calculated by using the output voltages measured in the tests. Using this method, the white and black & white rats were determined to have leg resistances of 27,914 Ω and 29,833 Ω, compared to resistances of 23,760 Ω and 24,620 Ω respectively. With the newly calculated 10,000 Ω resistances and considering the 30,000 Ω calibrated resistances, we can see that the true resistance of the rat leg ranges between 27,000 Ω and 33,000 Ω, with the majority of discrepancy in resistance calculations coming from the amount of electrode gel used on each electrode.

| **Calibrated Load (Ω)** | **Rat** | **Measured Output Voltage ($V_{pp}$)** | **Calculated rat leg resistance[1] (Ω)** | **True Current at calculated resistance[2] ($\mu A$)** | **True rat leg resistance (Ω)** |
|---|---|---|---|---|---|
| 10,000 | White | 11.88 | 23,760 | 212.8 | 27,914 |
| 30,000 | White | 16.25 | 32,500 | 247.1 | 32,881 |
| 10,000 | Black & White | 12.31 | 24,620 | 216.6 | 28.416 |
| 30,000 | Black & White | 15 | 30,000 | 251.4 | 29,833 |

[1]Assuming a 250 $\mu A$ current delivered

[2]Determined via the fitted curve in Figure 35, for the 30,000 Ω calibration of each rat

Table 6: Summary of the animal model experiments

# CHAPTER 6: ANESTHETIC DEVICE

One of the limitations in the early stages of the project was that the anesthetic machines can only anesthetize a single rat at a time. This was not ideal for these experiments because our sample size consisted of 30 rats to be stimulated daily. The experimental protocol required stimulation on each rat for 1 hour/day for 6 weeks, resulting in a total stimulation time of 30 hours/day, which was not possible. Hence, we developed a custom anesthetic device consisting of an induction chamber and a tube able to keep up to 6 rats anesthetized simultaneously. This reduced the experimentation time to about 5-6 hours/day. Additionally, we developed 2 of the anesthetic tubes which allowed the stimulation of 12 rats simultaneously, allowing a further reduction in experimentation time.

## 6.1 INDUCTION CHAMBER

To put the rats in an anesthetized state, a custom induction chamber had to be developed that was capable of holding up to 6 rats at a time. The box itself was made of ¼" clear acrylic plastic from P&A Plastics Inc (Hamilton, Canada). The sheets of plastic were cut using a laser cutter from the mechanical engineering department. The laser cut tabbed box program of the Inkscape software was used to develop the model to be cut by the laser cutter. The box also included an inlet connection and an outlet connection. The inlet was created by tapping a ¼" NPT screw hole into one side of the box, and then 3-D printing a ¼" NPT to 0.6" adapter (Figure 37). The adapter was necessary because the anesthetic vaporizer used to

turn the isoflurane liquid to gas was obtained from the CAF and used a 0.6” hose to output the gas from the vaporizer. The outlet was created similarly, by tapping a ¾” NPT screw hole into the opposite side of the box. To implement the scavenger, a ¾” barbed fitting (Figure 38) was purchased from Canadian Tire. Figure 39 and Figure 40 show the final assembled induction chamber along with the corresponding adapter attached to the walls of the chamber.

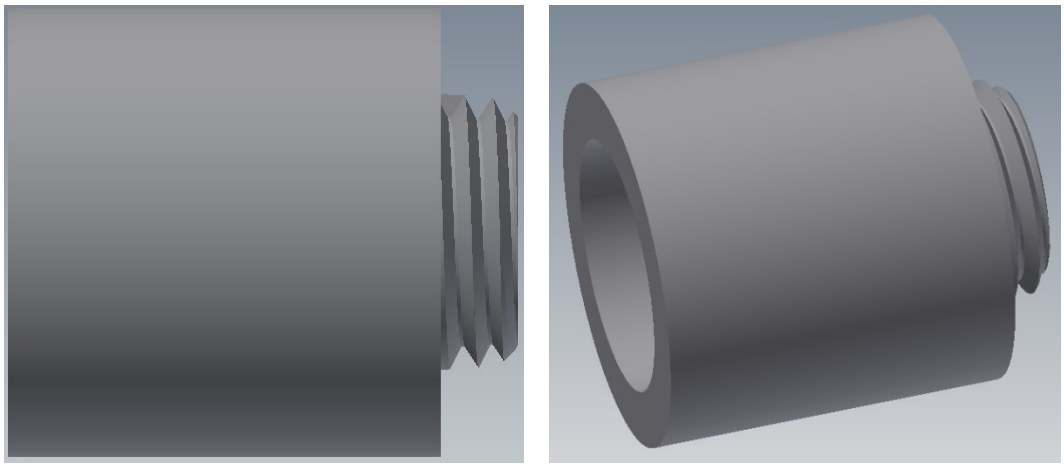

Figure 37: 3D model of the inlet adapter. **Left** – side view. **Right** – angled view

Figure 38: ¾” barbed fitting attached to the box

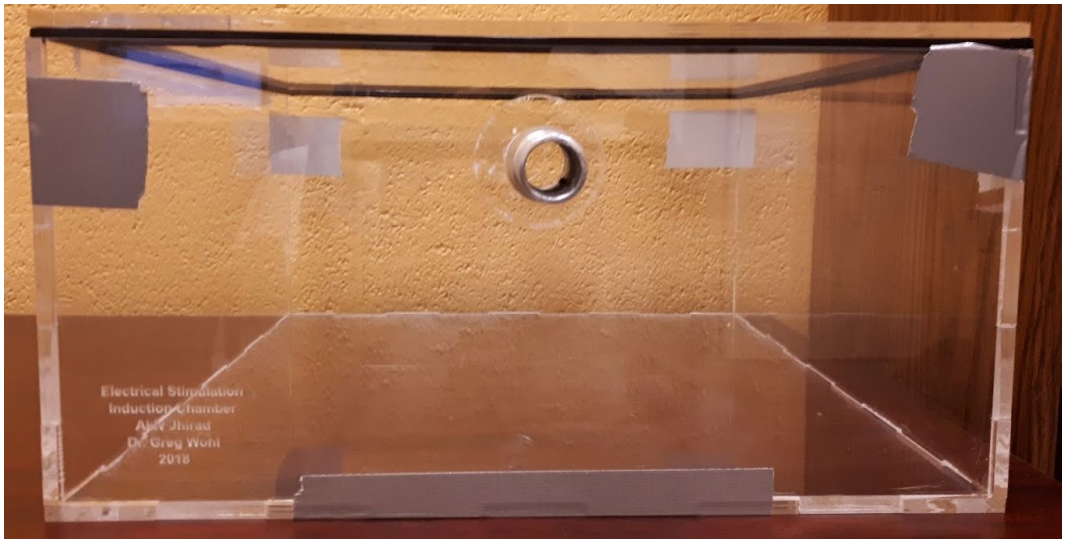


Figure 39: Assembled induction chamber

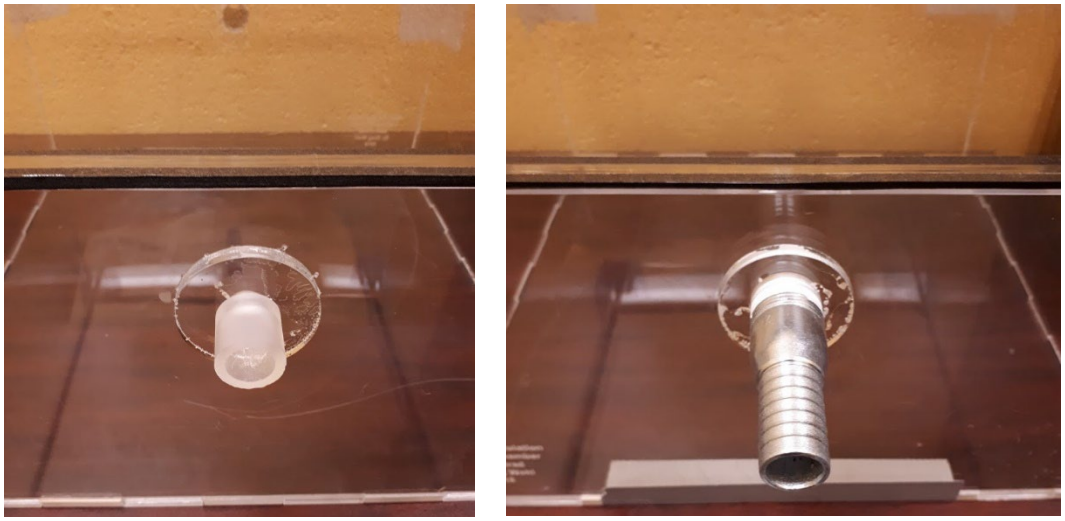

Figure 40: Adapters attached to the induction chamber. **Left** – ¼" NPT adapter. **Right** – ¾" NPT barbed fitting

## 6.2 MULTI-RAT ANESTHETIC TUBE

To maintain the anesthetic states of the rats, a custom anesthetic tube was developed that was capable of keeping up to 6 rats anesthetized simultaneously after being induced in the chamber. The tube is made of an ABS plastic pipe of 2"

diameter, with 3 holes drilled into the tube 6” apart to ensure there is enough space for each rat to lay down in side-by-side. On the other side, 3 more holes were drilled in a similar manner, but offset by 2” horizontally from the holes on the previous side. The staggering of the holes on both sides ensures that 2 rats are not inhaling anesthetic gas at the same points within the tube, which ensures that each rat is able to get enough gas. A schematic of holes made in the tube can be seen in Figure 41.

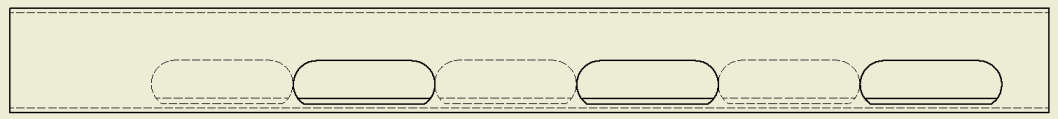

Figure 41: Schematic of the anesthetic tube with holes displayed

Next, to ensure that there was no unnecessary gas escaping through the tube, and that there was a proper way for the noses of rats to be inserted into the hole of the tube, latex resistance bands (Figure 42) from Thera-Band (Akron, United States) with holes cut in them were used. These bands were tightly wrapped around the diameter of the tube surrounding the position of each hole and attached to an ABS add-on on the top of the tube by a paper clip. The latex band was wrapped taut such that there would be no gaps between the band and the tube, ensuring that the only gas that escapes is through the small hole cut into the band. The holes cut into the band were approximately 1 cm in diameter, allowing just enough space for the rat nose to be inserted. An image of this implementation can be seen in Figure 43, with one side of the tube assembly shown in Figure 44.


Figure 42: Latex bands used for covering holes in the tube

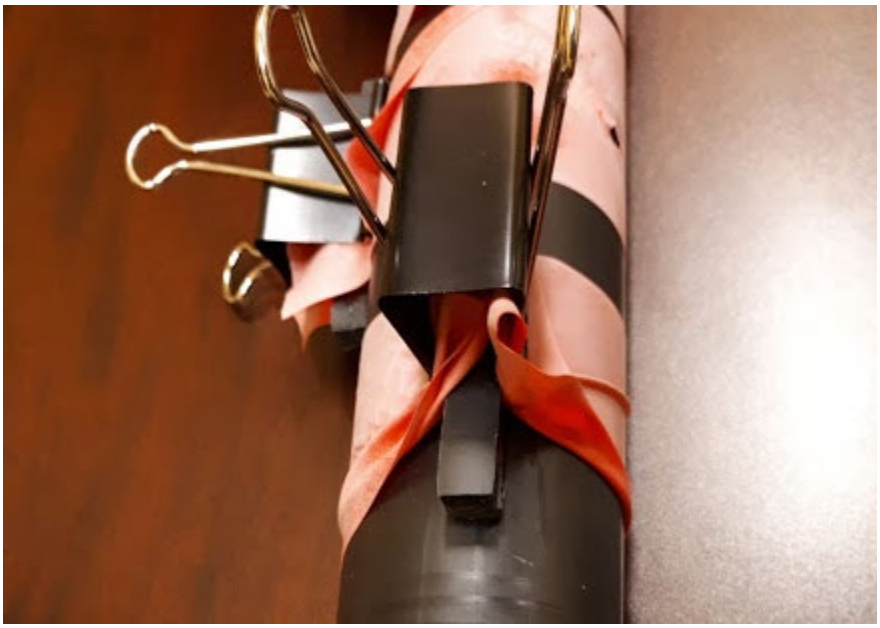

Figure 43: Portion of the tube showing the ABS attachment, paper clip, and wrapped latex band

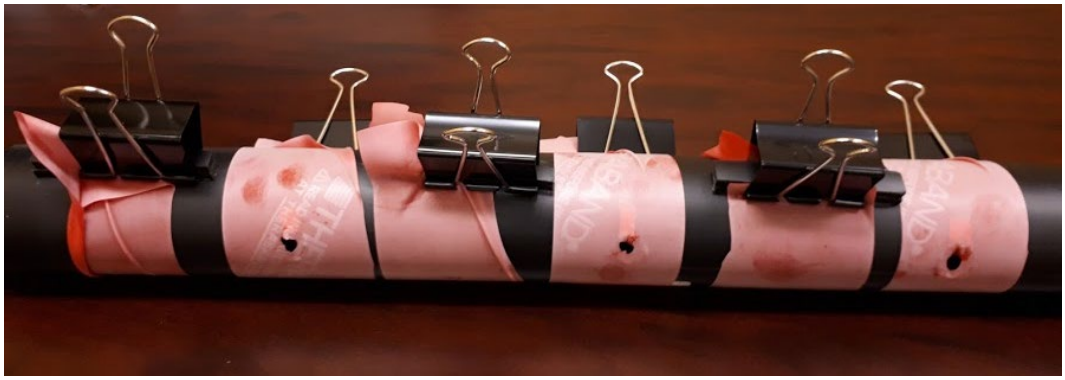

Figure 44: One side of the anesthetic tube showing the latex band implementation with holes cut out to allow rats noses to be inserted

To make the input and output holes of the tube compatible with the anesthetic machines provided by the CAF, adapters were 3D printed. These adapters were designed to have an inner hole diameter of approximately 0.6” to be compatible with the anesthetic output of the machine, with an outer hole diameter of 0.8” to be compatible with the scavenger hose that goes out to the ventilation for clearance of the gas. The other end of the adapter was designed to have an outer diameter of 2” to allow it to be inserted into the tube itself. This allows for gas to flow directly from the output of the anesthetic machine into the tube. This adapter was also placed at the other end of the tube to allow the scavenger pipe to be attached. Figure 45 shows various views of the adapter designed in Autodesk, while Figure 46 shows an image of the adapter inserted into the tube. This image also contains an additional adapter required for some of the anesthetic machines, which takes input from a 0.25” hose.

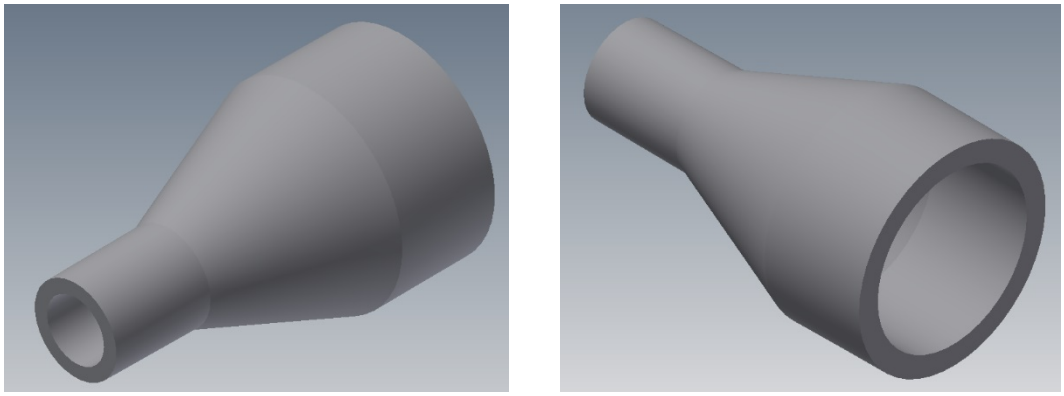

Figure 45: 3D model views of the tube adapter

Figure 46: Portion of the tube showing the input adapter inserted

Finally, there needed to be considerations on limiting the flow inside the tube to ensure that the anesthetic gas is not being scavenged out too quickly, and to ensure that changes to this scavenge rate can be made. The rate was limited by implementing a flow restrictor (Figure 47) at one end of the tube that forces the gas

to flow through a hole of diameter 0.75”, increasing the time that the gas remains in the tube. Additionally, at the scavenging end of the tube, an elongated hole was drilled into the top, which can be closed off by the adapter at that end by any amount appropriate for the rate of scavenging required. This allows control over how much time the anesthetic gas spends in the tube, which can be varied depending on the physiological state of the rats. The flow restrictor and scavenger end can be seen in Figure 48.

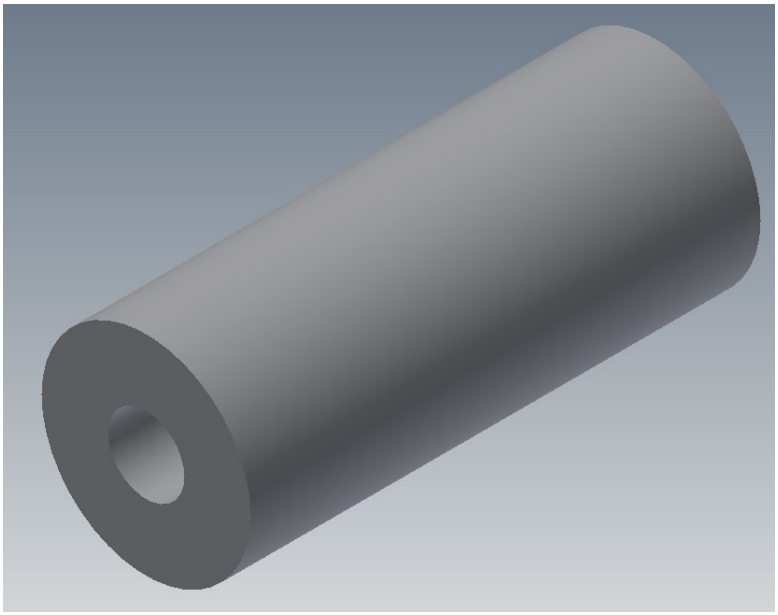

Figure 47: Flow restrictor

Figure 48: Portion of the tube showing flow restrictor and scavenging rate control hole

The complete multi-rat anesthetic tube can be seen in Figure 49 below.

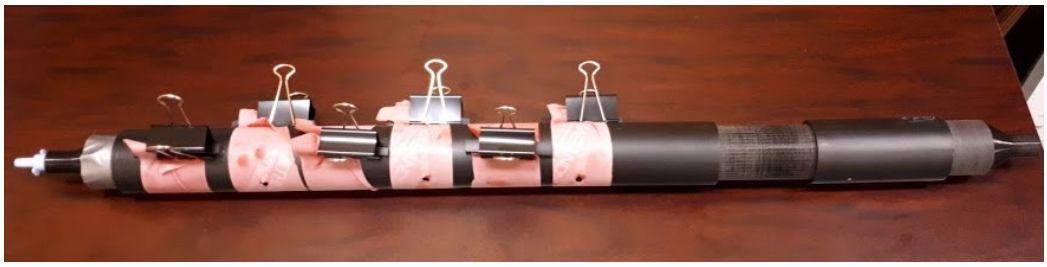

Figure 49: The multi-rat anesthetic tube

# CHAPTER 7: EXPERIMENTAL METHODS

## 7.1 EXPERIMENTAL ANIMAL GROUPS

The OVX rat model was selected due to its wide acceptance for age-related bone loss studies, and for the similarity in estrogen depletion that it experiences in relation to human beings (Jee & Yao 2001). Thirty SPF (special Pasteurella-free) female Sprague-Dawley rats (12-13 weeks old) were obtained from Charles River (Saint Constant, QC) on May 22$^{nd}$, 2018.

Fifteen of these rats underwent the OVX procedure (OVX group), and 15 underwent a sham procedure in which the OVX surgery was performed but the ovaries remain in the body (SHAM group). The procedures were performed on May 17th, 2018 by Charles River. Each cohort (OVX and SHAM) was randomly separated into: a group (n=6 / group) that did not undergo the electrical stimulation treatment (OVX + NOSTIM, and SHAM + NOSTIM), a group (n=6 / group) that underwent the electrical stimulation treatment (OVX + STIM, and SHAM + STIM), and a group (n=3 /group) that was sacrificed 1 day before the experimental period begins to obtain baseline bone density results (OVX BASELINE, and SHAM BASELINE). Additionally, each non-stimulated group was split into: a group (n=3) that had electrodes and the circuit attached with power (OVX/SHAM + NOISE), and a group (n=3) that only had electrodes attached (OVX/SHAM + NOSTIM). After the initial day of stimulation some changes were implemented, which are detailed below. The sample sizes of each group were selected to be similar to previous studies performed using comparable treatment methods, where the sample sizes ranged from 5 to 8 (Fredericks 1999; Mcleod & Rubin 1992; Brighton, Katz, et al. 1985). A summary of the groups, the sample sizes of each group, and how each group was identified is shown in Table 7**.** Each rat was also provided with a unique number from 1 to 30 for more simple identification.

| **Group** | | **Sample Size** | **Identification Marker** |
|---|---|---|---|
| OVX | STIM | 6 | Red, 2 stripes |
| OVX | NOISE | 3 | Black, 2 stripes |

| | | | |
|---|---|---|---|
| OVX | NOSTIM | 3 | Blue, 2 stripes |
| OVX | BASELINE | 3 | No Marking |
| SHAM | STIM | 6 | Red, 1 stripe |
| SHAM | NOISE | 3 | Black, 1 stripe |
| SHAM | NOSTIM | 3 | Blue, 1 stripe |
| SHAM | BASELINE | 3 | No Marking |
| **Total** | | 30 | |

Table 7: Summary of the experimental groups

The first day of experimentation was on June 4$^{th}$, 2018 (day zero at 18 days after OVX or SHAM surgery), to allow enough time for acclimatization of the rats to the new environment, healing of the surgical wound, and removal of the surgical clips (Figure 50) using forceps with specialized hooks obtained from the CAF (Figure 50). After the first day of testing, a skin lesion was found on rats belonging to the NOISE group (shown in Figure 51). This lesion showed necrotic cells, indicating that the site may have been burnt by the electrical stimulation. This burning was due to the fact that even though there was no electrical signal put through the electrodes, there was an inherent low amplitude DC signal due to the connected power supply. Although the amplitude was low, a stimulation period of 1 hour seems to have been long enough to induce a lesion in the leg of the rat. No rats from the STIM group showed any lesions similar to that experienced by the NOISE group. Following this finding, the NOISE group were not attached with electrodes connected to a power supply, and hence underwent the same treatment as the NOSTIM group. The lesions on the two NOISE rats healed and there were

no complications with the lesions. The animal legs were included in all analyses. Additionally, two rats died due to an overexposure of anesthetic during the 1-hour treatment. Hence, these two rats were taken to be baseline rats, while two of the original baseline rats were marked as replacements for the dead rats. The baseline rats were sacrificed on the second day of experimentation, on June 5$^{th}$, 2018. The overall experimental timeline can be seen in Figure 52.

Figure 50: **Left** – surgical clips on the back of a rat. **Right** – tweezers used to remove the clips.

Figure 51: **Left** - lesion on a SHAM + NOISE rat. **Right** – lesion on an OVX + NOISE rat.

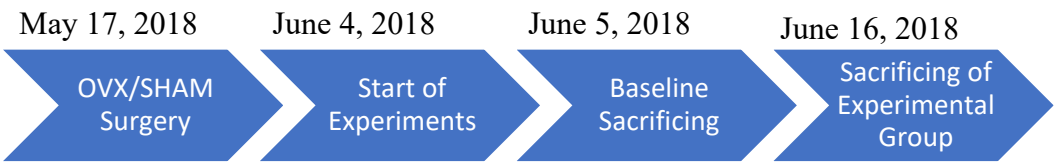


Figure 52: Experimental timeline.

## 7.2 STIMULATION PROTOCOL

The electrical stimulation was carried out via capacitive coupling stimulation using the constant current circuit as described in Section 4.1. The current was delivered using 1 cm x 1 cm ECG electrodes (Covidien, United Kingdom) across the right knee joint of the rat, to encompass the PTM. The left knee joint did not undergo the electrical stimulation treatment and served as an internal paired control. The electrical stimulation used a 15 Hz frequency sinusoid with a 250 $\mu$A amplitude as calibrated and tested in Section 5.3**.** This signal was

also tested to ensure no muscular contractions were being induced, and no damage to the skin was present over a 1-hour period.

The electrodes were attached to the legs of each rat using a folded-up paper clip, which provided just enough compression on the electrodes to hold them in place. Since the clips may induce lateral forces on the bone which may have an effect on bone growth, they were also used to attach the electrodes onto the legs of the non-stimulated groups (Figure 53).

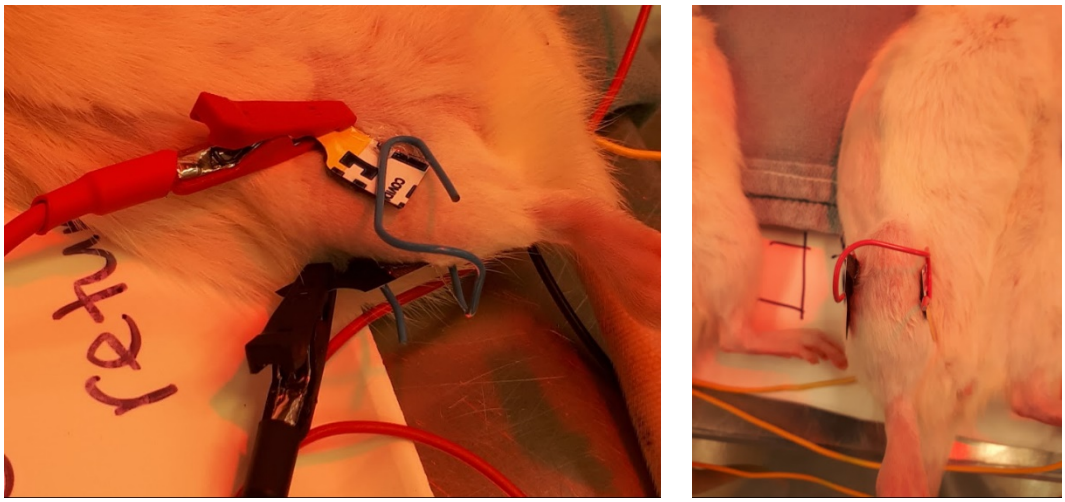

Figure 53: **Left** – electrodes and clip attached to STIM rat. **Right** – electrodes and clip attached to NOSTIM rat.

Six rats were anesthetized simultaneously via gaseous anesthesia using isoflurane in the induction chamber described in Section 6.1. The rats were then transferred to the anesthetic-maintenance tube (Section 6.2) with their noses placed inside and bodies exposed, allowing the attachment of the electrodes. The anesthetic protocol followed is listed in Appendix D, with Figure 54 showing the configuration of the rats**.** The right legs of each rat were shaved cleanly to ensure

proper adhesive contact of the electrodes, and electrode gel was used to reduce the electrode-skin impedance boundary. The electrical stimulation treatment was administered for 1 hour each day, 5 days a week, for 6 weeks. The OVX/SHAM + NOISE group were supposed to have had the electrodes attached in the same manner as those in the treatment group, with the stimulation circuit not connected to the function generator but following the finding of the lesions as shown above the power supply was also disconnected and the same application as that of the OVX/SHAM + NOSTIM was used. The original idea behind the NOISE group was that since the circuit will still be attached to the power supply, it would determine whether the high-frequency, low amplitude power supply noise had an effect on the effects of the stimulation without the signal of interest. This protocol is similar to that used by McLeod et. al (Mcleod & Rubin 1992) to assess the effects of low frequency PEMF on disuse osteopenia in the immobilized turkey ulnae.

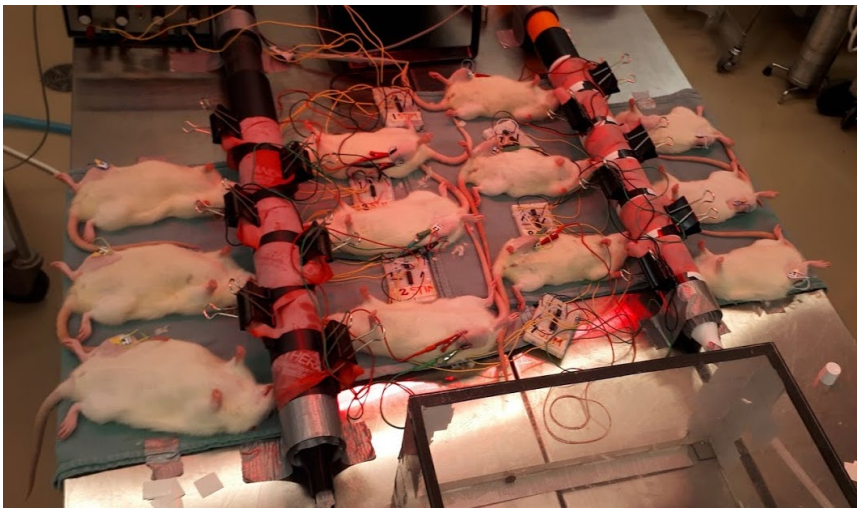

Figure 54: Two anesthetic tubes running simultaneously, with 6 rats each

An oscilloscope was used at the start of each stimulation period to ensure the electrical signal is within the voltage rails of the power supply, which was used to determine proper delivering of the stimulation current. As mentioned in Section 5.3.2 Animal Testing, if the resistance of the rat leg is too high, or the electrodes are not properly attached to the leg, the signal amplitude will exceed the maximum allowed by the power supply and undergo clipping, which would reduce the current delivered to be lower than specified.

# CHAPTER 8: POST-EXPERIMENT METHODS

## 8.1 BONE EXTRACTION

All 24 remaining rats used during experimentation were sacrificed using $CO_2$ induction on July 16$^{th}$, 2018, 3 days following the final day of experiments. The dissection was carried out using a size 3 scalpel handle and a size 15 scalpel blade. Disarticulations at the hip joint, knee joint, and foot joint were performed to isolate the femur and tibia. Lastly, as much muscle as possible was dissected off the bones, with care being taken not to scratch the surface of the bone so cortical bone does not get removed. Each pair of bones from one leg was wrapped in a gauze doused in 70% ethanol, and then stored in a 15 ml falcon tube with a label indicating the number of the individual rat. Each tube held all 4 bones of each rat. A pair of dissected bones can be seen in Figure 55**.**

Figure 55: Tibia and fibula of the left leg (left) and femur of the left leg (right).

## 8.2 MICRO-CT SCANNING

Micro-CT scanning was carried out using the Skyscan 1172 X-Ray Microtomograph (Bruker-microCT, Belgium) available for use at the McMaster Automotive Resource Centre (MARC). The proximal tibia and distal femur from the left and right legs of each individual rat were scanned simultaneously. A medium camera was used for a resolution of 13.1 $\mu$m in all 3 dimensions with a rotation step size of 0.5, an X-Ray beam of 89 kV and 112 $\mu$A, and a beam exposure time of around 2010 ms. A 0.5 mm Aluminum filter was used to decrease the noise effects of low-energy photons and reduce the effects of beam hardening (Bouxsein et al. 2010). To differentiate between the right and left bone of each rat, a marking was etched into the bottom of the sample holder (Figure 56), and the right leg bones were always situated above the marking, which would be seen in the reconstructed image and allow the identification of the bones belonging to the right leg vs. the

left. Additionally, the proximal end of the tibia and distal end of the femur were aligned on the same side to be on the bottom of the sample holder, allowing a single ROI to be selected when scanning, and preventing the need to scan the whole bone thereby greatly reducing scan time. Finally, each pair of bones was double wrapped in gauze to prevent movement while in the CT scanner.

Figure 56: **Left** – sample holder with etched marking. **Right** – leg bones wrapped in gauze placed in the sample holder (right leg bones are on top of the marking).

To reduce scan time, a region of interest (ROI) was selected to be scanned (Figure 57) which encompassed the proximal end of the tibia and distal end of the femur. The top of the ROI corresponded to a distance of approximately 45 mm from the top of the scanner view, and the bottom corresponded to approximately 63 mm. The chosen ROI ensured that the cortical ROI, trabecular ROI, and etched marking would all be imaged and visible following reconstruction. The total scan time per scan averaged about 1 hour and output an average of 1300 slices after reconstruction.

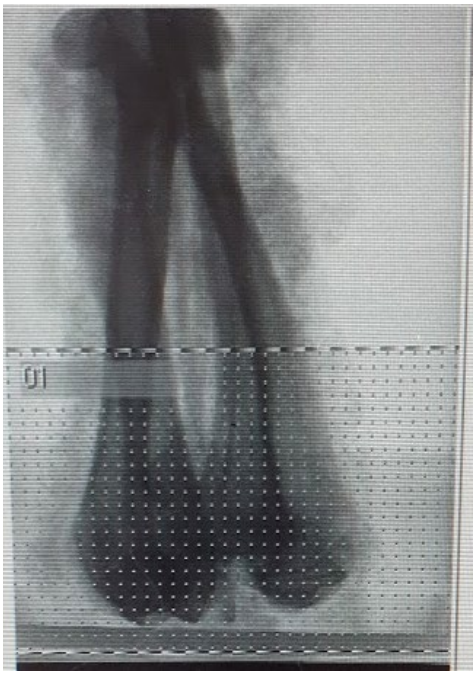

Figure 57: CT scanner view of the sample with an ROI selected that encompasses the sample holder etch, trabecular ROI, and cortical ROI.

## 8.3 IMAGE RECONSTRUCTION & PRE-PROCESSING

### 8.3.1 Reconstruction

After the CT scanning was completed, the images were reconstructed using the NRecon (Bruker-microCT, Belgium) software. Specifically, the GPUReconServer was used, which significantly cuts down reconstruction time when compared to traditional CPU-based reconstruction (reduces 1 hour and 20 minutes of reconstruction to about 5 minutes). The GPUReconServer requires a compatible NVIDIA graphics card for use. The output of the reconstruction was approximately 1300 slices of bitmap (.bmp) bone slices showing the underlying architecture of the trabecular and cortical bone, converted from the TIFF shadow

image format (.tif) output by the CT scanner. An example of the output of the scanner and reconstruction can be seen in Figure 58.

Figure 58: **Left** – single output image from the CT scanner. **Right** – reconstruction output image from NRecon

### 8.3.1 Cropping

After image reconstruction, the ImageJ software platform (v1.52e, (Schneider et al. 2012)) was used to crop individual bones (right tibia, right femur, left tibia, left femur) to allow for more simple segmentation and data handling for bone morphometric analysis. The rectangle tool was used to outline the image segment corresponding to a particular bone, and then the "Image -> Crop" function was used to perform the cropping. The cropping reduced the total pixel dimensions that were required to be analyzed from 2000 x 2000 pixel down to an average of 650 x 650 pixels.

### 8.3.3 Orientation Alignment

To ensure that the bone morphometric analysis is performed accurately, the cropped images were normalized to ensure that all bones were aligned along a defined axis. Alignment was carried out using the ITK-SNAP (Yushkevich et al. 2006), a software application used to segment structures in 3D medical images. Since ITK-SNAP only imports medical imaging filetypes such as DICOM, and NIFTI, the bitmap image sequence of each set of bone slices were converted to the NIFTI filetype using ImageJ. To enable the conversion, a version of ImageJ called FIJI (Schindelin et al. 2012) was used, which allowed the imported bitmap image sequences of each bone to be saved as the NIFTI-1 filetype. The NIFTI file was then imported in ITK-SNAP using "File -> Open Main Image…". The image was then opened again using "File -> Add Another Image…". The reorientation was then carried out by using the "Tools -> Registration …" function using Manual Registration as seen in Figure 59. The images on the right of each panel in Figure 59 could be rotated and translated to ensure each bone was straight in all orientations. Figure 60 shows a left femur before alignment, and Figure 61 shows the same left femur after alignment. Finally, the image set was saved as a NIFTI file and imported into FIJI.

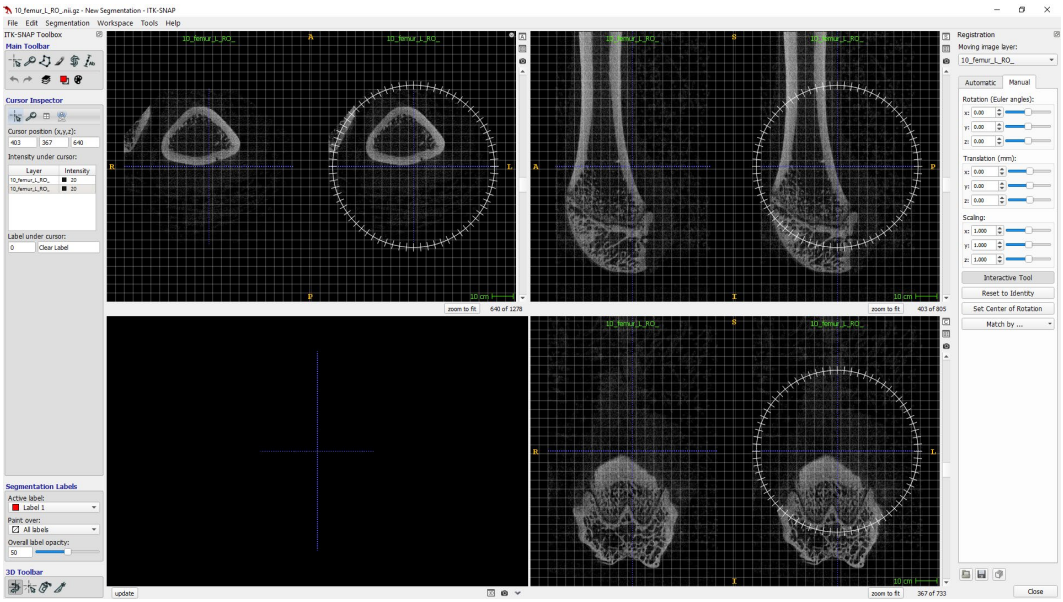

Figure 59: Registration in ITK-SNAP, allowing rotation and translation of images

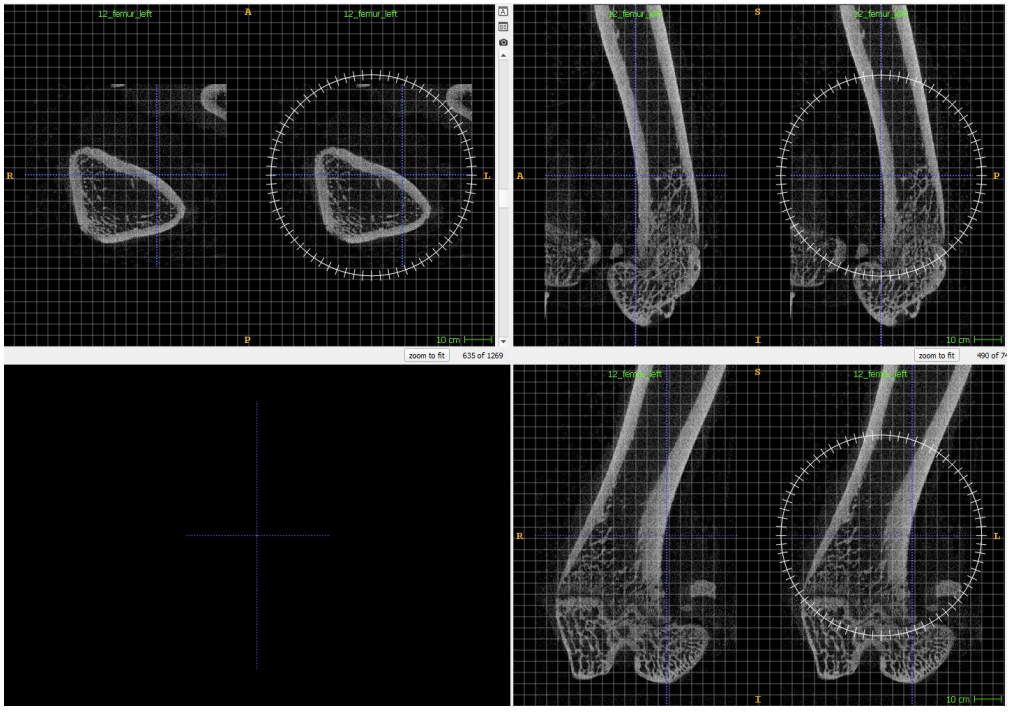

Figure 60: ITK-SNAP import of the left femur of an OVX rat before realignment

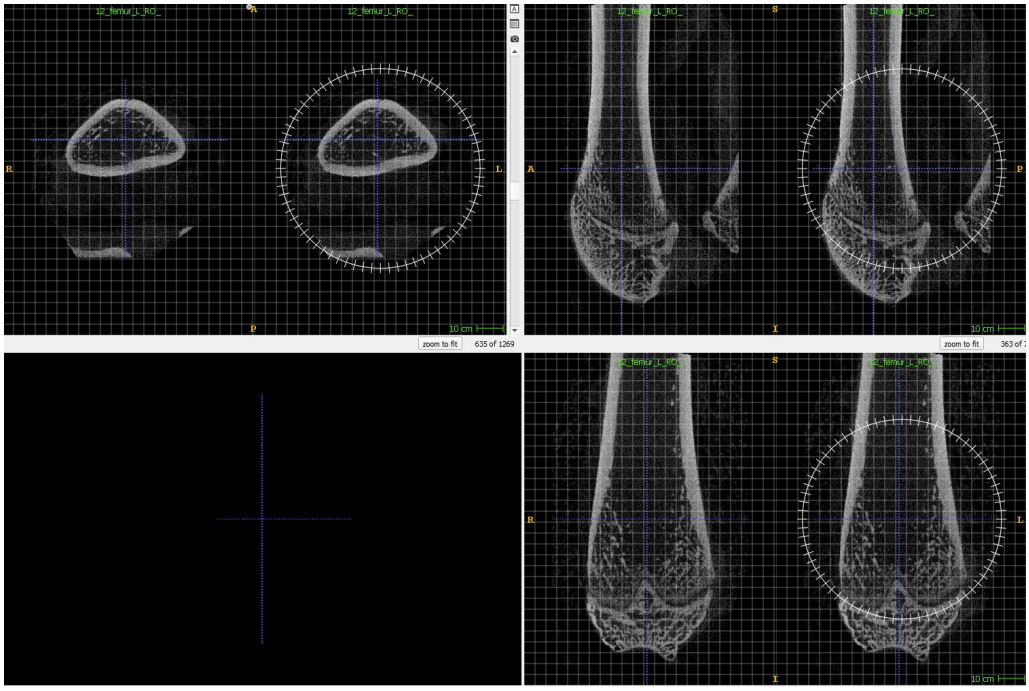

Figure 61: ITK-SNAP import of the left femur of an OVX rat after realignment

### 8.3.4 Filtering

As seen in Figure 62, the process of converting the bitmap image sequence to NIFTI, realigning the image set, saving it as a NIFTI, and then importing back into FIJI, introduced a lot of noise into the image and increases the pixel intensity.

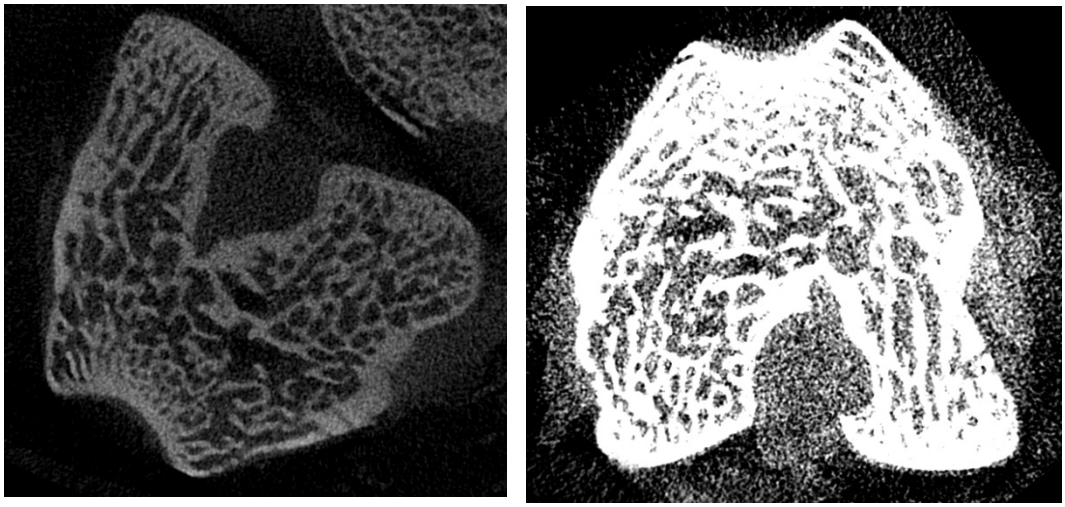

Figure 62: **Left** – left femur before alignment. **Right** – left femur after alignment

To reduce the noise and pixel intensity, a Linear Kuwahara Filter was applied to the image using "Process -> Filters -> Linear Kuwahara", with 80 angles, a line length of 11, and using variance as the criteria. This filter enables adaptive noise reduction while also preserving edges (Bakker et al. 1999), and speeds up filtering by using linear (straight) kernels instead of the rectangular kernels used by the original Kuwahara filter. Figure 63 shows the same slices of resultant images before and after the Linear Kuwahara filter is applied.

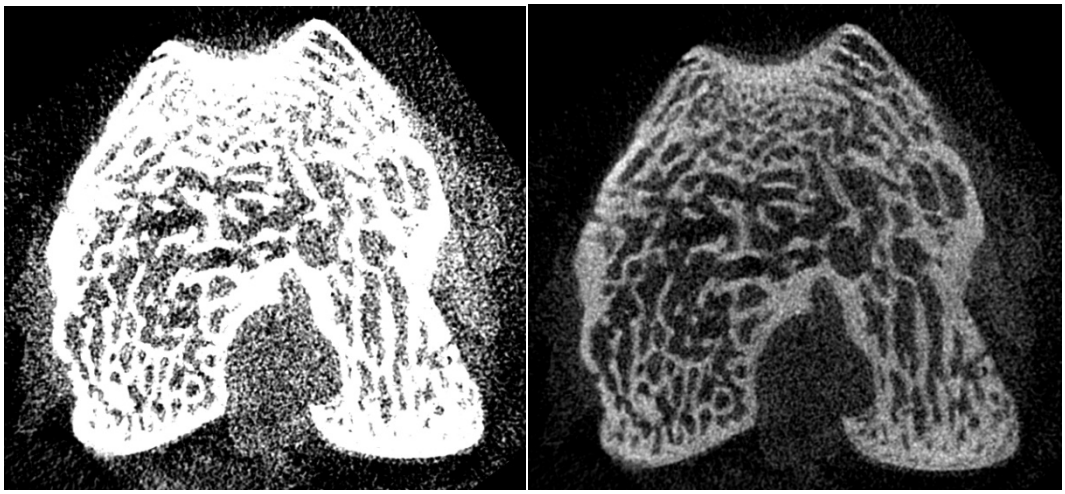

Figure 63: **Left** – left femur before filtering. **Right** – left femur after filtering

## 8.4 IMAGE ANALYSIS

### 8.4.1 Trabecular Bone

Trabecular analysis of the images was carried out using the CTAn software (Bruker-microCT, Belgium). The ROI selected for both the proximal tibia and distal femur was 3.01 mm from the growth plate (Figure 64), which was also used by Yang et al. (Yang et al. 2017) when assessing the effects of bone-targeting parathyroid hormone (PTH) conjugates on bone microstructure. This distance corresponded to a total of 232 slices, as our scanning resulted in a slice thickness of 13.1 $\mu$m.

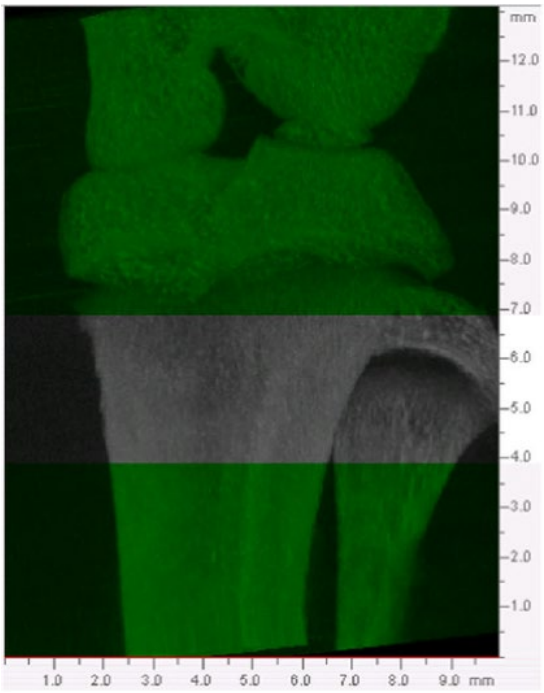


Figure 64: Micro-CT analysis region of the proximal right tibia, with a highlighted region (gray shading) showing the trabecular ROI (Yang et al. 2017)

Once the images were loaded into CTAn, the slices corresponding to the growth plate were identified visually by scrolling through the slices. Figure 65 (I – V) shows the succession of slices through the right tibia of a SHAM rat, showing the progression of the images from the end of the proximal tibia. This enables the growth plate to be identified, and allows the identification of the first slice where the growth plate has disappeared to begin the ROI selection (Figure 65 - V). Hence, in this case the ROI would consist of slices 550 up to 782. Finally, slice 550 was set to be the bottom of the stack, while 782 is set to be the top of the stack.

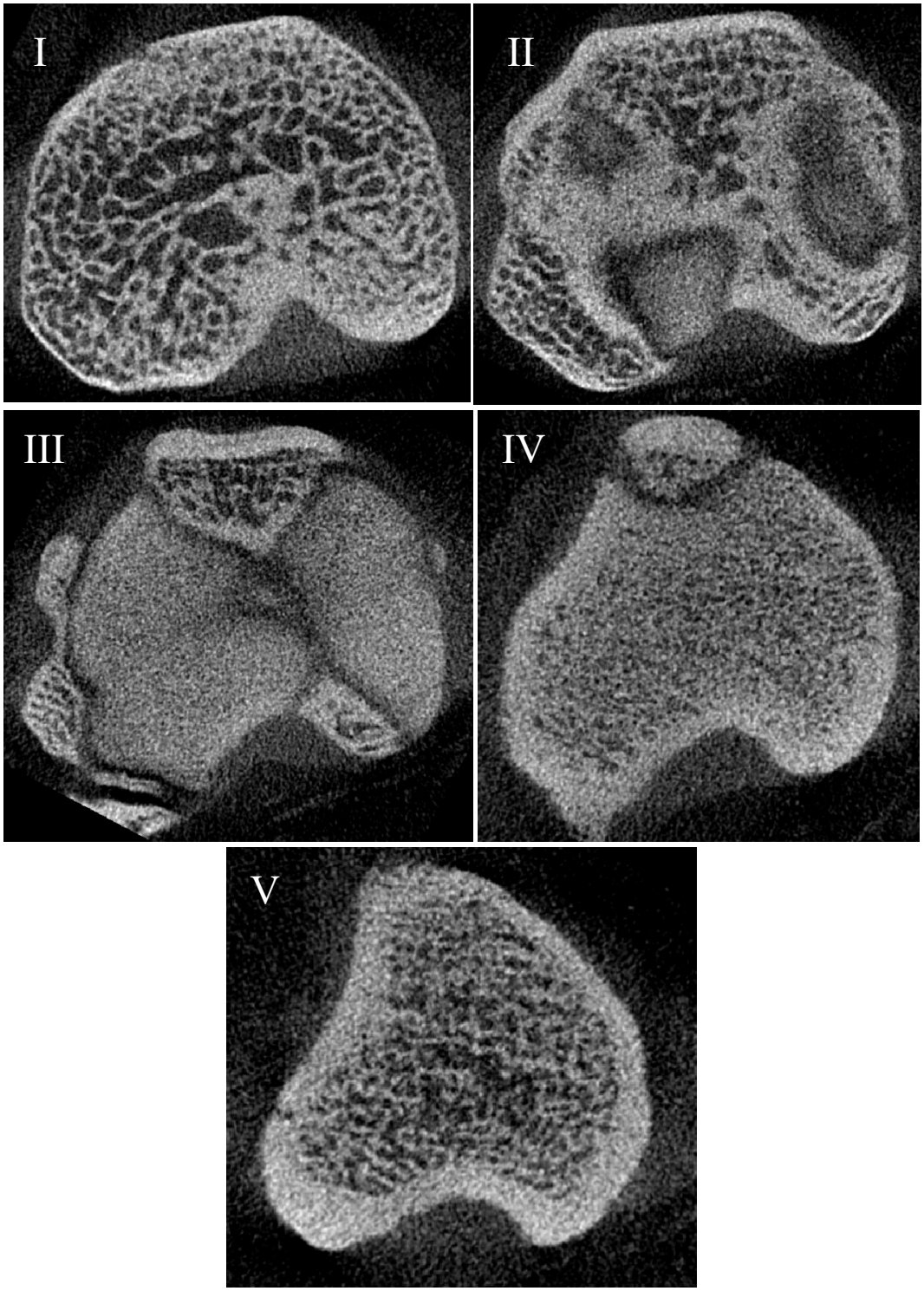


Figure 65: Slices through a left tibia showing growth plate progression. **I** – slice 300. **II** – slice 340. **III** – slice 375. **IV** - slice 445. **V** - slice 550

After the ROI was identified the region of interest was manually drawn on 4 slices along the ROI, corresponding to a drawing every 58 slices. Figure 66 shows the trabecular ROI selected for a slice of the left femur. By default, each slice in the ROI is an “interpolated” region of interest. When drawing a region on a slice, the ROI turns to “polygonal”. This allows CTAn to automatically interpolate the ROI between all the slices chosen as the ROI stack after a region has been drawn on a slice.

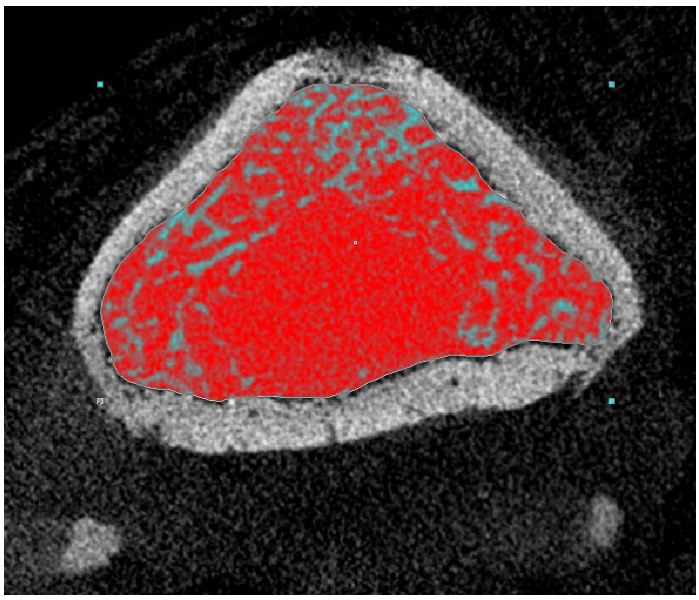

Figure 66: ROI drawn manually in CTAn

Next, a global binary threshold is set by viewing the slices as a “Binary Selection”. As shown in Figure 67, the histogram of grayscale intensities within the ROI is displayed in CTAn with a slider corresponding to the minimum chosen grayscale value, and maximum chosen value. For the majority of bones, a minimum grayscale value of 100 was chosen and a maximum of 255. For some bones that

were cropped with an existing white number from the CT reconstruction (Figure 68), a minimum grayscale value of 60 was chosen.

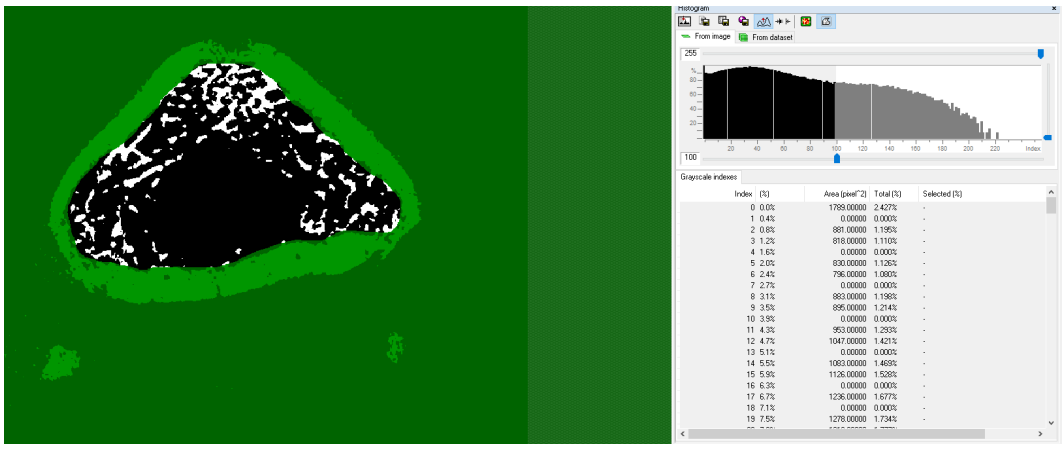

Figure 67: Binary Selection in CTAn

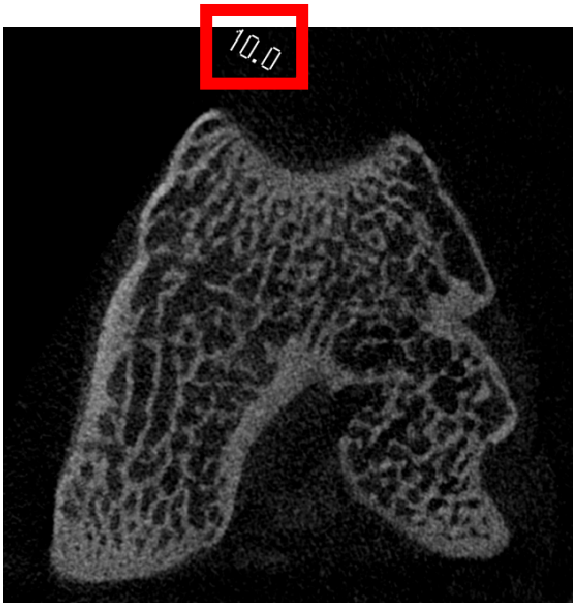


Figure 68: Cropped image with an existing white number (outlined in red) after reconstruction

Finally, "Morphometry" was used in CTAn to show the amount of trabecular bone detected by the software in the ROI (Figure 69), and to perform a

3D analysis of the trabecular bone to output the following values of highest interest: Tissue Volume (TV), Bone Volume (BV), Bone Volume Fraction (BV/TV), Trabecular Thickness (Tb.Th), Trabecular Number (Tb.N), and Degree of Anisotropy (DA). Table 8 provides a summary of the physiological relevance of each of the chosen parameters, adapted from Bouxsein et al. (Bouxsein et al. 2010). The results from the analysis of each bone were saved as a "single text line" and appended to a single .csv file, which resulted in the analysis of every bone being in a single output file with a corresponding filename and timestamp, allowing simple identification of which line of results corresponded to which bone.

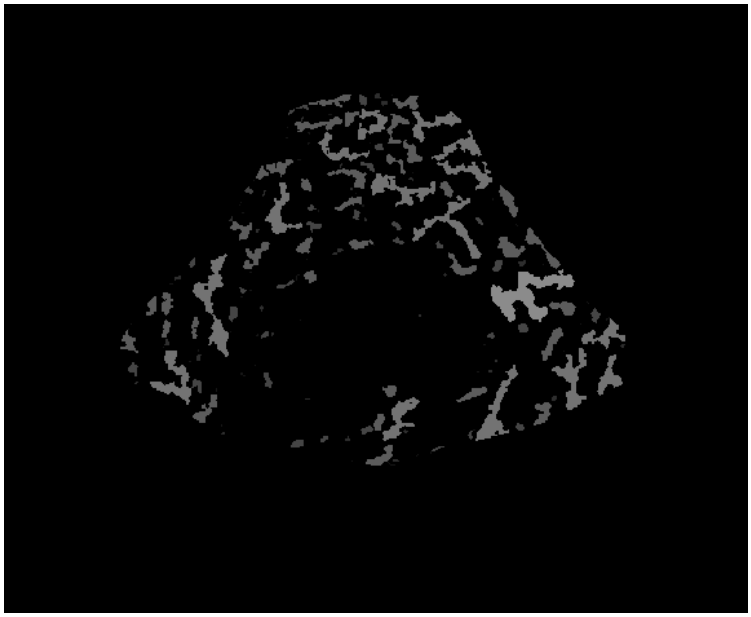

Figure 69: Visualization of trabecular bone detected in an image within the ROI

| Parameter | Abbreviation | Units | Description |
|---|---|---|---|
| Tissue Volume | TV | $mm^3$ | Volume of the entire region of interest |
| Bone Volume | BV | $mm^3$ | Volume of the region segmented as bone |
| Bone Volume Fraction | BV/TV | % | Ratio of the segmented bone volume to the total volume of the region of interest |
| Trabecular Thickness | Tb.Th | mm | Mean thickness of trabeculae, assessed using direct 3D methods |
| Trabecular Number | Tb.N | 1/mm | Measure of the average number of trabeculae per unit length |
| Degree of Anisotropy | DA | - | 1 = isotropic, >1 = anisotropic; DA = length of longest divided by shortest mean intercept length vector |

Table 8: Definition and description of 3D outcomes for trabecular bone microarchitecture (Bouxsein et al. 2010)

### 8.4.2 Cortical Bone

Cortical analysis was started using CTAn once again. The "Custom Processing" option allowed for automated cortical bone segmentation of every bone, with an output consisting of a stack of binary images containing only cortical bone saved in the folder of each bone. The custom processing contains a BATch MANager (BatMan) module (Figure 70) that allows a set of functions to be sequentially applied to an image stack, and applies this set of functions to every image dataset provided. Table 9 shows a summary of the functions used for cortical segmentation in order from first to last, along with a description containing the parameters used. A detailed description of each function can be seen in the *Bruker-MicroCT method note* (Bruker Micro-CT) hosted by the University of Manitoba.

Figure 71 shows the CT image of a left femur along with the segmented cortical bone.

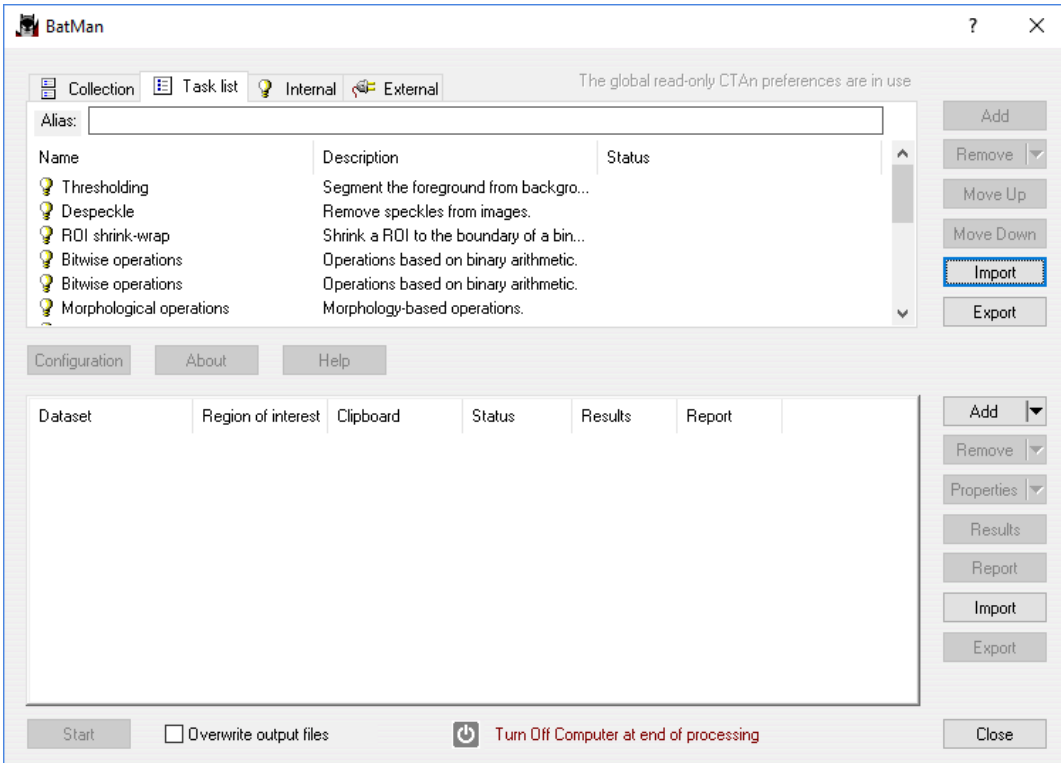


Figure 70: CTAn BATch MANager

| Function | Parameters |
|---|---|
| Thresholding | Global, Low = 100, High = 255 |
| Despeckle | Type: Sweep, 3D space; Remove: all except the largest object; Apply to: Image |
| ROI shrink-wrap | Mode: Shrink-wrap, 2D space; Stretch over holes; Diameter: 20 pixels |
| Bitwise operations | Image = NOT Image |
| Bitwise Operations | Image = Image AND Region of Interest |
| Morphological operations | Type: Opening, 2D space; Kernel: Round; Radius: 2; Apply to: Image |
| Despeckle | Type: Sweep, 3D space; Remove: all except the largest object; Apply to: Image |

| | |
|---|---|
| Morphological operations | Type: Closing, 2D space; Kernel: Round; Radius: 20; Apply to: Image |
| Morphological operations | Type: Opening, 2D space; Kernel: Round; Radius: 10; Apply to: Image |
| Morphological operations | Type: Erosion, 2D space; Kernel: Round; Radius: 3; Apply to: Image |
| Morphological operations | Type: Dilation, 2D space; Kernel: Round; Radius: 3; Apply to: Image |
| Bitwise operations | Region of Interest = Region of Interest SUB Image |
| Reload | Apply to: Image |
| Save bitmaps | Apply to: ROI; File format: BMP; Custom Subfolder; Convert to monochrome (1bit) |

Table 9: CTAn BATch MANager Functions

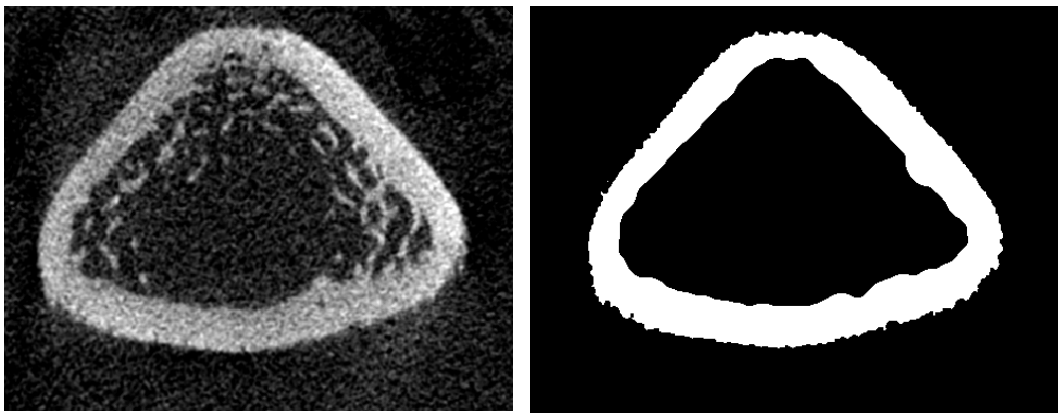

Figure 71: **Left** – CT image of a left femur. **Right** – segmented cortical image of the left femur of the same slice

Following cortical segmentation, an ImageJ plugin called BoneJ (Doube et al. 2010) was used to perform cortical analysis. The "Moments of Inertia" function was used to calculate the moments of inertia of a 60-slice (0.8 mm) thickness cortical segment at 3 locations: at the end of the growth plate (beginning of the trabecular ROI stack), at the midpoint of the trabecular ROI stack, and at a location

close to the mid-diaphysis of the bone corresponding to 37% of the length of the bone. A thickness of 0.8 mm was chosen as outlined by the *Method for ex-vivo micro-CT analysis of rat bone (proximal tibia, distal femur)* document (Bruker Micro-CT).

Assessing the cortical bone at the three chosen locations allowed for a comparison of whether the electrical stimulation had effects on cortical bone. The first location contains the cortical bone with the least thickness and highest porosity due to its proximity to the growth plate (Figure 73**)**. The second location was chosen to ensure the cortical slice has less trabecular bone but is also within a region covered by the electrode applied during experimentation (Figure 74), which was determined through placing the electrode on the bones in a manner similar to experimentation (Figure 72). The final location was chosen to ensure cortical bone close to the mid-diaphysis and also well out of bounds of the electrode region was analyzed (Figure 75). Additionally, this region was chosen to be 37% of the length of each bone to ensure that: the same relative region of cortical bone is selected across bones, the region is outside that covered by the electrode, and the region contains slices within the maximum number of slices in each stack. Table 10: Summary of ROI slices determined for rat 10 shows a sample of the slices corresponding to each region for each bone of rat 10 (OVX STIM). Each stack contained a set of blank slices that had to be subtracted from the total number of slices before determining whether or not the mid-diaphysis ROI was within the slice limit.

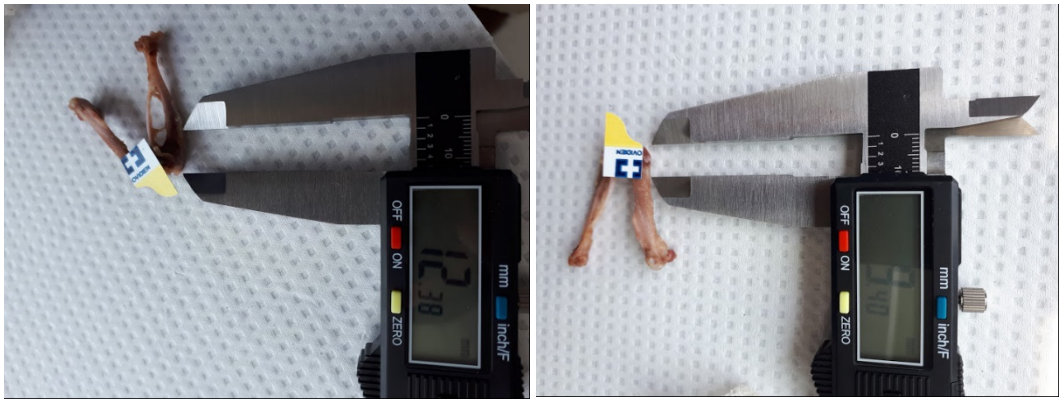


Figure 72: **Left** – Distance from the proximal tibia that the electrode covers on the tibia. **Right** – Distance from the distal femur that the electrode covers on the femur

| Bone | # of Blank Slices | Total # of slices | Total Length (mm) | Trabecular ROI Beginning | Electrode ROI Beginning | Mid-Diaphysis ROI Beginning |
|---|---|---|---|---|---|---|
| Left Femur | 84 | 1278 | 36.81 | 530 | 645 | 1039.6 |
| Right Femur | 202 | 1278 | 36.89 | 640 | 755 | 1041.9 |
| Left Tibia | 61 | 1278 | 41.75 | 450 | 565 | 1179.2 |
| Right Tibia | 260 | 1278 | 42.6 | 730 | 845 | 1203.2 |

Table 10: Summary of ROI slices determined for rat 10

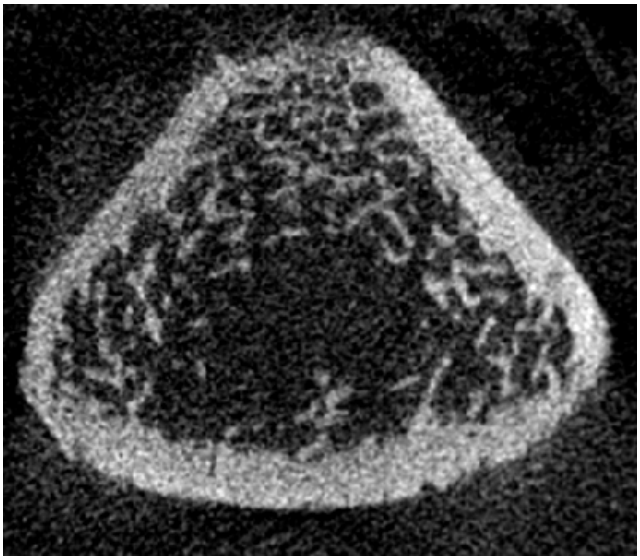

Figure 73: Left femur of rat 10, slice 530 (trabecular ROI)

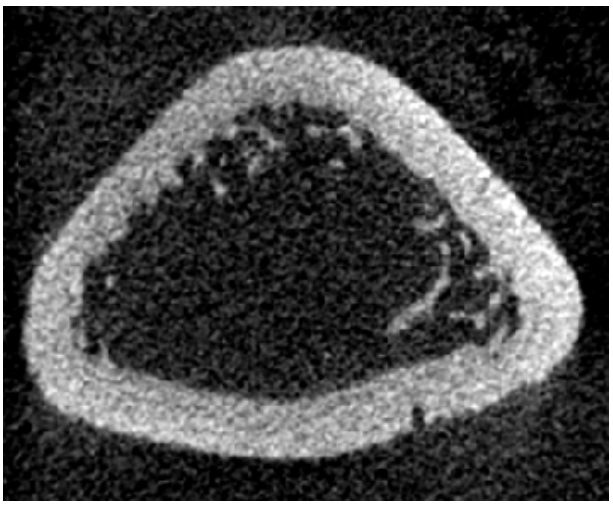

Figure 74: Left femur of rat 10, slice 645 (electrode ROI)

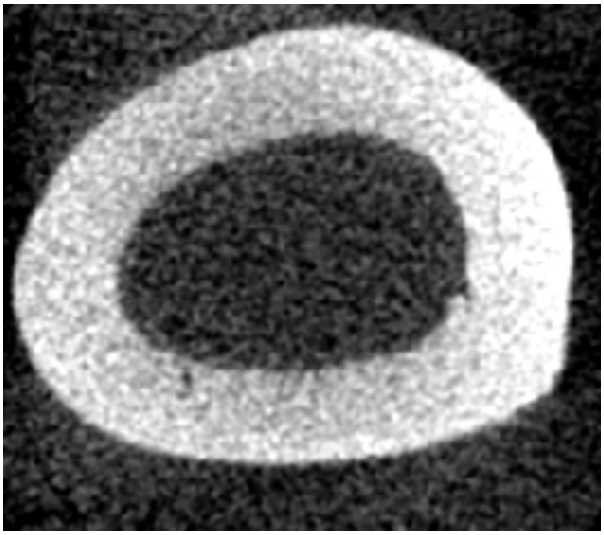

Figure 75: Left femur of rat 10, slice 1039 (mid-diaphysis ROI)

The moments of inertia for the stack of 60 slices for each of the three chosen locations was then analyzed using BoneJ. This process was semi-automated using the Macro shown in Appendix C, which automatically calculates the parameters for all 3 stacks of an opened image sequence and saves them to an excel .csv file. The start and end slices, and the filename, had to be manually entered into the macro for each bone. The collection of excel files was then combined using the command line (CMD) with the command "copy *.csv combined.csv" after changing directories to the folder containing the excel files. When performing the analysis, the calibration factor chosen was 1.8 $g/cm^3$. The output of BoneJ gave results in units of $kg*m^2$ which was converted to a more common unit of $mm^4$ by using the correction factor along with a pixel size of 1 $\mu$m. Additionally, the output provided was a sum of the moments in all the slices in the stack, so it was divided 60 (the number of slices in a stack) to provide an average value of the moments. When performing the data

analysis, any data points that were shown to be outliers were manually assessed to see if there was failure in the automation process, and the correct analysis output was then used.

# CHAPTER 9: RESULTS

## 9.1 MICRO-CT ANALYSIS (BONE ARCHITECTURE)

### 9.1.1 Trabecular Bone

The first set of results determined was the degree of bone loss experienced by the OVX group, by looking at the differences in trabecular number relative to the baseline group. A one-tailed confidence interval was used throughout all tests for a 5% significance level. As seen in Figure 76 and Figure 77, the OVX BASELINE group had a much higher trabecular number than both the OVX NOSTIM and OVX STIM groups. With the difference in every bone being statistically significant. These results are also summarized in Table 12 as a percentage decrease in trabecular number relative to the OVX BASELINE group, and clearly show a decrease of around 50% in each bone. Interestingly, there was almost a 10% decrease in the amount of bone lost in a stimulated femur compared to a non-stimulated femur. But, the difference between these femurs, shown later, were not found to be statistically significant so the difference cannot confidently be attributed to the electrical stimulation treatment.

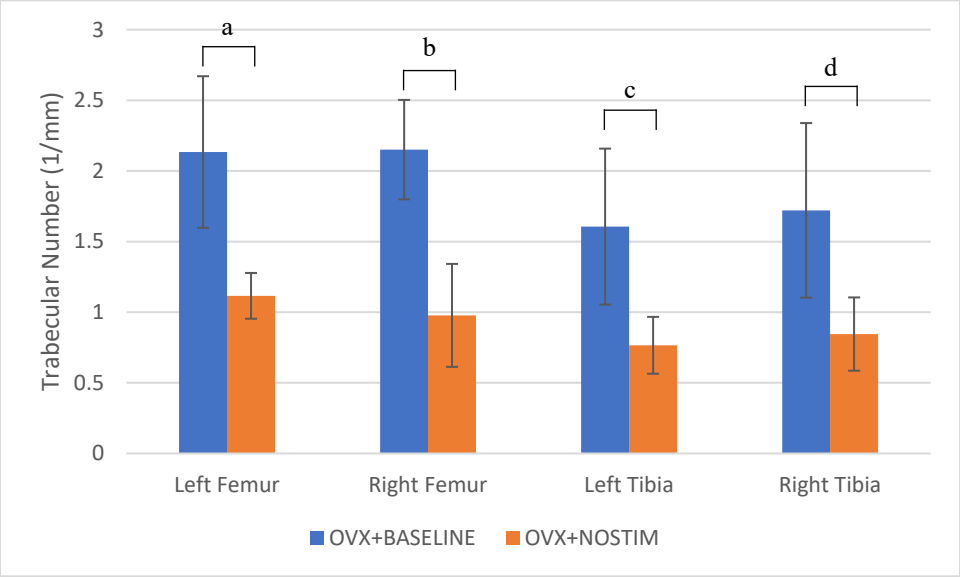


[a] $P = 0.0013$; [b] $P = 0.0012$; [c] $P = 0.0051$; [d] $P = 0.0084$

Figure 76: Comparison of trabecular number between OVX BASELINE and OVX NOSTIM. Significant bone loss experienced by the NOSTIM group due to OVX.

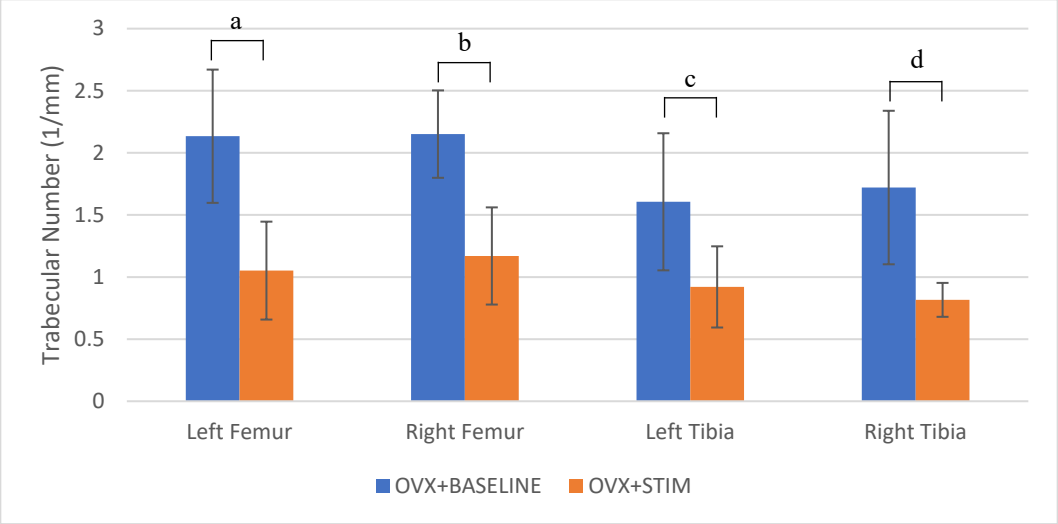


[a] $P = 0.0051$; [b] $P = 0.0041$; [c] $P = 0.0238$; [d] $P = 0.0041$

Figure 77: Comparison of trabecular number between OVX BASELINE and OVX STIM. Significant bone loss experienced by the STIM group due to OVX.

| | OVX NOSTIM | OVX STIM |
|---|---|---|
| Left Femur | 47.71% | 50.70% |
| Right Femur | 54.56% | 45.62% |
| Left Tibia | 52.31% | 42.68% |
| Right Tibia | 50.88% | 52.56% |

Table 11: Percentage decrease in trabecular number relative to OVX baseline

The next set of results determined were the comparison between the stimulated (right) set of bones to the non-stimulated (left). For this data a paired comparison was performed (t-test: paired two sample means) as it is a within-subject comparison that controls for all variation between-subjects, thus providing a stronger comparison with higher statistical confidence. Since our initial hypothesis is that the stimulated bones will have higher trabecular number and thickness than the non-stimulated bones, a one-tailed confidence interval was used throughout all tests for a 5% significance level.

The comparison between the stimulated and non-stimulated femur and tibia of the OVX STIM group can be seen in Figure 78 to Figure 81, with error bars representing the standard deviation of the data and corresponding statistical significance values below the graphs. As seen in the figures, the trabecular thickness of the stimulated femur and tibia showed a slight increase compared to the non-stimulated, with the difference between femurs (0.0788 mm to 0.0769 mm) almost being statistically significant ($P = 0.0508$). When comparing the trabecular number between femurs, the stimulated femur showed a statistically significant ($P = 0.0029$) increase compared to the non-stimulated femur (1.17 $mm^{-1}$ compared to

1.05 $mm^{-1}$), corresponding to an increase of 11.4% from the non-stimulated. The tibia did not show a significant difference in trabecular number.

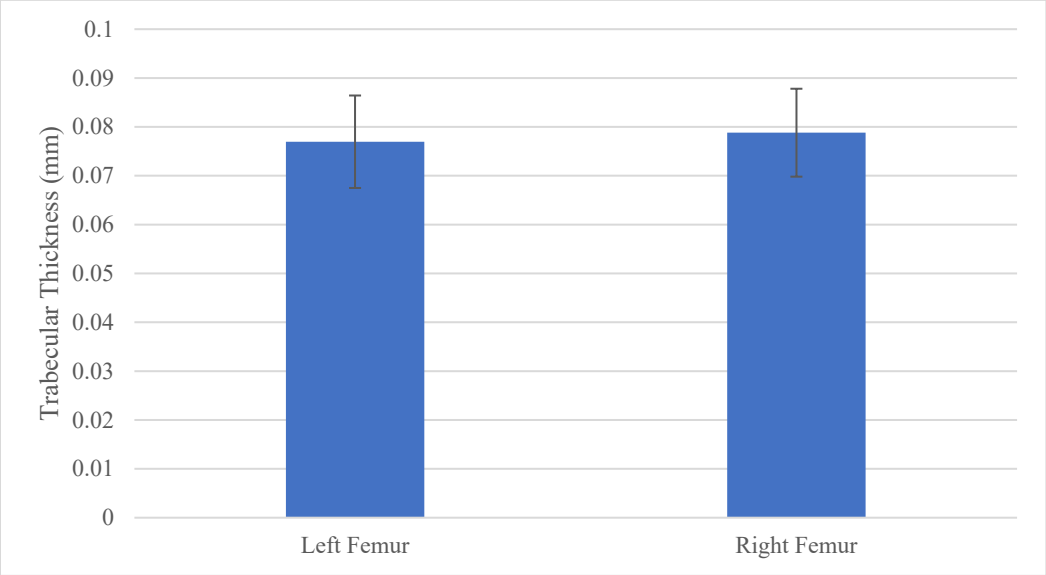


Figure 78: Trabecular thickness of OVX STIM femurs. Left Femur (non-stimulated) versus Right Femur (stimulated). $P = 0.0508$ (N.S.). Stimulated femur shows slight increase compared to unstimulated.

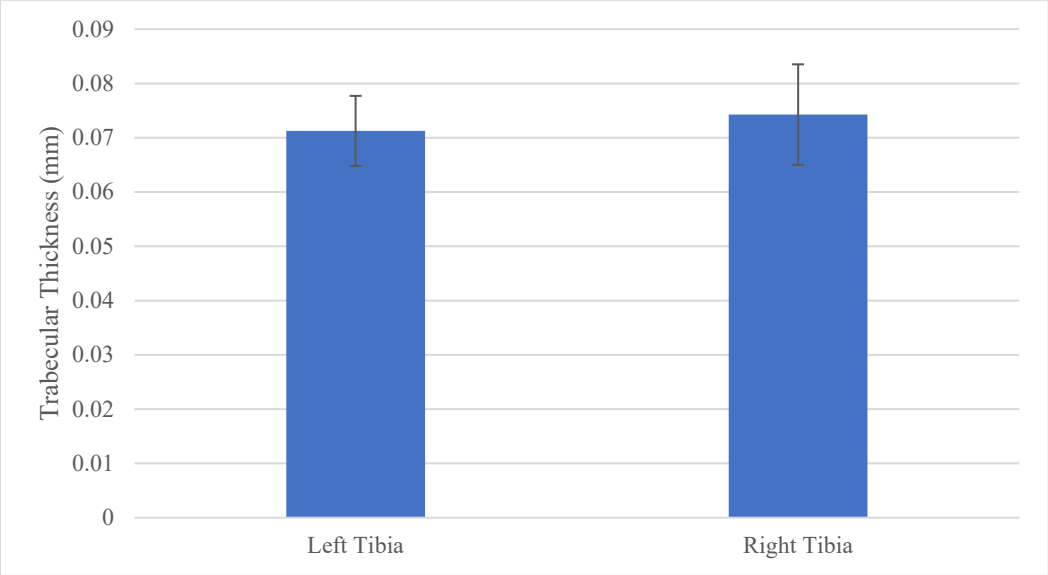


Figure 79: Comparison of trabecular thickness in OVX STIM tibia. Left Tibia (non-stimulated) versus Right Tibia (stimulated). $P = 0.2404$ (N.S.). Stimulated tibia shows slight increase compared to unstimulated.

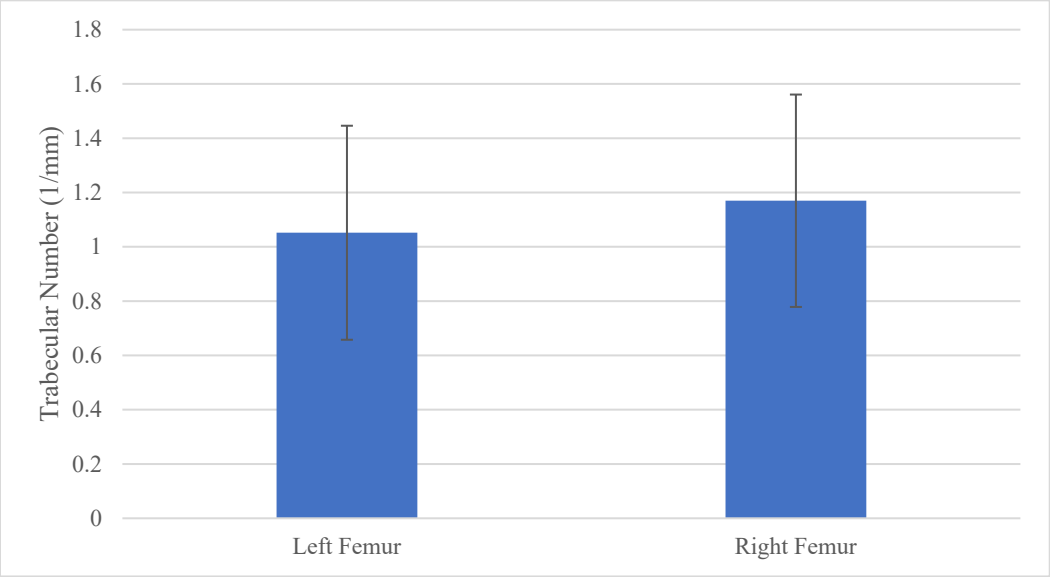


Figure 80: Comparison of trabecular number in OVX STIM femur. $P = 0.0029$. Stimulated femur showed significant increase compared to unstimulated.

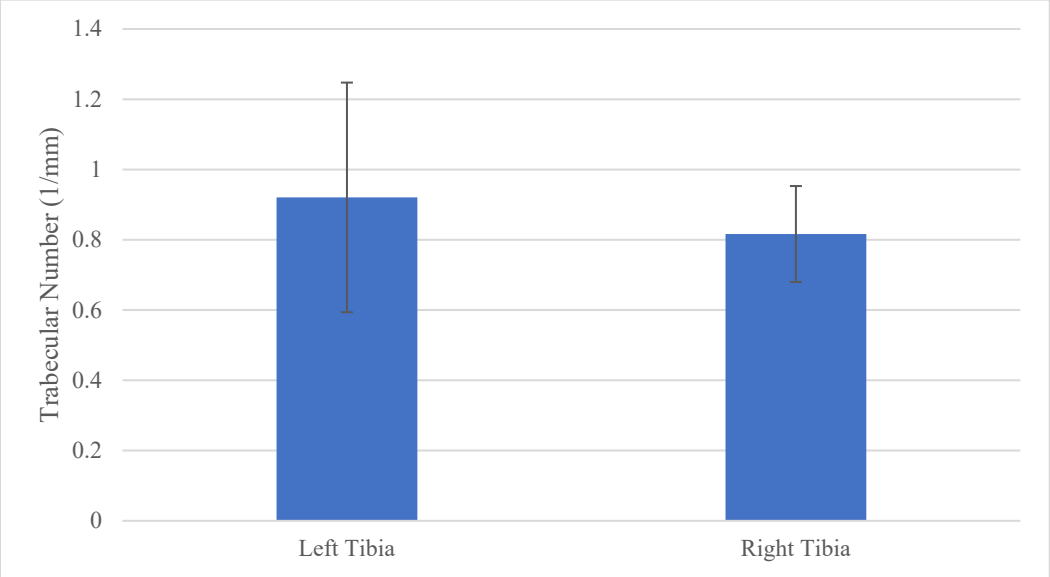


Figure 81: Comparison of trabecular number in OVX STIM tibia. $P = 0.1810$ (N.S.). Stimulated tibia showed slight decrease compared to unstimulated.

Similarly, to find out whether the electrical stimulation had an effect on trabecular bone, the trabecular parameters were compared between the OVX NOSTIM group and the OVX STIM group. Figure 82 shows a summary of the

trabecular thickness results between the two groups. The right femur was the only bone where the stimulation tended to show an increase in trabecular thickness, although this result was not significantly different. The only significant difference occurred in the comparison between the right tibia of the groups, where the non-stimulated tibia had a greater trabecular thickness than the stimulated ($p = 0.0153$), contrary to the hypothesis. Figure 83 shows similar results for the difference in trabecular number between groups. As seen in the figure, there are small differences between groups, but none of the differences were found to be statistically significant. Although there is an increase in the stimulated femur as expected, there is almost no difference between the right tibia of both groups.

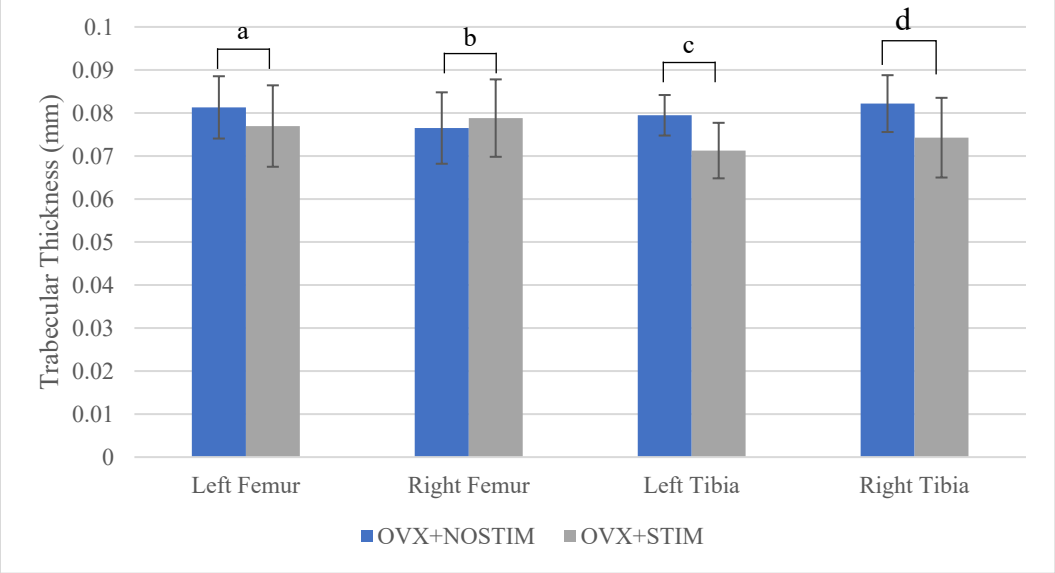


[a] $P = 0.197$ (N.S.); [b] $P = 0.480$ (N.S.); [c] $P = 0.0153$; [d] $P = 0.0595$ (N.S.)

Figure 82: Comparison of trabecular thickness between OVX NOSTIM and OVX STIM. OVX STIM stimulated femur showed slight increase over OVX NOSTIM stimulated femur.

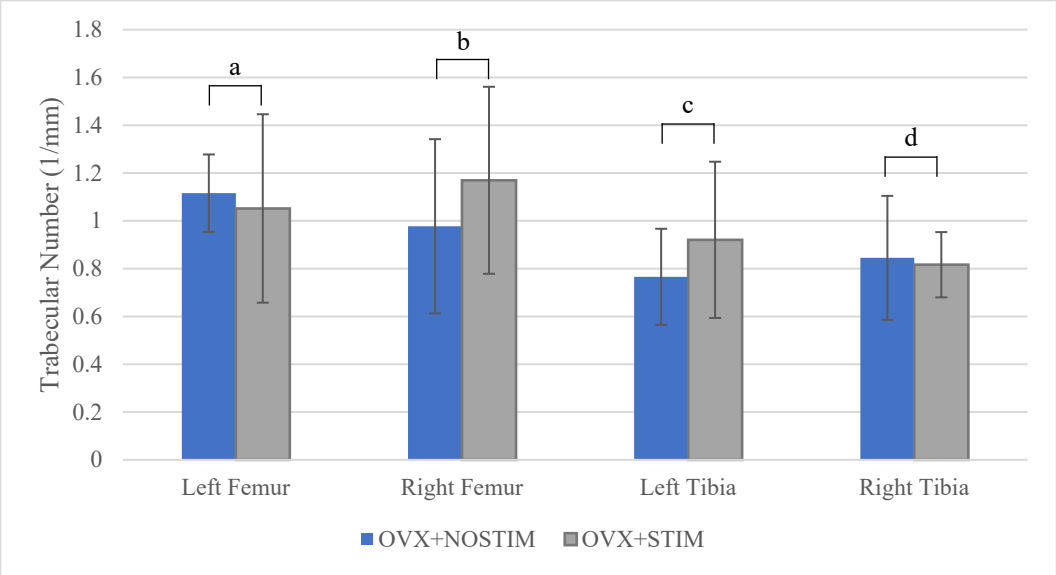


[a] $P = 0.367$ (N.S.); [b] $P = 0.199$ (N.S.); [c] $P = 0.173$ (N.S.); [d] $P = 0.407$ (N.S.)

Figure 83: Comparison of trabecular number between OVX NOSTIM and OVX STIM. No significant differences found between groups.

To see whether electrical stimulation could have effects on the bones of healthy rats, a within-subject paired comparison of the bones was also performed for the SHAM STIM group. Figure 84 to Figure 87 shows a summary of this comparison of the trabecular thickness and trabecular number. There were minimal differences between the stimulated and non-stimulated bones, and none of the differences were found to be statistically significant.

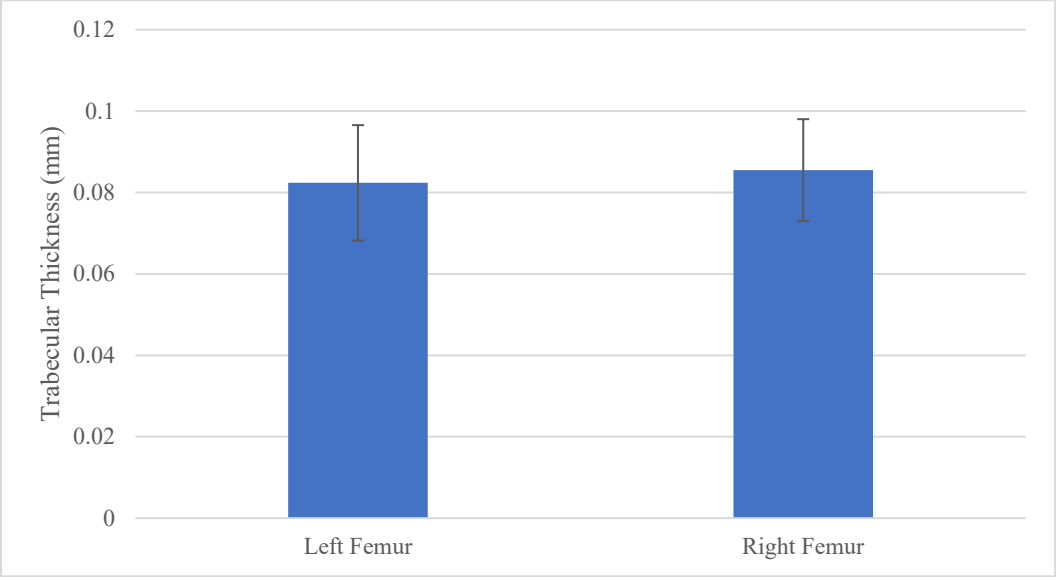


Figure 84: Comparison of trabecular thickness in SHAM STIM femur. $P = 0.265$ (N.S.). No significant difference found between stimulated and unstimulated femurs.

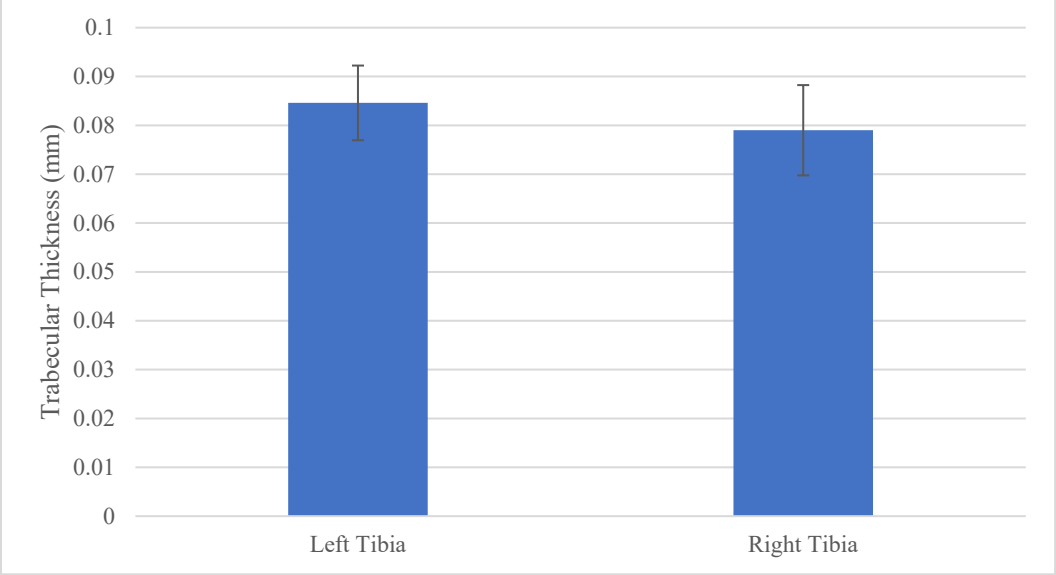


Figure 85: Comparison of trabecular thickness in SHAM STIM tibia. $P = 0.199$ (N.S.). No significant difference found between stimulated and unstimulated tibias.

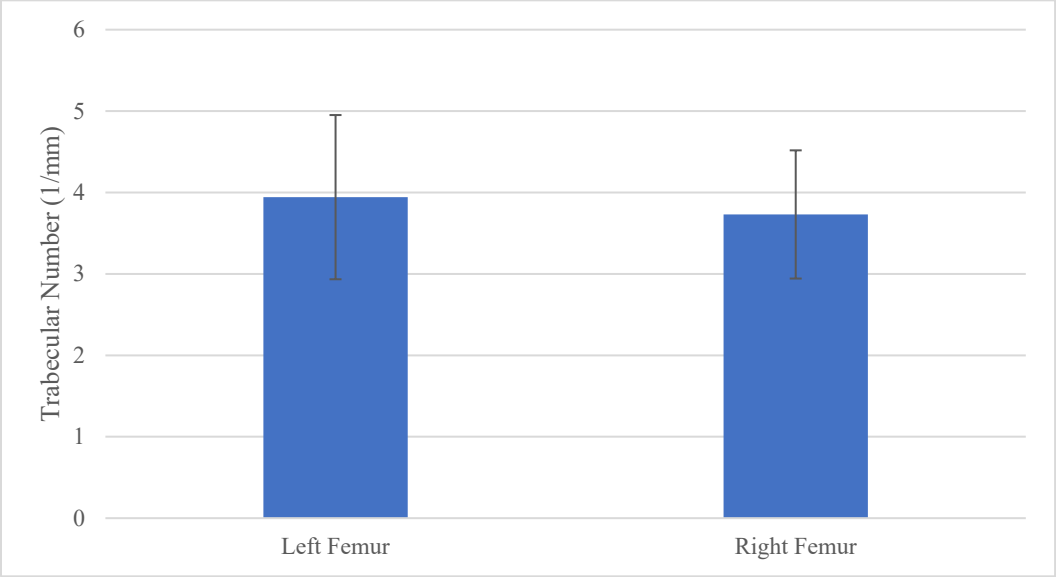


Figure 86: Comparison of trabecular number in SHAM STIM femur. $P = 0.453$ (N.S.). No significant difference found between stimulated and unstimulated femurs.

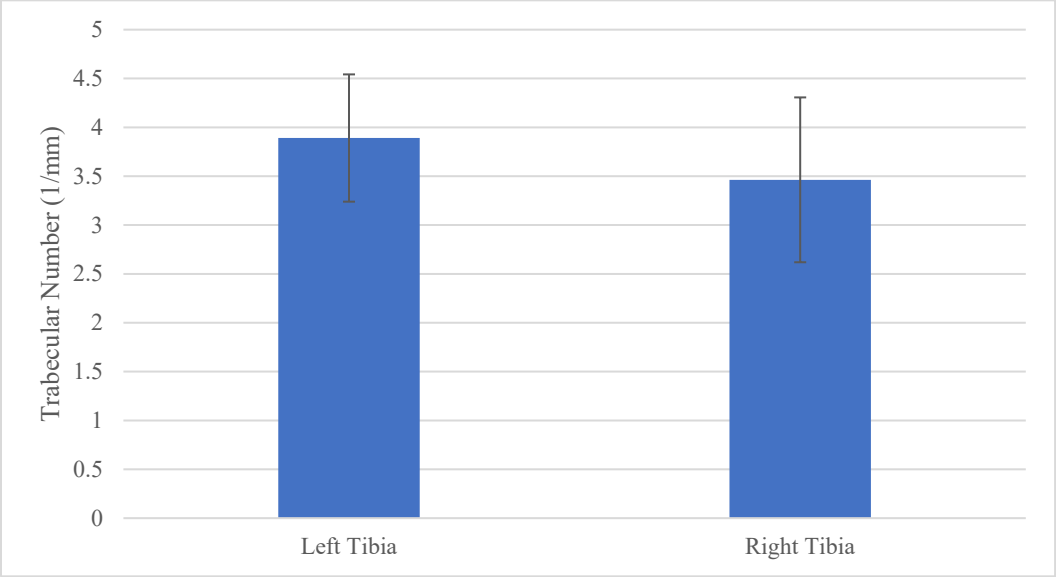


Figure 87: Comparison of trabecular number in SHAM STIM tibia. $P = 0.421$ (N.S.). No significant difference found between stimulated and unstimulated tibias.

After assessing the trabecular number and trabecular thickness, the bone volume fraction of each group was assessed to see if there were significant changes in total bone due to the electrical stimulation treatment. The results for the comparison between OVX groups can be seen in Figure 90, which shows the large decrease in total bone volume in both the OVX NOSTIM and OVX STIM groups in every bone relative to the baseline group. The figure also shows no significant results on the efficacy of the electrical stimulation on bone volume fraction, as the increase in the right femur of the stimulated group was not significantly different than that of the non-stimulated group ($P = 0.224$). The results for the comparison between SHAM groups can be seen in Figure 91, which shows the increase in bone volume in both the SHAM NOSTIM and SHAM STIM group relative to the baseline group following normal, healthy growth. Interestingly, the stimulated femur and tibia show a higher bone volume fraction than the non-stimulated, but this finding was not significant and holds true for the left bones of the SHAM STIM group as well, meaning the SHAM STIM group may just inherently have had greater bone volume than the SHAM NOSTIM group.

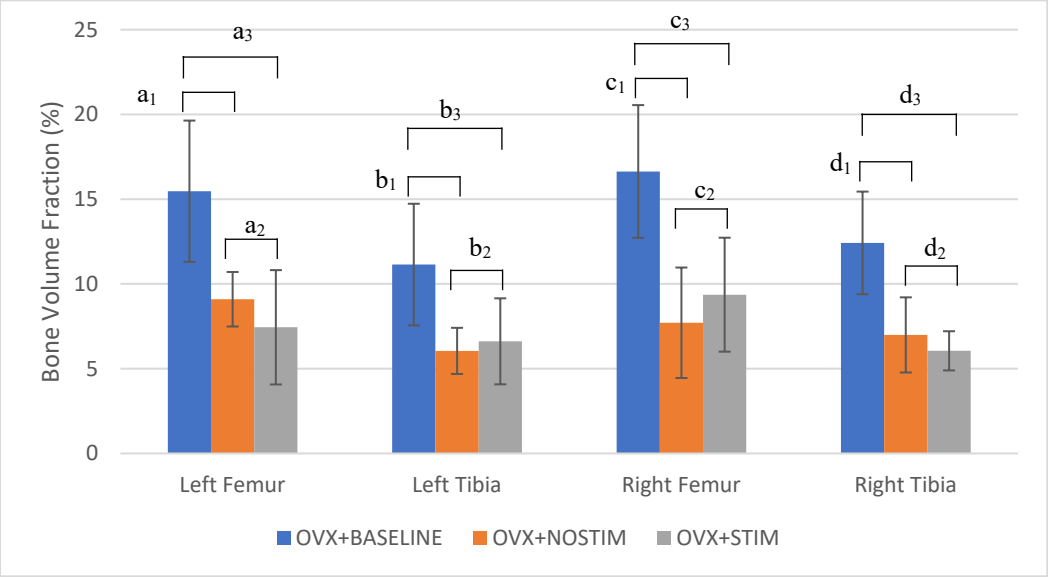


[a]1 $P = 0.012$; [a]2 $P = 0.185$ (N.S.); [a]3 $P = 0.013$
[b]1 $P = 0.015$; [b]2 $P = 0.335$ (N.S.); [b]3 $P = 0.048$
[c]1 $P = 0.008$; [c]2 $P = 0.224$ (N.S.); [c]3 $P = 0.019$
[d]1 $P = 0.023$; [d]2 $P = 0.210$ (N.S.); [d]3 $P = 0.006$

Figure 88: Comparison of bone volume fraction between OVX groups. Significant total bone loss experienced by OVX STIM and OVX NOSTIM groups due to OVX.

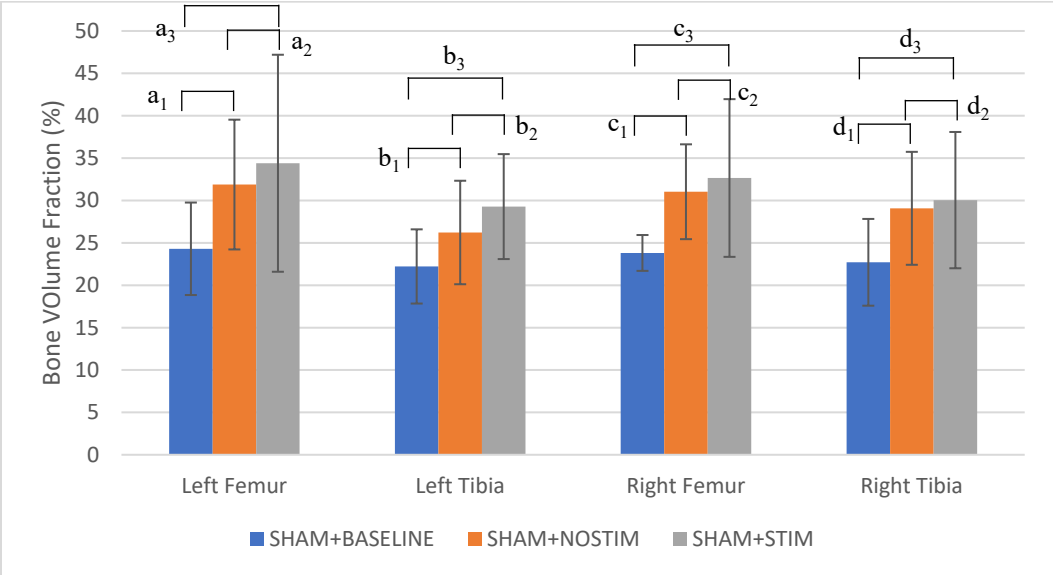


[a]1 $P = 0.109$ (N.S.); [a]2 $P = 0.357$ (N.S.); [a]3 $P = 0.143$ (N.S.)
[b]1 $P = 0.200$ (N.S.); [b]2 $P = 0.225$ (N.S.); [b]3 $P = 0.082$ (N.S.)
[c]1 $P = 0.049$; [c]2 $P = 0.372$ (N.S.); [c]3 $P = 0.097$ (N.S.)
[d]1 $P = 0.120$ (N.S.); [d]2 $P = 0.420$ (N.S.); [d]3 $P = 0.122$ (N.S.)

Figure 89: Comparison of bone volume fraction between SHAM groups. Slight increase in total bone experienced by SHAM STIM and SHAM NOSTIM groups over time.

Finally, the degree of anisotropy of each group was assessed to see if the electrical stimulation had any effects on trabecular bone orientation. The comparison between OVX groups can be seen in Figure 92, which shows very similar anisotropic behaviour between the OVX NOSTIM and OVX STIM group across all bones, with some variability when compared to baseline. Similarly, the results between SHAM groups can be seen in Figure 93. Here, there is again very little variability between the stimulated and non-stimulated group across all bones, with a small, but consistent decrease in anisotropy relative to baseline across all bones.

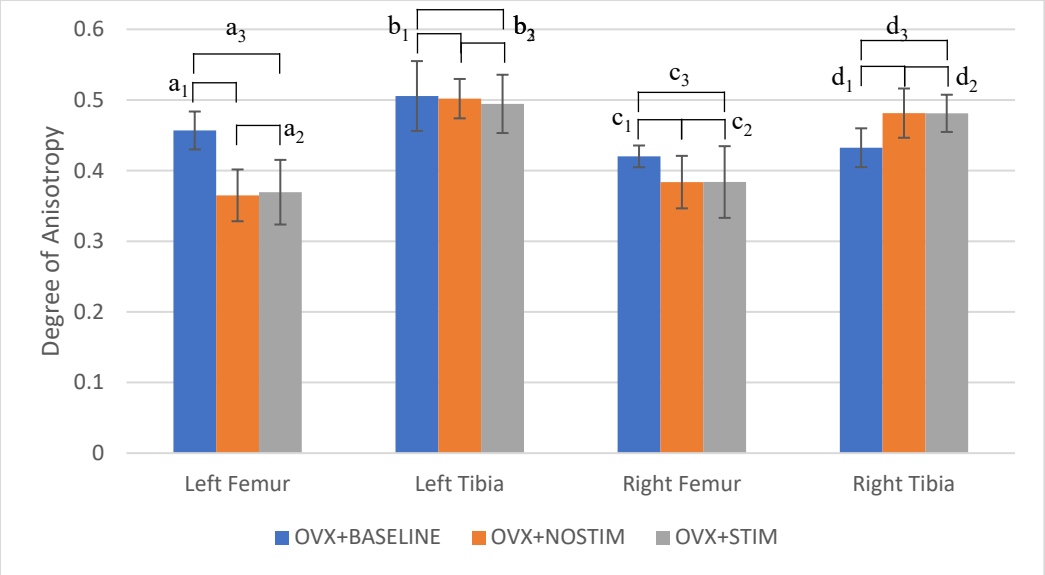


[a]1 $P = 0.006$; [a]2 $P = 0.428$ (N.S.); [a]3 $P = 0.009$
[b]1 $P = 0.451$ (N.S.); [b]2 $P = 0.356$ (N.S.); [b]3 $P = 0.368$ (N.S.)
[c]1 $P = 0.097$ (N.S.); [c]2 $P = 0.498$ (N.S.); [c]3 $P = 0.105$ (N.S.)
[d]1 $P = 0.127$ (N.S.); [d]2 $P = 0.494$ (N.S.); [d]3 $P = 0.109$ (N.S.)

Figure 90: Comparison of degree of anisotropy between OVX groups. Similar anisotropic behaviour was seen between OVX STIM and OVX NOSTIM groups.

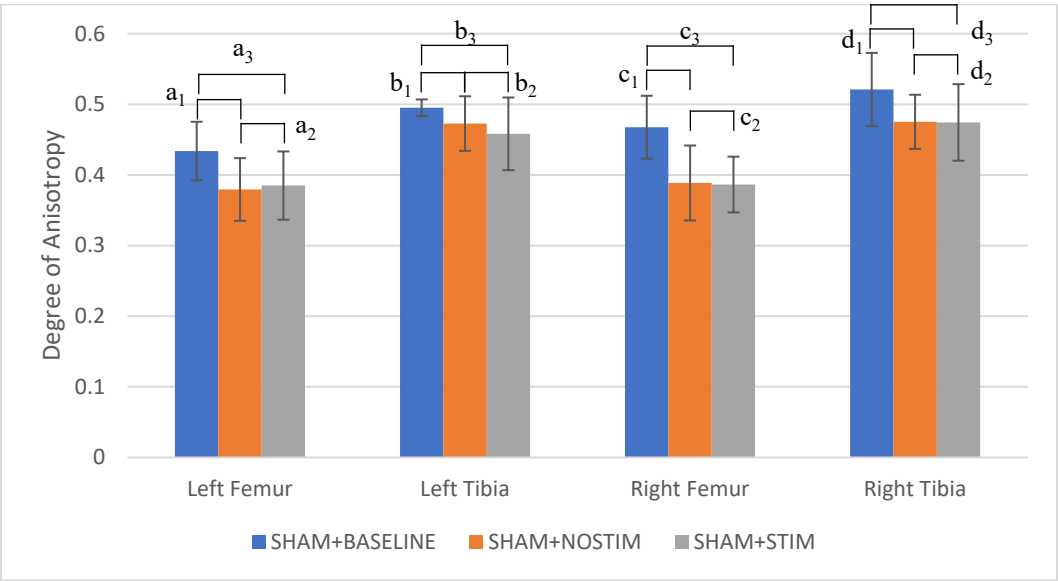


$^{a}_{1}$ $P = 0.004$; $^{a}_{2}$ $P = 0.358$ (N.S.); $^{a}_{3}$ $P = 0.021$
$^{b}_{1}$ $P = 0.191$ (N.S.); $^{b}_{2}$ $P = 0.311$ (N.S.); $^{b}_{3}$ $P = 0.166$ (N.S.)
$^{c}_{1}$ $P = 0.007$; $^{c}_{2}$ $P = 0.455$ (N.S.); $^{c}_{3}$ $P = 0.005$
$^{d}_{1}$ $P = 0.044$; $^{d}_{2}$ $P = 0.100$ (N.S.); $^{d}_{3}$ $P = 0.487$ (N.S.)

Figure 91: Comparison of degree of anisotropy between SHAM groups. Similar anisotropic behaviour was seen between SHAM STIM and SHAM NOSTIM groups.

A full summary of the trabecular analysis across all groups can be seen in Table 13, reported as the mean value across samples +/- the standard deviation across samples.

| Group | Bone | Trabecular Thickness ($\mu$m) | Trabecular Number (1/mm) | Bone Volume Fraction (%) | Degree of Anisotropy |
|---|---|---|---|---|---|
| OVX BASELINE | Left Femur | 72 +/- 10 | 2.13 +/- 0.536 | 15.5 +/- 4.17 | 0.457 +/- 0.0268 |
| OVX NOSTIM | Left Femur | 81 +/- 7 | 1.12 +/- 0.162 | 9.1 +/- 1.61 | 0.365 +/- 0.0367 |
| OVX STIM | Left Femur | 77 +/- 9 | 1.05 +/- 0.394 | 7.44 +/- 3.37 | 0.369 +/- 0.0458 |
| SHAM BASELINE | Left Femur | 76 +/- 7 | 3.15 +/- 0.643 | 24.3 +/- 5.46 | 0.434 +/- 0.0414 |
| SHAM NOSTIM | Left Femur | 87 +/- 10 | 3.63 +/- 0.619 | 31.9 +/- 7.65 | 0.379 +/- 0.0443 |
| SHAM STIM | Left Femur | 82 +/- 14 | 3.94 +/- 1.01 | 34.4 +/- 12.8 | 0.385 +/- 0.0483 |
| OVX BASELINE | Left Tibia | 68 +/- 6 | 1.61 +/- 0.552 | 16.6 +/- 3.92 | 0.42 +/- 0.0154 |
| OVX NOSTIM | Left Tibia | 80 +/- 5 | 0.766 +/- 0.201 | 7.71 +/- 3.26 | 0.384 +/- 0.0372 |
| OVX STIM | Left Tibia | 71 +/- 6 | 0.921 +/- 0.327 | 9.37 +/- 3.36 | 0.384 +/- 0.0508 |
| SHAM BASELINE | Left Tibia | 72 +/- 8 | 2.71 +/- 0.44 | 23.8 +/- 2.11 | 0.468 +/- 0.0445 |
| SHAM NOSTIM | Left Tibia | 76 +/- 7 | 3.45 +/- 0.731 | 31 +/- 5.59 | 0.389 +/- 0.053 |
| SHAM STIM | Left Tibia | 85 +/- 8 | 3.89 +/- 0.651 | 32.7 +/- 9.3 | 0.386 +/- 0.0395 |
| OVX BASELINE | Right Femur | 76 +/- 14 | 2.15 +/- 0.352 | 11.1 +/- 3.59 | 0.506 +/- 0.0494 |

| Group | Bone | Trabecular Thickness ($\mu$m) | Trabecular Number (1/mm) | Bone Volume Fraction (%) | Degree of Anisotropy |
|---|---|---|---|---|---|
| OVX NOSTIM | Right Femur | 77 +/- 8 | 0.977 +/- 0.364 | 6.05 +/- 1.36 | 0.502 +/- 0.0279 |
| OVX STIM | Right Femur | 79 +/- 9 | 1.17 +/- 0.391 | 6.61 +/- 2.54 | 0.494 +/- 0.0413 |
| SHAM BASELINE | Right Femur | 79 +/- 2 | 3.02 +/- 0.372 | 22.2 +/- 4.38 | 0.495 +/- 0.0118 |
| SHAM NOSTIM | Right Femur | 85 +/- 4 | 3.66 +/- 0.611 | 26.2 +/- 6.11 | 0.473 +/- 0.0386 |
| SHAM STIM | Right Femur | 86 +/- 13 | 3.73 +/- 0.787 | 29.3 +/- 6.19 | 0.458 +/- 0.0514 |
| | | | | | |
| OVX BASELINE | Right Tibia | 72 +/- 2 | 1.72 +/- 0.618 | 12.4 +/- 3.03 | 0.432 +/- 0.0274 |
| OVX NOSTIM | Right Tibia | 82 +/- 7 | 0.845 +/- 0.259 | 6.99 +/- 2.22 | 0.481 +/- 0.0349 |
| OVX STIM | Right Tibia | 74 +/- 9 | 0.816 +/- 0.137 | 6.06 +/- 1.16 | 0.481 +/- 0.0264 |
| SHAM BASELINE | Right Tibia | 76 +/- 4 | 2.98 +/- 0.735 | 22.7 +/- 5.12 | 0.521 +/- 0.0518 |
| SHAM NOSTIM | Right Tibia | 79 +/- 5 | 3.64 +/- 0.802 | 29.1 +/- 6.66 | 0.475 +/- 0.0383 |
| SHAM STIM | Right Tibia | 79 +/- 9 | 3.46 +/- 0.844 | 30 +/- 8.04 | 0.474 +/- 0.0542 |

Table 12: Summary of trabecular analysis

### 9.1.2 Cortical Bone

Cortical bone analysis was carried out by assessing the strength of the bone along the two principal axes in 2 dimensions, by looking at the smallest and largest second moment of areas around the centroid of the bone.

To see if the electrical stimulation had effects on cortical bone properties along the principal axis with the largest moment in the OVX group, an internal paired comparison was once again performed between the stimulated (right) and non-stimulated (left) leg bones. The results of this analysis can be seen in Figure 94 and Figure 95. As seen in Figure 94 the femur showed a general trend of increase in the maximal moment in all 3 of the analyzed regions. None of the comparisons showed statistical significance but the difference between the electrode regions was almost significant ($P = 0.052$). The differences in tibia as seen in Figure 95 showed the opposite effects, with the non-stimulated tibia exhibiting a higher maximal moment than the stimulated, except for around the mid-diaphysis region where they were almost equal. None of these comparisons showed statistical significance.

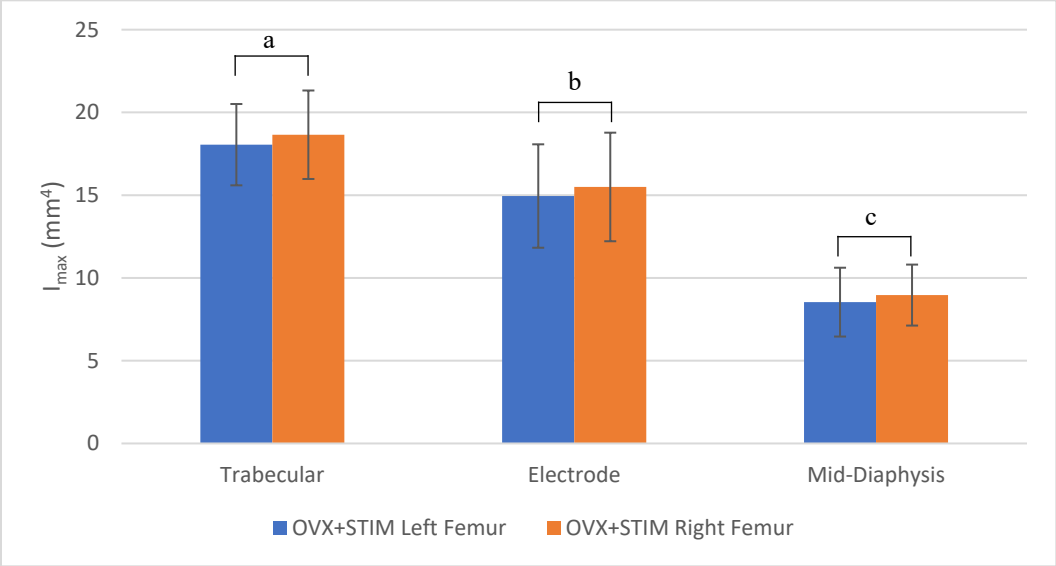


[a] $P = 0.185$ (N.S.); [b] $P = 0.098$ (N.S.); [c] $P = 0.052$ (N.S.)

Figure 92: Comparison of $I_{max}$ in OVX STIM femur. Stimulated femur showed slight increase compared to unstimulated.

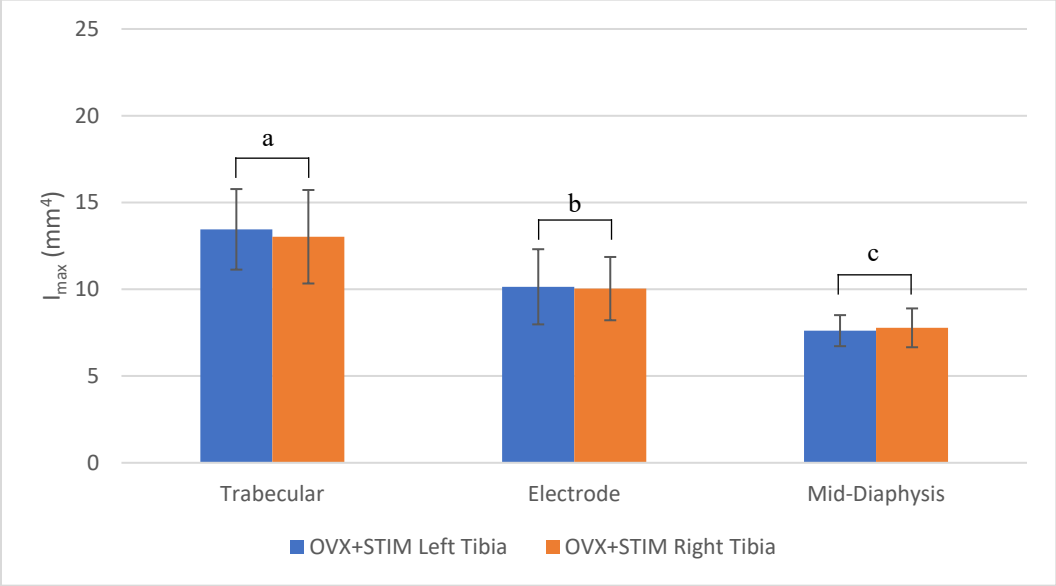


[a] $P = 0.295$ (N.S.); [b] $P = 0.160$ (N.S.); [c] $P = 0.291$ (N.S.)

Figure 93: Comparison of $I_{max}$ in OVX STIM tibia. No significant differences seen between stimulated and unstimulated tibia.

The same paired analysis was performed to see if electrical stimulation had any effects on bone cross-sectional properties of healthy rats, by comparing the

bones of the SHAM STIM group. These figures show the general trend that the maximal moment was equivalent across compared bones in all 3 regions examined. None of the comparisons showed statistical significance except for the comparison between tibia in the mid-diaphysis region ($P = 0.024$).

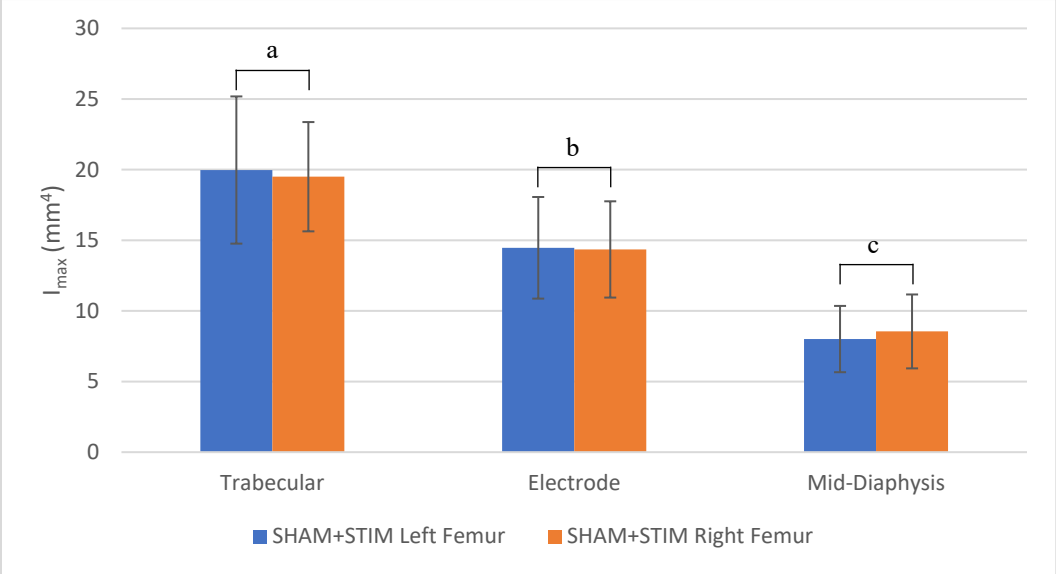


[a] $P = 0.289$ (N.S.); [b] $P = 0.423$ (N.S.); [c] $P = 0.079$ (N.S.)

Figure 94: Comparison of $I_{max}$ in SHAM STIM femur. Maximal moment was found to be approximately equivalent in all 3 regions.

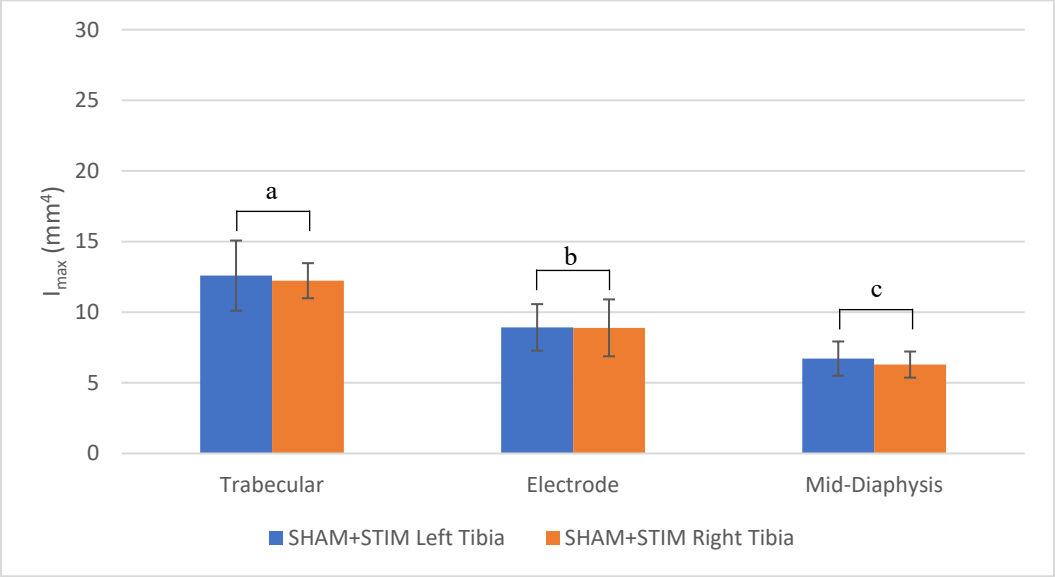


[a] $P = 0.134$ (N.S.); [b] $P = 0.457$ (N.S.); [c] $P = 0.024$

Figure 95: Comparison of $I_{max}$ in SHAM STIM tibia. Maximal moment was found to be approximately equivalent in all three regions.

Next, a comparison between the bones and regions of the OVX STIM and OVX NOSTIM groups was performed, the results of which can be seen in Figure 98 to Figure 100. None of the comparisons showed any significant results, but showed results consistent with that found during the trabecular analysis – namely that the two groups are almost equivalent except the OVX NOSTIM group shows slightly greater maximum second moment of area of the bone cross-section.

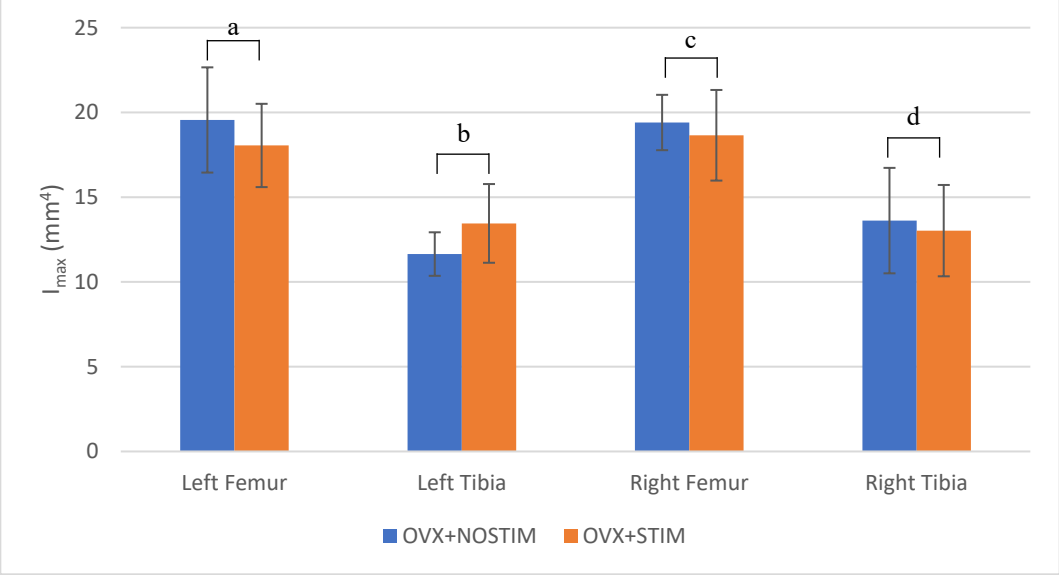


[a] $P = 0.187$ (N.S.); [b] $P = 0.063$ (N.S.); [c] $P = 0.284$ (N.S.); [d] $P = 0.366$ (N.S.)

Figure 96: Comparison of $I_{max}$ between the trabecular region of the OVX STIM and OVX NOSTIM group. No significant differences found between groups.

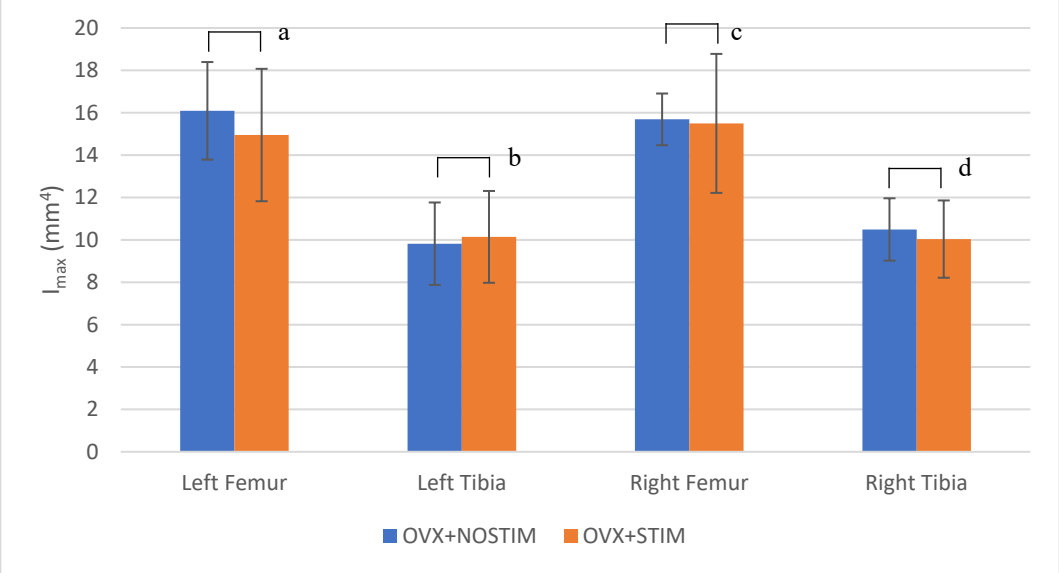


[a] $P = 0.244$ (N.S.); [b] $P = 0.165$ (N.S.); [c] $P = 0.448$ (N.S.); [d] $P = 0.322$ (N.S.)

Figure 97: Comparison of $I_{max}$ between the electrode region of the OVX STIM and OVX NOSTIM group. No significant differences found between groups.

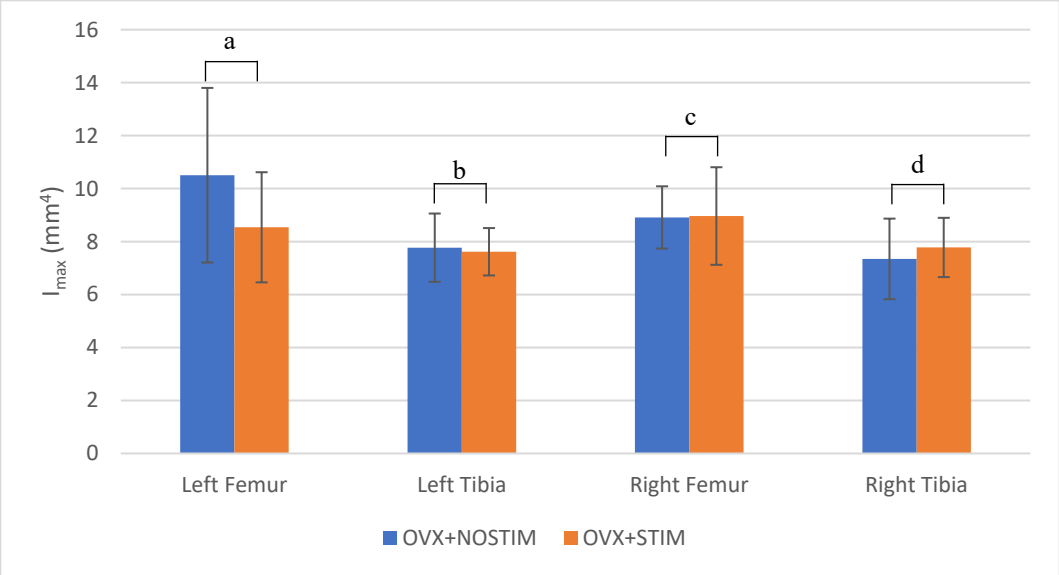


[a] $P = 0.122$ (N.S.); [b] $P = 0.408$ (N.S.); [c] $P = 0.477$ (N.S.); [d] $P = 0.294$ (N.S.)

Figure 98: Comparison of $I_{max}$ between the mid-diaphysis region of the OVX STIM and OVX NOSTIM group. No significant differences found between groups.

Similar analysis was also performed on the minimal second moment of area of the bone ($I_{min}$), to assess the bone cross-sectional properties orthogonal to the maximal moment (i.e., minimal second moment of area). As seen in Figure 101, the OVX STIM group showed a slightly higher minimal moment than the OVX NOSTIM in the trabecular region when assessing the femurs, with the difference here almost being statistically significant ($P = 0.063$). Similar to the results found in $I_{max}$, Figure 102 shows the minimal moment in the tibia, which shows that the non-stimulated tibia has a higher moment than the stimulated in all three regions, although none of these results were found to be statistically significant.

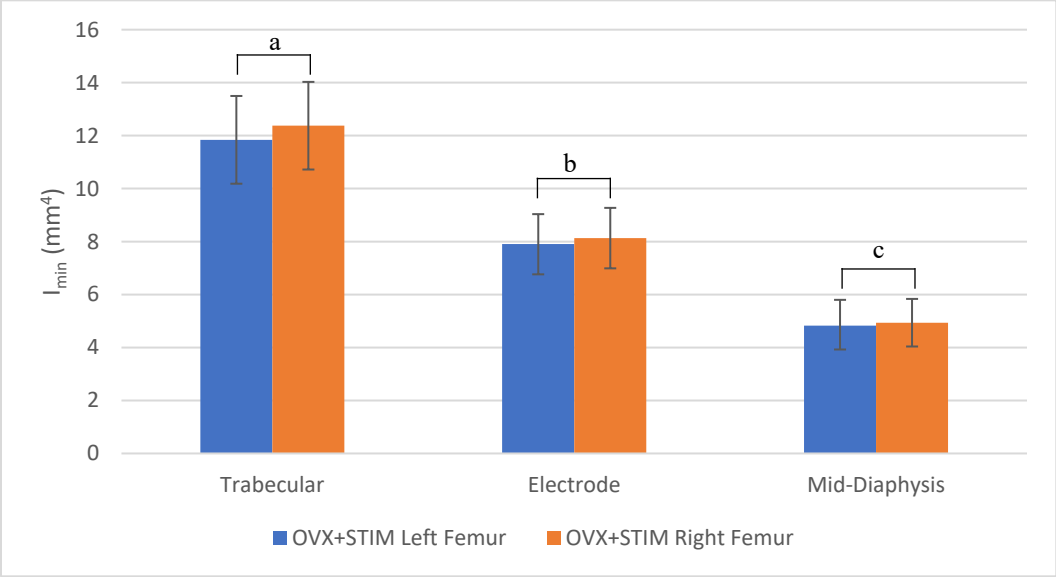


[a] $P = 0.063$ (N.S.); [b] $P = 0.169$ (N.S.); [c] $P = 0.193$ (N.S.)

Figure 99: Comparison of $I_{min}$ in OVX STIM femur. Stimulated femur shows slightly high $I_{min}$ compared to unstimulated, across all three regions.

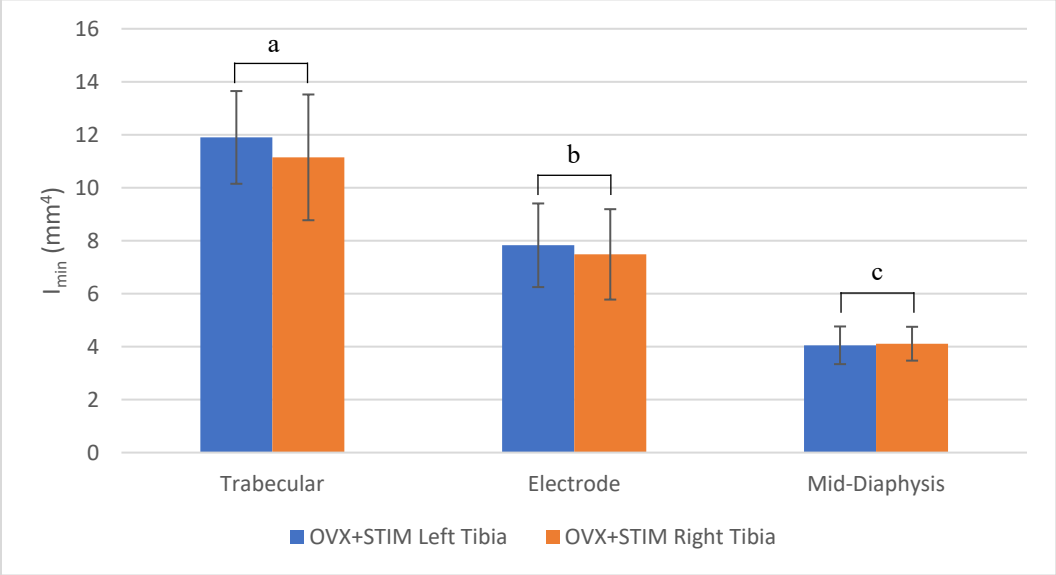


[a] $P = 0.088$ (N.S.); [b] $P = 0.132$ (N.S.); [c] $P = 0.302$ (N.S.)

Figure 100: Comparison of $I_{min}$ in OVX STIM tibia. Stimulated tibia shows slightly high $I_{min}$ compared to unstimulated, across all three regions except the mid-diaphysis.

When looking at the differences between bones in the SHAM STIM group, the internal comparison showed that both non-stimulated and stimulated sides were very similar, with no differences found to be statistically significant.

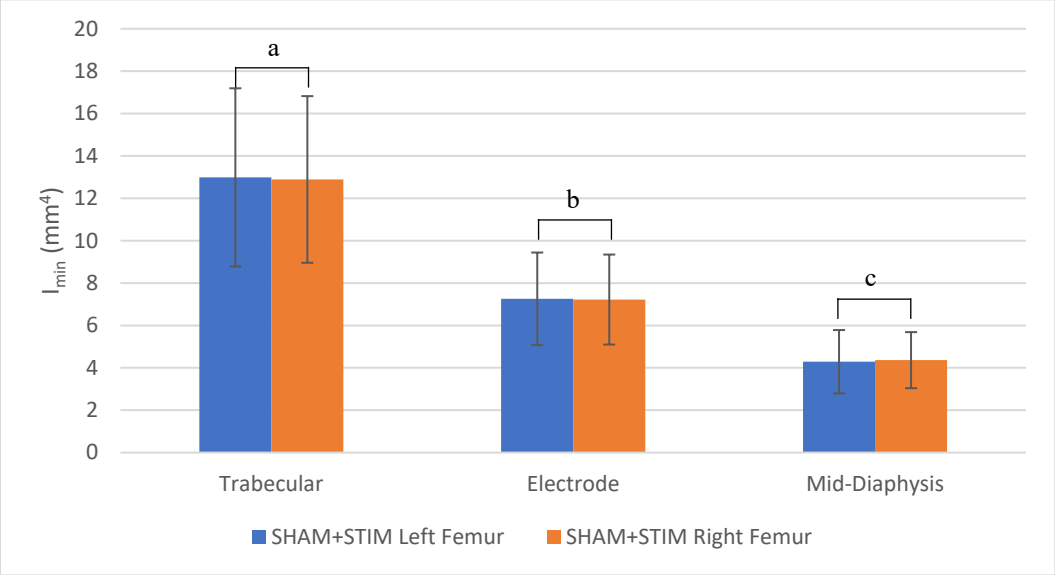


[a] $P = 0.457$ (N.S.); [b] $P = 0.468$ (N.S.); [c] $P = 0.367$ (N.S.)

Figure 101: Comparison of $I_{min}$ in SHAM STIM femur. No difference found between femurs, across all three regions.

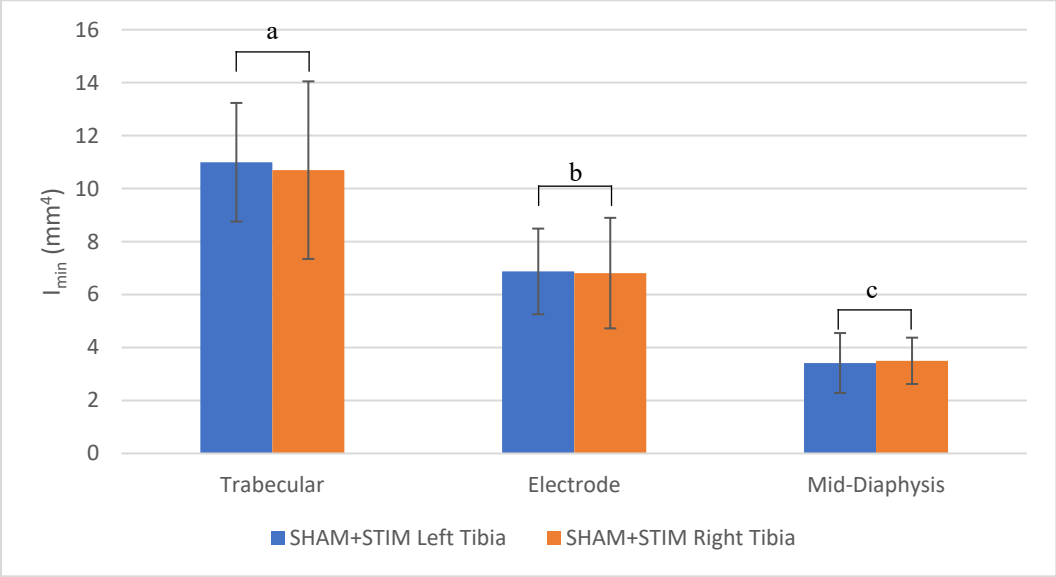


[a] $P = 0.304$ (N.S.); [b] $P = 0.416$ (N.S.); [c] $P = 0.336$ (N.S.)

Figure 102: Comparison of $I_{min}$ in SHAM STIM tibia. No difference found between tibias, across all three regions.

The assessment of $I_{min}$ between the OVX stim and OVX NOSTIM groups once again showed no significant results in the comparisons performed, and no insight into the effects of electrical stimulation on bone strength. The comparison between left tibia in the trabecular region (Figure 105) was the only result that showed a statistically significant difference, but this bone was not stimulated so nothing can be concluded with regards to the electrical stimulation treatment. The remaining comparisons can be seen below in Figure 106 and Figure 107.

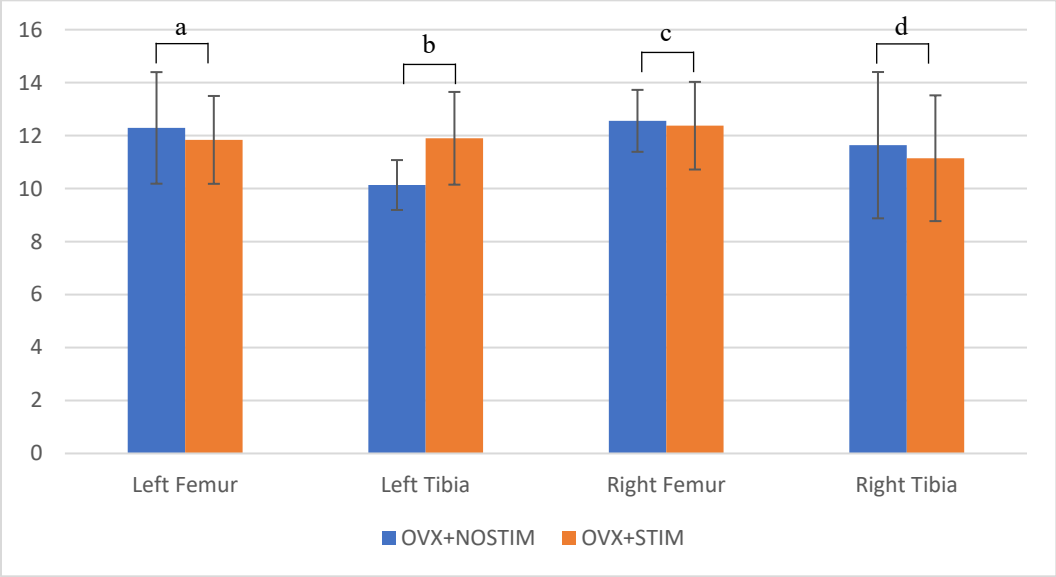


[a] $P = 0.344$ (N.S.); [b] $P = 0.027$; [c] $P = 0.414$ (N.S.); [d] $P = 0.373$ (N.S.)

Figure 103: Comparison of $I_{max}$ between the trabecular region of the OVX STIM and OVX NOSTIM group. No difference found between OVX NOSTIM and OVX STIM bones.

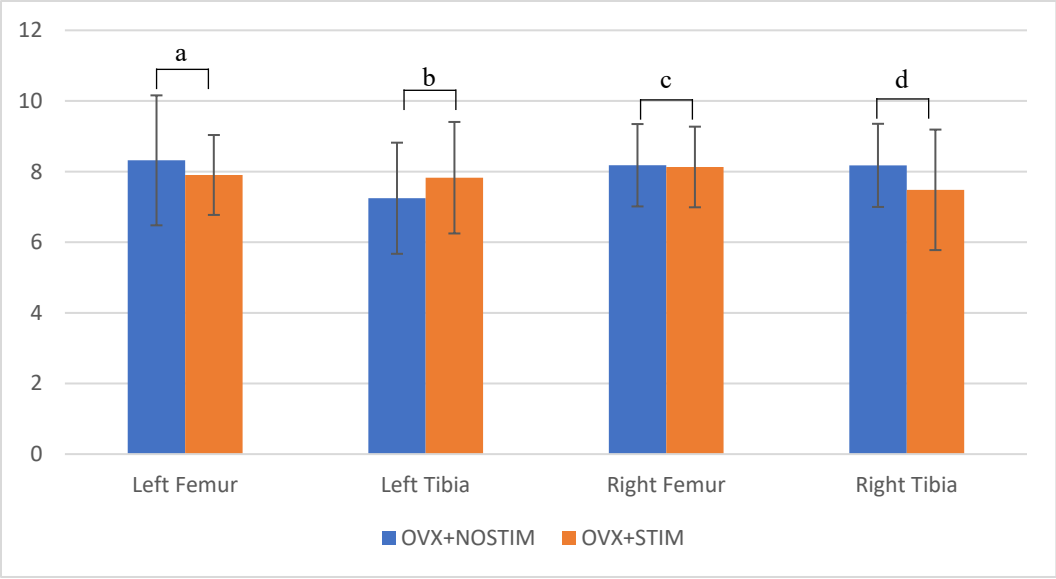


[a] $P = 0.324$ (N.S.); [b] $P = 0.130$ (N.S.); [c] $P = 0.471$ (N.S.); [d] $P = 0.216$ (N.S.)

Figure 104: Comparison of $I_{max}$ between the electrode region of the OVX STIM and OVX NOSTIM group. No difference found between OVX NOSTIM and OVX STIM bones.

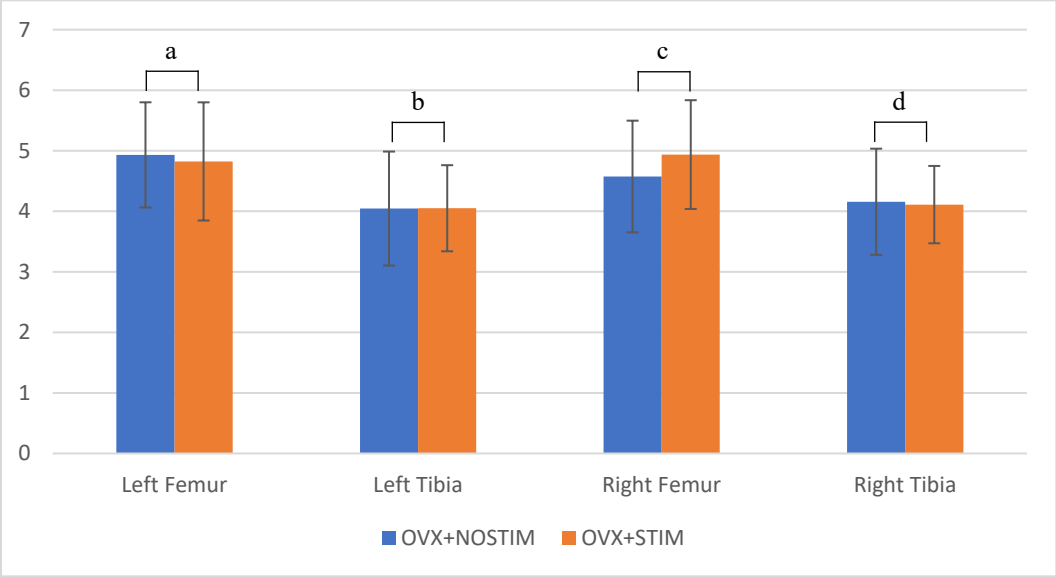


[a] $P = 0.178$ (N.S.); [b] $P = 0.495$ (N.S.); [c] $P = 0.253$ (N.S.); [d] $P = 0.459$ (N.S.)

Figure 105: Comparison of $I_{max}$ between the mid-diaphysis region of the OVX STIM and OVX NOSTIM group. No difference found between OVX NOSTIM and OVX STIM bones.

Finally, analysis was performed on the bone volume calculated by BoneJ, to determine whether there was a difference in the amount of cortical bone present due to the effects of the electrical stimulation. The internal paired comparison between the contralateral bones of the OVX STIM group can be seen in Figure 108 and Figure 109. Both analyses showed that the corresponding contralateral bones consisted of almost the same bone volume in all three regions, with the stimulated femur having slightly higher bone volume than the non-stimulated, although these results were not found to be statistically significant. The same comparison performed in the SHAM STIM group can be seen Figure 110 and Figure 111, the results of which were also not statistically significant across all comparisons made. Lastly, a comparison between OVX STIM and OVX NOSTIM groups (as shown in Figure 112, Figure 113, and Figure 114) showed small differences between the

groups in each region, with the magnitude of these differences decreasing as the analysed region moves from the end of the growth plate towards the mid-diaphysis. None of the comparisons were found to be statistically significant in this case.

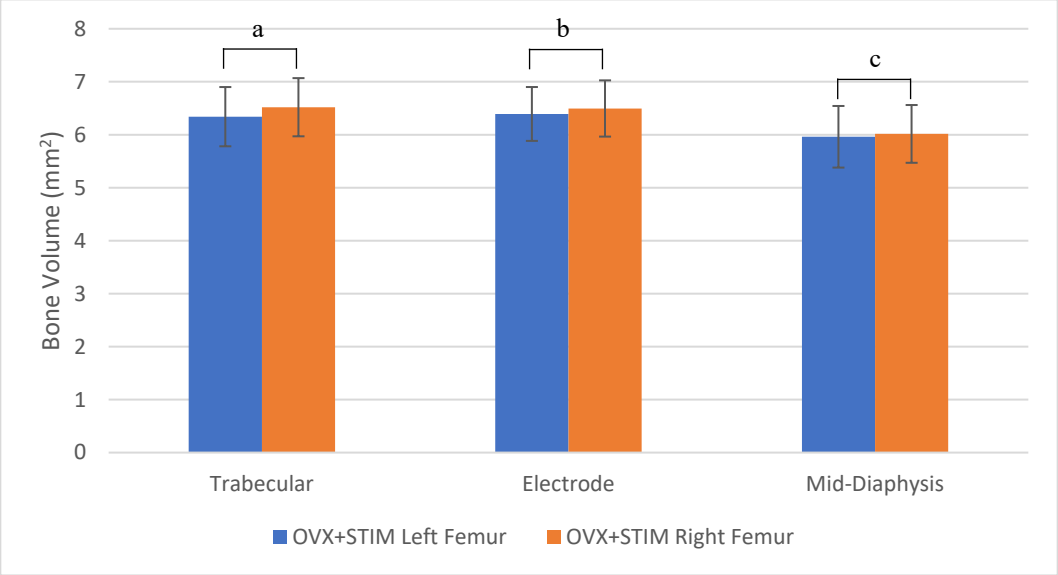


[a] $P = 0.206$ (N.S.); [b] $P = 0.082$ (N.S.); [c] $P = 0.251$ (N.S.)

Figure 106: Comparison of bone volume in OVX STIM femur. No differences found between stimulated and unstimulated femur across all three regions.

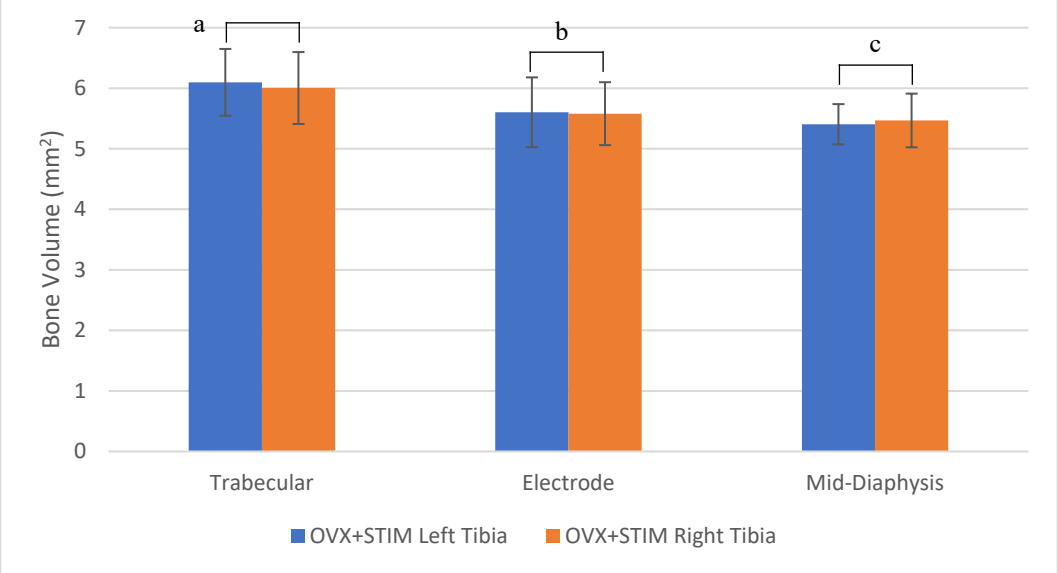


[a] $P = 0.301$ (N.S.); [b] $P = 0.472$ (N.S.); [c] $P = 0.277$ (N.S.)

Figure 107: Comparison of bone volume in OVX STIM tibia. No differences found between stimulated and unstimulated tibia across all three regions.

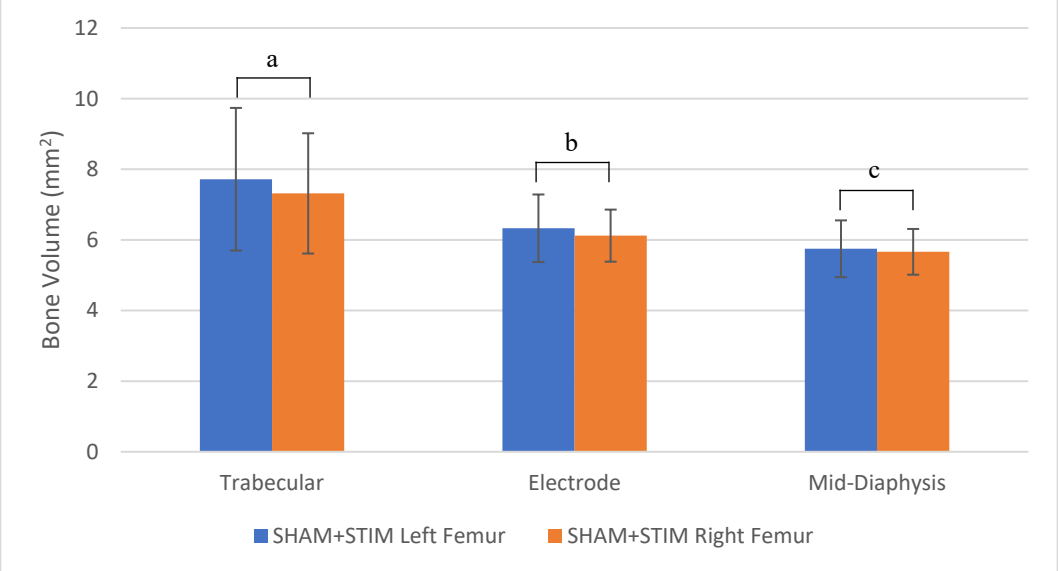


[a] $P = 0.094$ (N.S.); [b] $P = 0.148$ (N.S.); [c] $P = 0.269$ (N.S.)

Figure 108: Comparison of bone volume in SHAM STIM femur. No differences found between stimulated and unstimulated femur across all three regions.

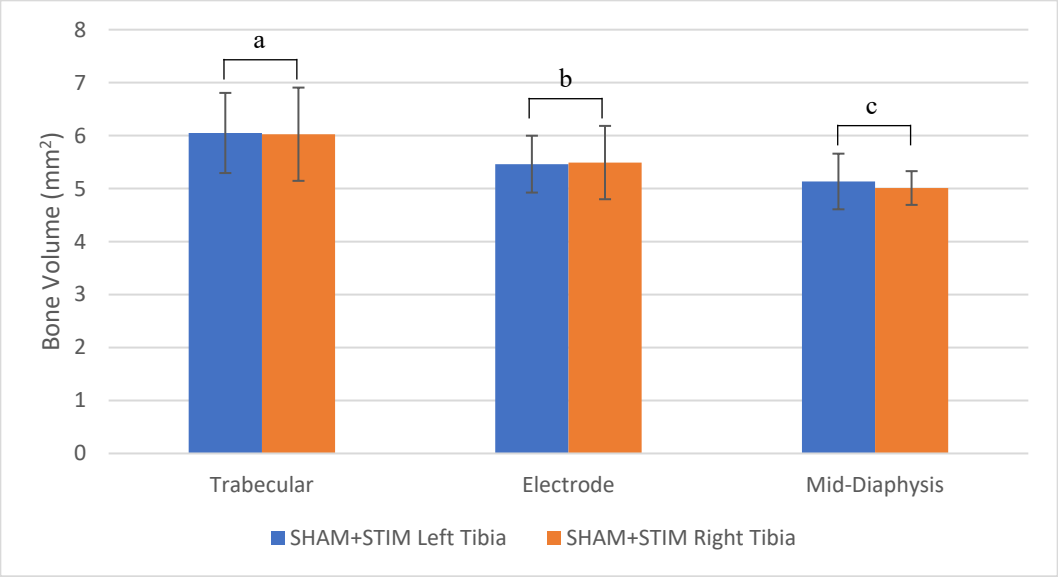


[a] $P = 0.200$ (N.S.); [b] $P = 0.405$ (N.S.); [c] $P = 0.146$ (N.S.)

Figure 109: Comparison of bone volume in SHAM STIM tibia. No differences found between stimulated and unstimulated tibia across all three regions.

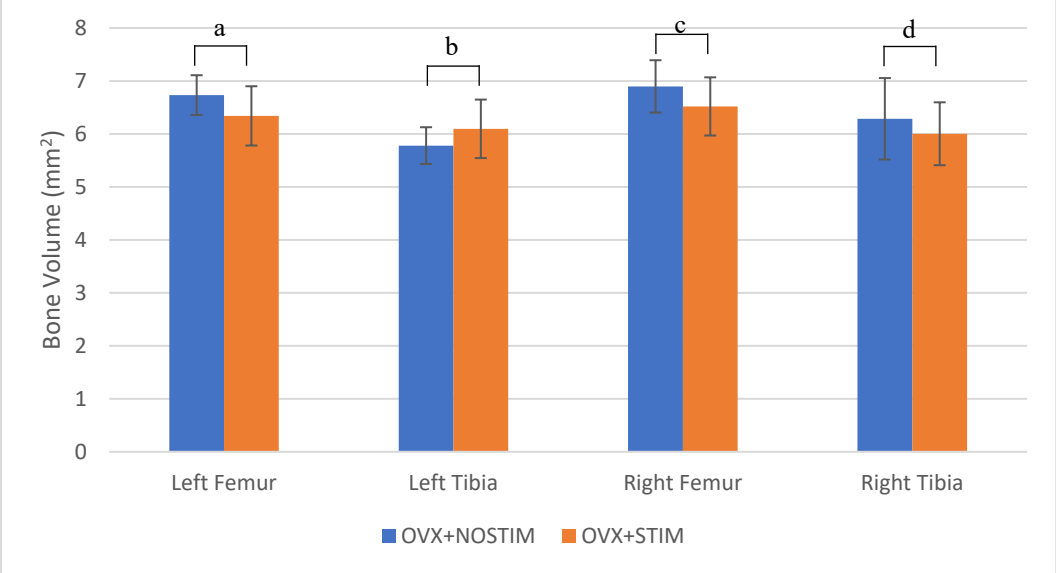


[a] $P = 0.092$ (N.S.); [b] $P = 0.131$ (N.S.); [c] $P = 0.120$ (N.S.); [d] $P = 0.246$ (N.S.)

Figure 110: Comparison of Imax between the trabecular region of the OVX STIM and OVX NOSTIM group. OVX STIM showed slightly lower bone volume than OVX NOSTIM in all bones except the left tibia.

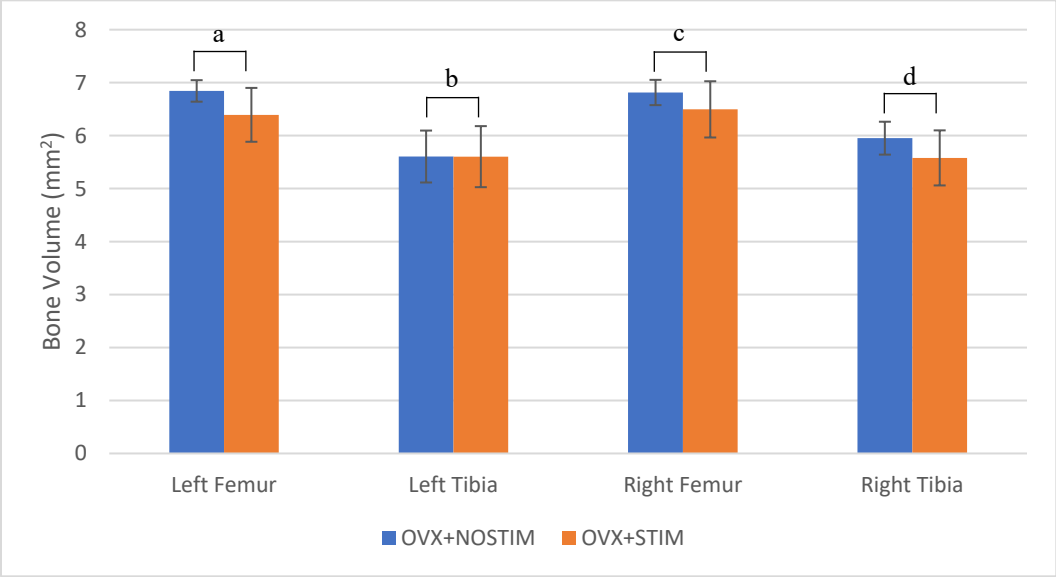


[a] $P = 0.036$; [b] $P = 0.179$ (N.S.); [c] $P = 0.105$ (N.S.); [d] $P = 0.081$ (N.S.)

Figure 111: Comparison of Imax between the electrode region of the OVX STIM and OVX NOSTIM group. OVX STIM showed slightly lower bone volume than OVX NOSTIM in all bones except the left tibia.

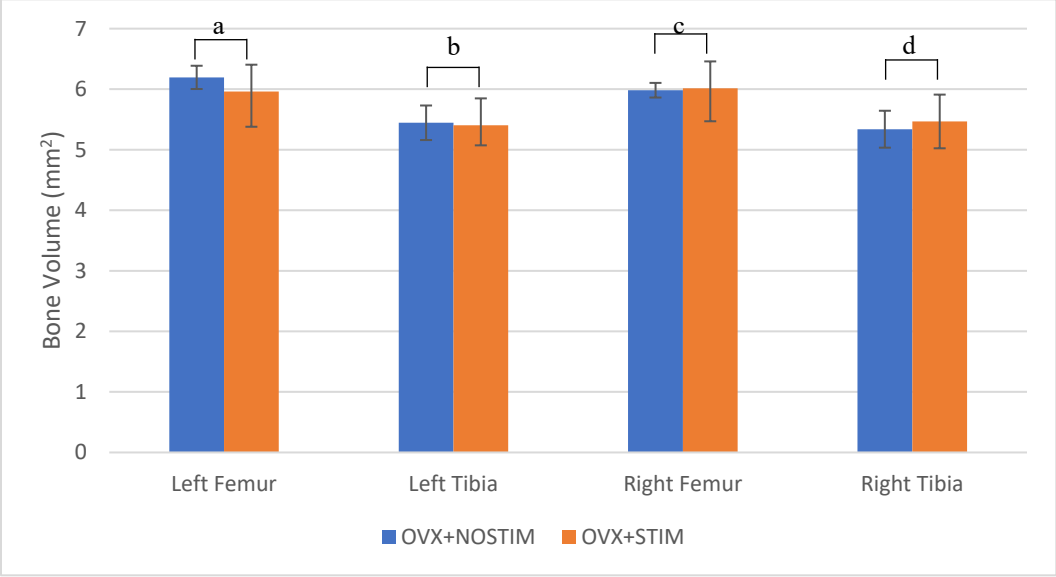


[a] $P = 0.307$ (N.S.); [b] $P = 0.412$ (N.S.); [c] $P = 0.445$ (N.S.); [d] $P = 0.246$ (N.S.)

Figure 112: Comparison of Imax between the mid-diaphysis region of the OVX STIM and OVX NOSTIM group. No significant differences found between groups.

# CHAPTER 9: DISCUSSION

## 9.1 SUMMARY

According to Osteoporosis Canada, around 1.5 million Canadians have been diagnosed with Osteoporosis (Public Health Agency of Canada 2010), a debilitating bone disease that occurs when the body loses too much bone, primarily in the trabecular region. Of these individuals, 1 in 5 reported having a fracture due to the extent of this induced bone loss. The current solutions to best maintain bone density are to take age-appropriate vitamins, partake in impact-type exercise, and take medication. Unfortunately, only 40% of affected individuals reported taking the necessary vitamins, and only 43% reported regular physical activity. To address these issues, the effectiveness of an alternative method of maintaining bone density, electrical stimulation, was explored, to test the hypothesis that low frequency, constant current electrical stimulation could promote bone growth or reduce the rate of bone loss. Therefore, the overall purpose of this thesis was to design a novel electrical stimulation circuit, and assess the effectiveness of the treatment in female OVX rats.

The first objective of this thesis involved the development of a circuit capable of delivering a 15 Hz, 250 $\mu$A, sinusoidal constant current signal for the electrical stimulation. Using the difference amplifier circuit combine with the integrator circuit, this requirement was achieved. The circuit was then built using through-hole components on a breadboard and its constant current capabilities were tested using fixed resistances at the output, as well as using discard animals.

The second objective was to develop a novel SOP with a custom anesthetic device to enable experimentation on multiple rats simultaneously. The device consisted of an induction chamber larger enough to hold up to 6 rats at a time, and an anesthetic tube that was able to maintain the sleep states of the rats for at least 1 hour. The induction chamber was developed by laser cutting sheets of PLA plastic with 4 walls, a base, and a top, which were then assembled and glued together. Additionally, the chamber consisted of a barbed fitting and a 3D printed adapter to enable coupling with the hosing of an anesthetic vaporizer. The anesthetic tube was an ABS pipe with 6 drilled holes along the body with sizes large enough for the noses of each rat to fit in. It also consisted of a 3D printed flow-limiting component and 3D printed adapters to couple with the anesthetic vaporizer hoses. The device was then tested on discard rats to determine the appropriate parameters (i.e. anesthetic flow rate and concentration) that enabled safe anesthetization of the animals for a 1-hour period, and a SOP was developed for the experimentation period.

The final objective involved the evaluation of the effectiveness of the electrical stimulation treatment after testing on OVX rats. This involved 6-week, 1 hour/day electrical stimulation experimentation on each rat. Following the stimulation period, the rats were sacrificed, and the femurs and tibia of each rat dissected. The bones were then imaged using micro-CT imaging, and the images were analyzed using software to determine various parameters related to both trabecular and cortical bone. Statistically significant differences were found in the

femur of the trabecular bone when a within-specimen comparison was performed in the stimulated OVX group, where the stimulated femur had greater number of trabeculae compared to the non-stimulated femur. This result agreed with additional results found when analyzing bone strength parameters such as the second moment of area. The outcome of this research represents a novel finding for the effects of electrical stimulation on bone loss, and would need to be further tested to determine the true effectiveness.

## 9.2 STRENGTHS & LIMITATIONS

Many strengths and limitations were discovered through the process of completing this research. The overall objective of determining the effects of electrical stimulation on bone loss was not a novel concept as it had already been performed in prior studies. But, evaluating these effects in the OVX rat model using capacitive coupling stimulation was a topic that was not previously researched, as previous studies focused on different animal models such as rabbits (Fredericks 1999; Hassler et al. 1976; Yonemori et al. 1996) and turkeys (Rubin et al. 1989), different physiological anomalies such as disuse osteopenia (Brighton, Katz, et al. 1985), and different methods of electrical stimulation such as PEMF (Chang & Chang 2003; Mcleod & Rubin 1992).

Another strength of this study was the specific parameters chosen for the electrical stimulation signal. Contrary to prior research articles, these parameters were chosen due to them being the most relevant in determining the safety of the application of electrical stimulation. Namely, these parameters are the frequency,

which was chosen to ensure no muscle contraction occurs, the current density, which was chosen to be low enough such that no damage to the skin occurs, and constant current nature of the signal, which was chosen to compensate for the differences in tissue resistances between animals to ensure each animal is delivered the same amount of stimulation.

This study also had an appropriate sample size for the paired analysis. The result for the internal comparison between the stimulated and unstimulated legs of the OVX STIM group was statistically significant for the comparison between femurs. Running a power calculation showed that a sample size of 6 was enough to achieve statistical power of 90%, meaning that the null hypothesis (the trabecular number being the same between both bones) will be rejected at a probability of 90%.

One of the main limitations of this study is present when performing comparisons between groups. The weights of each rat varied across all rats, even across rats within the same group. These differences could have affected the amount of bone loss and bone growth experienced by the rats due to the amount of forces experienced by the bones – the bones of the heavier rats would undergo higher stresses. Additionally, some of the rats in the study were singly-housed. Rats are generally kept in pairs within a cage as they are social animals that enjoy play, which is the major source of activity they experience during the day. The singly-housed rats would have had this key activity missing, which may have contributed to a higher weight gain, or even less forces experienced by their bones due to having a more static lifestyle. These physiological variations are controlled for when

performing internal paired comparisons, but may affect results when comparing between groups.

Another limitation is the application of this research to humans. There are currently four types of bisphosphonate dugs approved for use in Canada (Osteoporosis Canada 2016). Although the New England Journal of Medicine has found inconsistencies in the ability of these bisphosphonates to reduce fractures (Whitaker et al. 2012), they are one of the top 10 most employed drugs in Ontario with over 230 thousand active beneficiaries in 2015 alone (CIHI 2016). This would make any device developed from this research difficult to penetrate a market that would allow its use. Additionally, the effects of these drugs are throughout the body and provide a holistic effect on preventing bone loss, while this research focused on a localized effect in long bones only.

## 9.3 RECOMMENDATIONS

This research focused on the effects of electrical stimulation on bone loss in the OVX rat model, with significant improvement in the number of trabeculae found in the femur. To test if this improvement was due to the electrical stimulation, the experiments should be performed again to assess repeatability. Additionally, a larger sample size would provide more effective results, especially for the internal paired comparison of trabecular thickness between femurs where the result was almost statistically significant ($P = 0.0508$). For a statistical power of 80%, a sample size of 15 would be enough to establish a 95% statistical significance.

Since prior art has found more effects in a disuse osteopenia animal model, the OVX model might not be as well suited for electrical stimulation applications compared to the disuse model, as exemplified by the lack of effects found on cortical area, trabecular thickness, and cortical strength. The experiments may also benefit from controlling the amount of food that the OVX rats receive, to try and mitigate the large difference in weight between the OVX and SHAM rats, which may allow for more meaningful comparisons.

Although this research only looked at the effects of 15 Hz electrical stimulation, it could be extended to examine the effects of higher frequency electrical stimulation as well, and can even use the same circuit developed here. Prior studies have used frequencies in the kHz range for both bone loss and bone healing applications, so examining these higher frequencies using a pure sinusoidal signal in either an OVX or disuse model would provide some insight into what electrical stimulation protocol may work best as a treatment.

# CHAPTER 10: CONCLUSION

This research examined the examined the effects of 15 Hz, constant current, sinusoidal electrical stimulation on bone loss in the OVX rat model. A custom electrical circuit was designed to deliver the electrical stimulation via surface electrodes to the right leg of the rat around the proximal tibial metaphysis region. A novel multi-rat anesthetic device was developed to allow the anesthetization of 6 rats simultaneously, greatly reducing experimentation time. The results from micro-

CT analysis of trabecular and cortical bone showed an 11.4% increase in trabecular number between the stimulated and non-stimulated femur within the OVX group. Further work would need to be performed to validate the efficacy of this treatment in the femur, and to see if alternate stimulation parameters could induce effects in the tibia.

# BIBLIOGRAPHY

Andreuccetti, D., Fossi, R. & Petrucci, C., 1997. An Internet resource for the calculation of the dielectric properties of body tissues in the frequency range 10 Hz - 100 GHz. *IFAC-CNR, Florence (Italy)*. Available at: http://niremf.ifac.cnr.it/tissprop/.

Bakker, P., Vliet, L.J. van & Verbeek, P.W., 1999. Edge preserving orientation adaptive filtering. In *Proceedings. 1999 IEEE Computer Society Conference on Computer Vision and Pattern Recognition (Cat. No PR00149)*. p. 535–540 Vol. 1.

Bassett, C.A. & Becker, R.O., 1962. Generation of electric potentials by bone in response to mechanical stress. *Science*, 137(3535), pp.1063–4.

Belill, K.A. et al., 2014. Femoral Strength after Induced Lesions in Rats ( Rattus norvegicus ). *Comparative Medicine*, 64(3), pp.186–192.

Bodamyali, T. et al., 1998. Pulsed electromagnetic fields simultaneously induce osteogenesis and upregulate transcription of bone morphogenetic proteins 2 and 4 in rat osteoblasts in vitro. *Biochemical and Biophysical Research Communications*, 250(2), pp.458–461.

Bouxsein, M.L. et al., 2010. Guidelines for assessment of bone microstructure in rodents using micro-computed tomography. *Journal of Bone and Mineral Research*, 25(7), pp.1468–1486.

Bragdon, B. et al., 2011. Bone Morphogenetic Proteins: A critical review. *Cellular Signalling*, 23(4), pp.609–620. Available at: http://dx.doi.org/10.1016/j.cellsig.2010.10.003.

Brighton, C.T., Hozack, W.J., et al., 1985. Fracture healing in the rabbit fibula when subjected to various capacitively coupled electrical fields. *Journal of Orthopaedic Research*, 3(3), pp.331–340.

Brighton, C.T., Katz, M.J., et al., 1985. Prevention and treatment of sciatic denervation disuse osteoporosis in the rat tibia with capacitively coupled electrical stimulation. *Bone*, 6(2), pp.87–97.

Bronaugh, R., Stewart, R. & Congdon, E., 1983. Differences in permeability of rat skin related to sex and body site. *J. Soc. Cosmet. Chem.*, 34, pp.127–135.

Bruker Micro-CT, Automated trabecular and cortical bone selection. *UManitoba Faculty of Health Sciences*, p.18. Available at: http://umanitoba.ca/faculties/health_sciences/medicine/units/cacs/sam/media/MN008_Automated_trabecular_and_cortical_bone_selection.pdf [Accessed August 21, 2018a].

Bruker Micro-CT, Method for ex-vivo micro-CT analysis of rat bone (proximal tibia, distal femur). *UManitoba Faculty of Health Sciences*, p.7. Available at: http://umanitoba.ca/faculties/health_sciences/medicine/units/cacs/sam/media/MN003_Bone_microCT_analysis_rat.pdf [Accessed August 22, 2018b].

Chang, K. & Chang, W.H.S., 2003. Pulsed Electromagnetic Fields Prevent Osteoporosis in an Ovariectomized Female Rat Model: A Prostaglandin E2-Associated Process. *Bioelectromagnetics*, 24(3), pp.189–198.

CIHI, 2016. Prescribed Drug Spending in Canada, 2016: A Focus on Public Drug Programs. *Canada Institute for Health Information*, p.55. Available at: https://secure.cihi.ca/free_products/Prescribed Drug Spending in Canada_2016_EN_web.pdf.

Doube, M. et al., 2010. BoneJ: Free and extensible bone image analysis in ImageJ. *Bone*, 47(6), pp.1076–1079. Available at: http://linkinghub.elsevier.com/retrieve/pii/S8756328210014419.

Eser, P. et al., 2003. Effect of electrical stimulation-induced cycling on bone mineral density in spinal cord-injured patients. *European Journal of Clinical Investigation*, 33(5), pp.412–419.

Eyres, K.S., Saleh, M. & Kanis, J.A., 1996. Effect of Pulsed Electromagnetic Fields on Bone Formation and Bone Loss During Limb Lengthening. *Bone*, 18(6), pp.505–509.

Fredericks, D., 1999. Effects of Pulsed Electromagnetic Fields on Bone Healing in a Rabbit Tibial Osteotomy Model. *Journal of Orthopaedic Trauma*, 14(2), pp.93–100.

Fukada, E. & Yasuda, I., 1957. On the piezoelectric effect of bone. *Journal of the Physical Society of Japan*, 12(10), pp.1158–1162. Available at: http://jpsj.ipap.jp/link?JPSJ/12/1158/.

Gerber, H.P. et al., 1999. VEGF couples hypertrophic cartilage remodeling, ossification and angiogenesis during endochondral bone formation. *Nature Medicine*, 5(6), pp.623–628.

Golub, E. & Boesze-Battaglia, K., 2007. The role of alkaline phosphatase in mineralization. *Current Opinion in Orthopaedics*, 93(18), pp.444–448. Available at: http://www.jem.org/cgi/doi/10.1084/jem.93.5.415.

Greenfield, S., 2015. Is it possible to generate a sine wave of different positive and negative amplitude? *Quora*, p.1.

Griffin, M. et al., 2013. Enhancement of Differentiation and Mineralisation of Osteoblast-like Cells by Degenerate Electrical Waveform in an In Vitro Electrical Stimulation Model Compared to Capacitive Coupling. *PLoS ONE*, 8(9), p.e72978. Available at:

http://dx.plos.org/10.1371/journal.pone.0072978.

Hartig, M., Joos, U. & Wiesmann, H.P., 2000. Capacitively coupled electric fields accelerate proliferation of osteoblast-like primary cells and increase bone extracellular matrix formation in vitro. *European Biophysics Journal*, 29(7), pp.499–506.

Hassler, C.R. et al., 1976. Studies of Enhanced Bone healing via Electrical Stimuli. *Clinical orthopaedics and related research*, 124, pp.9–19.

Hodgkin, A.L., Huxley, A.F. & Katz, B., 1949. Measurement of Current-Voltage Relations in the Membrane of the Giant Axon of Loligo. *The Journal of Physiology*, 108(1), pp.424–448.

Holt, H., 2014. A Deeper Look into Difference Amplifiers. *Analog Dialogue*, 48(2), pp.1–3.

Hwang, S.J. et al., 2012. The Implications of the Response of Human Mesenchymal Stromal Cells in Three-Dimensional Culture to Electrical. *Tissue Engineering*, 18, pp.432–445.

Inoue, N. et al., 2002. Effect of pulsed electromagnetic fields (PEMF) on late-phase osteotomy gap healing in a canine tibial model. *Journal of Orthopaedic Research*, 20(5), pp.1106–1114.

Isaacson, B.M. & Bloebaum, R.D., 2010. Review Bone bioelectricity: What have we learned in the past 160 years? *Journal of Biomedical Materials Research*, 95A(4), pp.1270–1279.

Jee, W.S. & Yao, W., 2001. Overview: animal models of osteopenia and osteoporosis. *Journal of musculoskeletal & neuronal interactions*, 1(3), pp.193–207.

Kane, W., 1987. Direct current electrical bone growth stimulation for spinal fusion. *Spine*, 13(3), pp.363–365.

Kim, I.S. et al., 2006. Biphasic electric current stimulates proliferation and induces VEGF production in osteoblasts. *Biochimica et Biophysica Acta - Molecular Cell Research*, 1763(9), pp.907–916.

Kuzyk, P. & Schemitsch, E., 2009. The science of electrical stiumulation therapy for fracture healing. *Indian Journal of Orthopaedics*, 43(2), pp.127–131.

Lane, T. & Sage, H., 1994. The biology of SPARC, a protein that modules cell-matrix interactions. *Federation of American Societies for Experimental Biology*, 8(2), pp.163–173.

Lirani-Galvão, A.P.R. et al., 2006. Electrical field stimulation improves bone mineral density in ovariectomized rats. *Brazilian journal of medical and*

*biological research*, 39(11), pp.1501–5. Available at: http://www.ncbi.nlm.nih.gov/pubmed/17146563.

Mcelhaney, J., 1967. The Charge Distribution on the Human Femur Due to Load. *The Journal of Bone and Joint Surgery*, 49(December), pp.1561–1571.

Mcleod, K. & Rubin, C., 1992. The Effect of Low-Frequency Electrical Fields on Osteogenesis. *1The Journal of Bone and Joint Surgery*, 6(74–A), pp.920–929.

Mortimer, J.T., 2011. Motor Prostheses. *Comprehensive Physiology*. Available at: http://doi.wiley.com/10.1002/cphy.cp010205.

Nabil, Y., Abdalfattah, S. & Lotfy, M., 2014. A clinical study on the effect of electric stimulation on segment transfer distraction osteogenesis for mandibular reconstruction. *Egyptian Journal of Oral & Maxillofacial Surgery*, 5(1), pp.10–15. Available at: http://content.wkhealth.com/linkback/openurl?sid=WKPTLP:landingpage&an=01438520-201401000-00004.

Osteoporosis Canada, 2016. BISPHOSPHONATES. , p.1. Available at: https://osteoporosis.ca/about-the-disease/treatment/bisphosphonates/ [Accessed September 15, 2018].

Otter, M.W., McLeod, K.J. & Rubin, C.T., 1998. Effects of electromagnetic fields in experimental fracture repair. *Clinical orthopaedics and related research*, (355 Suppl), pp.S90-104. Available at: http://ovidsp.ovid.com/ovidweb.cgi?T=JS&PAGE=reference&D=med4&NEWS=N&AN=9917630.

Owen, T. et al., 1990. Progressive development of the rat osteoblast phenotype in vitro : Reciprocal relationships in expression of genes Associated with Osteoblast Proliferation and Differentiation During Formation of the Bone Extracellular Matrix. *Journal of Cellular Physiology*, 130(1990), pp.420–430.

Parent, A., 2004. Giovanni Aldini: From Animal Electricity to Human Brain Stimulation. *Canadian Journal of Neurological Sciences*, 31(4), pp.576–584.

Peckham, P.H. & Knutson, J.S., 2005. Functional Electrical Stimulation for Neuromuscular Applications. *Annual Review of Biomedical Engineering*, 7(1), pp.327–360. Available at: http://www.annualreviews.org/doi/10.1146/annurev.bioeng.6.040803.140103.

Peng, H. et al., 2002. Synergistic enhancement of bone formation and healing by stem cell-expressed VEGF and bone morphogenetic protein-4. *Journal of Clinical Investigation*, 110(6), pp.751–759.

Piccolino, M., 1997. Luigi Galvani and animal electricity: Two centuries after the foundation of electrophysiology. *Trends in Neurosciences*, 20(10), pp.443–448.

Public Health Agency of Canada, 2010. What is the impact of osteoporosis in Canada and what are Canadians doing to maintain healthy bones? *Government of Canada*, p.1. Available at: https://www.canada.ca/en/public-health/services/chronic-diseases/osteoporosis/what-impact-osteoporosis-what-canadians-doing-maintain-healthy-bones.html [Accessed September 15, 2018].

Rubin, C., Mcleod, K. & Lanyon, L., 1989. Prevention of Osteoporosis by Pulsed Electromagnetic Fields. *The Journal of Bone and Joint Surgery*, 71(3), pp.411–417.

Saltzman, C., Lightfoot, A. & Amendola, A., 2004. PEMF as treatment for delayed healing of foot and ankle arthrodesis. *Foot & ankle international*, 25(11), pp.771–3. Available at: http://www.ncbi.nlm.nih.gov/pubmed/15574233.

Schindelin, J. et al., 2012. Fiji: an open-source platform for biological-image analysis. *Nature Methods*, 9, p.676. Available at: http://dx.doi.org/10.1038/nmeth.2019.

Schneider, C.A., Rasband, W.S. & Eliceiri, K.W., 2012. NIH Image to ImageJ: 25 years of image analysis. *Nature Methods*, 9, p.671. Available at: http://dx.doi.org/10.1038/nmeth.2089.

Sert, C. et al., 2002. The preventive effect on bone loss of 50-Hz, 1-mT electromagnetic field in ovariectomized rats. *Journal of bone and mineral metabolism*, 20(6), pp.345–9. Available at: http://www.ncbi.nlm.nih.gov/pubmed/12434162.

Stein, G.S. & Lian, J.B., 1993. Molecular mechanisms mediating proliferation/differentiation interrelationships during progressive development of the osteoblast phenotype. *Endocrine Reviews*, 14(4), pp.424–442.

Stitt, M., 1993. Simple Filter Turns Square Waves Into Sine Waves. *Burr-Brown Application Bulletin*, (602), pp.1–8.

Stromal, M. et al., 2009. Novel Effect of Biphasic Electric Current on In Vitro Osteogenesis and Cytokine Production. *Tissue Engineering*, 15(9).

Takeuchi, H. et al., 2012. Influence of Skin Thickness on the in Vitro Permeabilities of Drugs through Sprague-Dawley Rat or Yucatan Micropig Skin. *Biological & Pharmaceutical Bulletin*, 35(2), pp.192–202. Available at: http://joi.jlc.jst.go.jp/JST.JSTAGE/bpb/35.192?from=CrossRef.

Whitaker, M. et al., 2012. Bisphosphonates for Osteoporosis — Where Do We Go from Here? *New England Journal of Medicine*, 366(22), pp.2048–2051. Available at: http://www.nejm.org/doi/abs/10.1056/NEJMp1202619.

WPI, 2013. Isolated Stimulation Explained.

Yakar, S. et al., 2002. Circulating levels of LGF-1 directly regulate bone growth and density. *Journal of Clinical Investigation*, 110(6), pp.771–781. Available at: http://www.ncbi.nlm.nih.gov/pubmed/12235108.

Yang, Y. et al., 2017. Bone-targeting parathyroid hormone conjugates outperform unmodified PTH in the anabolic treatment of osteoporosis in rats. *Drug Delivery and Translational Research*, 7(4), pp.482–496.

Yonemori, K. et al., 1996. Early effects of electrical stimulation on osteogenesis. *Bone*, 19(2), pp.173–80. Available at: http://www.ncbi.nlm.nih.gov/pubmed/8853862.

Yushkevich, P.A. et al., 2006. User-guided 3D active contour segmentation of anatomical structures: Significantly improved efficiency and reliability. *NeuroImage*, 31(3), pp.1116–1128. Available at: https://www.sciencedirect.com/science/article/pii/S1053811906000632?via%3Dihub [Accessed August 16, 2018].

Zhang, M. et al., 2002. Osteoblast-specific knockout of the insulin-like growth factor (IGF) receptor gene reveals an essential role of IGF signaling in bone matrix mineralization. *Journal of Biological Chemistry*, 277(46), pp.44005–44012.

# APPENDICES

## Appendix A: Code used to program microcontroller

```
const int signalPin = 1;
void setup() {
  pinMode(signalPin, OUTPUT);
}
void loop() {
  digitalWrite(signalPin, HIGH);
  delay(33.3);
  digitalWrite(signalPin, LOW);
  delay(33.3);
}
```

Appendix B: Current reaching bone in equivalent circuit model

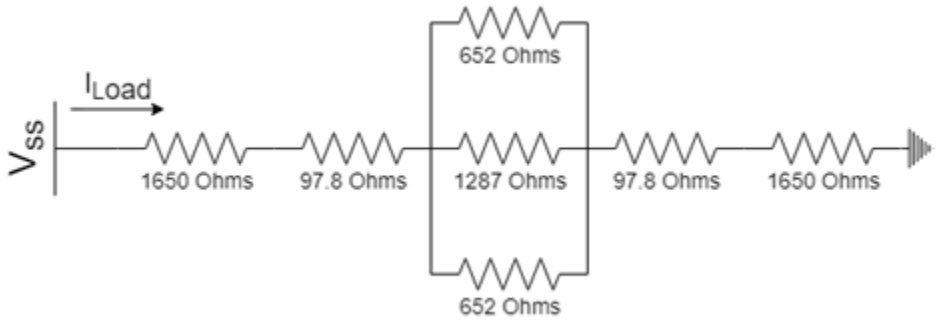


**Total resistance of the circuit:**

$R_{total} = 1650 + 97.8 + (652 \,||\, 1287 \,||\, 652) + 97.8 + 1650$
$R_{\text{total}} = 1650 + 97.8 + 260 + 97.8 + 1650$
$R_{total} = 3755.6\ \Omega$

**Current that will reach the bone:**

$I_{load} = 250\ \mu A$

$I_{bone} = \frac{(652 \,||\, 652)}{1287} * I_{load}$
$I_{bone} = \frac{326}{1287} * 250\ \mu A$
$I_{bone} = 63\ \mu A$

Appendix C: BoneJ macro for calculation moments of inertia

```
run("Moments of Inertia", "start=540 end=600 bone_min=0.1 bone_max=1
slope=0.0000 y_intercept=1.8000 align");

close();

run("Moments of Inertia", "start=655 end=715 bone_min=0.1 bone_max=1
slope=0.0000 y_intercept=1.8000 align");

close();

run("Moments of Inertia", "start=1195 end=1255 bone_min=0.1 bone_max=1
slope=0.0000 y_intercept=1.8000 align");

close();

run("Input/Output...", "jpeg=85 gif=-1 file=.csv use_file save_row");

saveAs("Results", "F:/BoneJ_Results/30_tr.csv");
```

## Appendix D: Anesthetic Protocol

The usage of the anesthetic devices followed the protocol listed below, which was determined through multiple tests to ensure the rats are able to be put into a deep sleep state, this sleep state is deep enough such that the rats are able to be taken from the induction chamber and put into the tube, and that the tube is able to maintain this sleep state for a 1-hour period.

1. Attach the output of the anesthetic vaporizer provided by the CAF into the inputs of the induction chamber and anesthetic tube
2. Attach the scavenger hose to the outputs of the induction chamber and anesthetic tube
3. Ensure the flow is going into the induction chamber by clipping shut the hose going into the anesthetic tube
4. Place 6 rats into the induction chamber
5. Turn the oxygen flow rate to 2, and vaporizer concentration to 5, for 9 to 10 minutes
6. When the induction time is up, unclip the hose going to the anesthetic tube so flow is going to both the induction chamber and the anesthetic tube
7. Transfer the 6 rats to the anesthetic tube, ensuring their noses are put inside the holes cut into the latex sheets
8. Stop the flow from going into the induction chamber by clipper its hose shut
9. Perform the reflex test on each rat after 15-30 seconds in the anesthetic tube, to ensure none of the rats are awake

10. Turn the vaporizer concentration down to 3, and the oxygen flow rate down to 1.5
11. After 10-15 minutes, turn the vaporizer concentration down to 2.5
12. After 40 – 45 minutes, turn the vaporizer concentration down to 2